ABSTRACT

Title of Document:	SCHWANN CELL–NEURON INTERACTIONS AND AXONAL STRAIN APPLICATION IN PERIPHERAL NERVOUS SYSTEM REGENERATION
	James Matthew Love, Ph.D. Bioengineering, 2014
Directed By:	Assistant Professor, Dr. Sameer Shah, Bioengineering

Peripheral nervous system (PNS) injuries affect many people worldwide and if not repaired can leave individuals with the burden of living with chronic pain or motor dysfunction. My thesis focused on understanding the relationship nerves and neurons have with their environment during development and normal function in order to identify means by which the regenerative process might be manipulated and enhanced. The implementation of a two-armed study allowed me to investigate the interactions between Schwann cells (SCs), a vital neuronal support cell, and neurons, as well as, the role strain has in local protein synthesis. First, I detailed the changes in membrane stability within

the two cell types. I was able to identify decreased velocity and correlative movement of neuronal membranes compared to SCs suggestive of a higher level of membrane stability. Both cell types saw a decreased trend in both velocity and correlative movement following development of contact with the other pointing to increased cellular membrane stability upon establishment of cellular contact. The next study looked into the development of ribosomal clusters within SC processes, which have been suggested to be a ribosomal source for axons following injury. I found that SCs develop ribosomal distributions early and use anterograde transport to maintain these populations. Upon the initiation of myelination, transport is depressed suggestive of a reduce role of ribosomes within the myelin fraction. The final portion of my work focused on neuronal adaptation to strain. I initially found that nerves are able to accommodate strains by straightening axons in a linear fashion. I further found moderate strain application to nerves upregulates the activation of both mTOR and S6, two molecules integral in enhancing protein synthesis. Additionally, increases in the cytoskeletal proteins β-actin and SMI31 were observed in response to strain. Suppression of the mTOR pathway with rapamycin led to an elimination of the effect on SMI31 but not β-actin. Rapamycin also enabled a strain-dependent reduction in tubulin levels. The results of my thesis contextualize the results of a number of studies that have observed advantageous regenerative outcomes from the use of SCs and strain for PNS recovery.

Schwann cell-neuron interactions and axonal strain application in peripheral nervous system regeneration

by

James Matthew Love

Dissertation submitted to the Faculty of the Graduate School of the
University of Maryland, College Park in partial fulfillment
of the requirements for the degree of
Doctor of Philosophy
2014

Advisory Committee:

Professor Adam Hsieh, Co-chair
Professor Sameer Shah, Co-chair
Professor Marco Colombini
Professor John Fisher
Professor Steven Jay

Acknowledgements

The work described herein was completed at the Neuromuscular Bioengineering Laboratories at the University of Maryland, College Park and the University of California, San Diego under the supervision of Dr. Sameer Shah and co-advisement of Dr. Adam Hsieh.

I would like to thank God for giving me every opportunity to pursue my goals even when at times He knew better than I what these might be.

I would like to thank my family for their love and support. Especially my mother, Cindy Love, whose ability to raise three young children into intelligent, capable, and caring adults serves as a reflection of her compassion and dedication in spite of great hardship. I would like to thank my father, Jamie Love, who has spent the better part of my life, no doubt, watching and blessing me from afar. My sisters, Erin Lowry and Bethany Love, for the phone calls and messages consistently remind me to be thankful for the little things. My brother-in-law, Jayson Lowry, who was always ready with a beer in hand to help me relax. My grandparents, Bill and Judy Harris and Marshall and Ginger Love, and all my aunts, uncles, and numerous cousins who have helped in countless ways getting me to the point where I am today.

I would like to thank Dr. Shah for being an incredible mentor. Under his guidance I have learned innumerable lessons about science, ethics, mentorship and running a functioning research lab. Additionally, I would like to thank Dr. Shah for his financial support of my academic pursuits.

I would like to thank the past and present members of the Neuromuscular Bioengineering Laboratory without whom I would have been unable to complete even a

fraction of this work including: Joshua Chetta, Gunja Dave, Brian Bober, Tom Chuang, Justin Papreck, and Ken Vaz.

I would like to thank my committee members who have provided valuable feedback which helped shape the direction of my work.

I would like to thank all the members of the UCSD Department of Orthopaedics for supporting me as a visiting graduate student, especially: Dr. Rick Lieber, Dr. Sam Ward, Dr. Simon Schenk, Dr. Koichi Masuda, Dr. Raji Pichika, Shannon Bremner, Amanda White, Margie Mathewson, and Tomonori Yamaguchi.

I would like to thank Erin Ryan for her unwavering love and support of me for the past year, especially in the past few months where I have spent nearly as many hours inside of lab as outside of it. I would like to thank all of my friends who have supported me throughout my Ph.D. journey including: Conrad Lubek, Brian Jester, Walter Ayllon, Isaac Chavez, Eli Michel, Jason Hollenbaugh, Bobby Raby, Eric Tola, Michael Carey, Richie Booth, Anik Dutteroy, Amy Hudson, Lindsay D'Ambrosio, Jaimie Miller, Kevin Doran, Robert Merkert, and Evan Beard. Finally, I would like to thank the countless teachers, coaches, and mentors who have enabled me to get to where I am today especially Mike Laidley and Eric DeCosmo who taught me to never be afraid of a little hard work.

TABLE OF CONTENTS

List of Tables

List of Figures

List of Publications (In Order of Publication Date)

First author manuscripts:

Varibility in membrane continuity between Schwann cells and neurons [2]

JM Love, GK Pathak, J Chetta, and SB Shah

Cellular and Molecular Bioengineering 2012; 5(4):450-62

Co-author contributions:

Gunja Pathak: Writing and project discussion

Joshua Chetta: Kymograph program development, writing and project discussion

Sameer Shah: Project development, results discussion, manuscript editing, corresponding author

Nerve strain correlates with structural changes quantified by Fourier analysis [3]

JM Love, T-H Chuang, RL Lieber, and SB Shah

Muscle & Nerve 2013; 48(3):433-5

Co-author contributions:

Ting-Hsien Chuang: Surgical assistance

Rick Lieber: Project discussion and guidance

Sameer Shah: Project development, results discussion, manuscript editing, corresponding author

Ribosomal trafficking is reduced in Schwann cells following induction of myelination

JM Love and SB Shah

*Submitted*Co-author contributions:

Sameer Shah: Project development, results discussion, manuscript editing, corresponding author

Differential regulation of cytoskeletal protein synthesis following nerve strain

JM Love, BG Bober, AT White, S Bremner, S Schenk, SB Shah

In Preperation

Co-author contributions:

Brian Bober: *In vitro* device production and troubleshooting

Amanda White: Western blot training and signaling discussions

Shannon Bremner: Electrophysiological set-up and tutorial

Simon Schenk: Western blot training and signaling discussions

Sameer Shah: Electrophysiology, project development, results discussion, manuscript editing, corresponding author

Contributing author manuscripts:

Influences of desmin and keratin 19 on passive biomechanical properties of mouse skeletal muscle [4]

SB Shah, **JM Love**, A O'Neill, RM Lovering, and RJ Bloch

Journal of Biomedicine and Biotechnology 2012 (Online)

Co-author contribution:

James Love: CAD model and submission for manufacture of microscope mountable biomechanical set up for application of strain on muscle fibers during imaging

A novel internal fixator device for peripheral nerve regeneration [5]

T-H Chuang, RE Wilson, **JM Love**, JP Fisher, and SB Shah

Tissue Engineering Part C: Methods 2013; 19(6):427-37

Co-author contribution:

James Love: SY5Y culture and confocal imaging for *in vitro* live-dead cell assessment

A comparative assessment of axonal and dendritic mRNA transport in maturing hippocampal neurons [6]

GK Pathak, **JM Love**, J Chetta, and SB Shah

PLOS One 2013; 8(7) (Online)

Co-author contribution:

James Love: Writing and project discussions

Morphological response of neuronal cells to changes in their osmotic environment

BG Bober, **JM Love**, M Sitnova, S Shahamatdar, A Kannan, and SB Shah

Cytoskeleton (Under Review)

Co-author contribution:

James Love: Experimental planning, cell culture, image acquisition, writing and project discussions, manuscript editing

Novel mode of bidirectional actin transport requires microtubule and actin integrity

J Chetta, **JM Love**, and SB Shah

Submitted

Co-author contribution:

James Love: Implementation of mathematical rate kinetic model of actin transport response to various drug treatments. Model based on kinetic model found in Chapter 3 using parameters from actin transport study.

Tensile loading does not negatively influence regenerative capacity of peripheral nerves

T-H Chuang, **JM Love**, K Vaz, JM Brown, SB Shah

In Preparation

Co-author contribution:

James Love: Automated image processing for nerve count and quantification

Chapter 1: Introduction

Section 1: The peripheral nervous system (PNS)

The nervous system is composed of two major branches, the peripheral (PNS) and the central (CNS) (Figure 1-1). The CNS is composed of the brain and the spinal cord and generally tasked with integrating and processing signals it receives from the periphery. The PNS encompasses the remaining nerves which reside outside of the CNS.

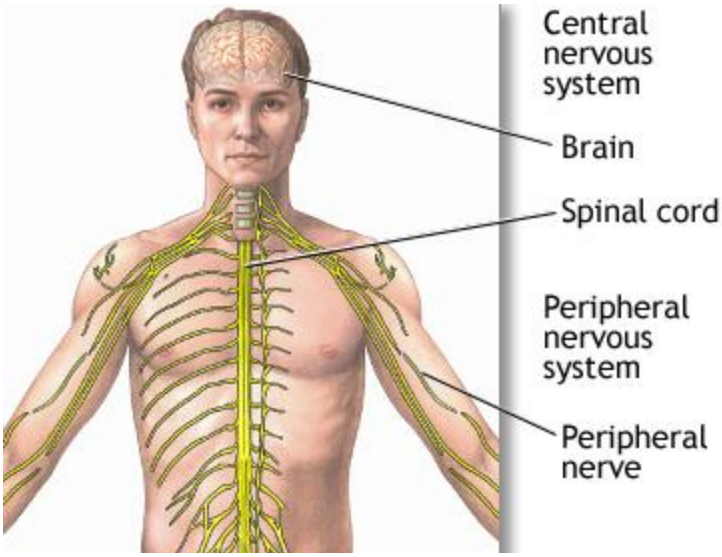

Figure 1-1: Nervous system [1]

Diagram showing the two branches of the nervous system, central and peripheral (reprinted under Fair Use)

Normal, healthy function of the PNS is centrally important to the well-being and overall quality of life of all people. Tasked with both initiating movement through motor neurons and sensing one's surroundings through sensory neurons, the PNS possesses a multitude of responsibilities. Any disruption to normal function, whether through traumatic injury or disease, can be crippling to an individual.

Anatomically, the PNS is composed of both the autonomic and somatic nervous systems. The autonomic nervous system maintains necessary unconscious functioning including regulation of heart rate, breathing, and digestion. The somatic system, on the other hand, is responsible for voluntary muscle contractions and sensing a person's surroundings. Both motor and sensory neurons possess cell bodies, or soma, located

adjacent to the spinal column in collections called ganglia. Motor neurons emerge ventrally within the ventral roots while sensory neurons project dorsally within the dorsal roots. From these positions neurons project long axons to their innervation sites. The axons descend distally from the spinal column in thicker bundles of axons resembling cables called neurons. In this manner axons can extend to lengths of up to one meter in the extremities of humans.

Section 2: Peripheral Nervous System Injury and Statistics

Traumatic PNS injuries, the partial or complete severance of a nerve, frequently result from automobile accidents, violence, and military conflict [7,8]. Up to 1% of individuals by the age of 70 can expect to experience some type of traumatic peripheral nerve injury costing individuals and private businesses billions of dollars in care and lost wages [9]. In addition to financial cost, there is also a substantial cost to quality of life, including an inability to perform basic daily activities and considerable loss of independence resulting from disrupted motor function and chronic pain [8]. Patients presenting with a peripheral nerve injury will often receive surgical intervention following reduction of inflammation at the site of injury followed by physical therapy in an attempt to restore function. Nonetheless, over 30% of patients still report poor or no functional recovery following injury [10].

Section 3: Current Therapeutic Techniques

Currently the prognosis of a particular injury directly relates to the size of the trauma. Best outcomes are expected if the surgeon is able to directly reattach the severed ends together. In many cases tissue may be lost or damaged to the point that it must be cleaned up prior to reattachment to permit regrowth of healthy tissue. The gap that exists

or develops during the surgical procedure explicitly correlates to the patient's prognosis [11,12].

Due to the presence of a gap, axonal regrowth must be directed into the distal portion of the severed nerve. For larger gaps this is often accomplished by the use of nerve tissue, either from the patient (autograft), a donor (allograft), or another species (xenograft). Current allograft options have been successful at bridging gaps up to 50 mm in length [13]. For smaller gap sizes tissue engineered nerve guidance conduits have been moderately successful. Tissue engineered solutions offer many benefits above native tissue including the absence of donor site morbidity and the availability of materials. Nonetheless, they are only consistently used clinically to bridge gaps of less than 30 mm [14]. When the expected outcomes of these devices reach those of the autograft they will offer a viable alternative for doctors performing nerve repair procedures.

Numerous efforts are being made to explore methods to enhance the effectiveness of tissue engineered conduits by attempting to accelerate the axonal elongation rate. Prolonged denervation of the target muscle leads to atrophy and negatively affects recovery prognosis [15]. Tissue engineers are examining a number of areas that affect axonal outgrowth including growth factors [16], physical guidance cues [17], material compatibility [18,19], introduction of support cells [20], and application of strain [21] among others as potential means of intervention.

Section 4: Thesis scope

In my thesis I investigated two means by which scientists believe recovery could be accelerated. First, I focused on the interplay between neurons and Schwann cells and the way by which Schwann cells may affect the recovery process (Chapters 2 and 3). This was followed by an investigation into the role strain plays on enhancing constructive

local signaling pathways and local protein synthesis (Chapters 4 and 5). In these two distinct arms of my dissertation work I was able to explore multiple modalities by which the regeneration process could be affected and accelerated.

Section 5: Developmental and regenerative role of Schwann cells

The PNS is composed of a number of different cell types. While neurons are the most notable cell type, their support cells, particularly Schwann cells, play an integral role in axonal health and viability. Schwann cells are most noted for enhancing neuronal conduction velocities through the process of myelination [22]. In addition to this major role, Schwann cells aid neurons through additional mechanisms including provision of physical guidance cues [23] and growth factors [24-26] to promote axonal elongation during development and regeneration. Additionally, recent evidence shows Schwann cells act as an additional source of axonal ribosomes for local protein synthesis during the regeneration process [27,28].

Subsection 1: Stabilization/axon guidance during development/following injury

During development Schwann cells receive signals promoting migration along axons to position themselves for myelination [29-33]. During the regeneration process the roles reverse with Schwann cells forming a substrate promoting axonal extension and guides neuronal regrowth [23]. In both cases, physical interactions between the two cell types are able to provide specific cues to direct proper functional development or recovery. Many examples of contact driven effects between Schwann cells and neurons exist illustrating how the two cell types generally stabilize each other. Specifically, Schwann cells upregulate adhesion levels [34] following contact with neurons. On the other hand, contact between Schwann cells and neurons can lead to enhancement of neurofilament phosphorylation, indicative of a more stable cytoskeleton [35].

Interestingly, membrane addition and retrieval in neurons primarily occurs at the growth cone and cell body and "flows" along the axon [36-42]. In contrast, other migratory cells do not observe this membrane flow [43]. Additionally, in neurons, membrane addition is coupled to the cytoskeletal stability and regional tension within the membrane [44-47]. Such concepts of membrane flow and cytoskeletal stability have not been tested in developing Schwann cells, but would provide insight into the role of cytoskeletal stabilization on membrane stability during their dynamic development.

To gain such insight, I performed a comparative assessment of the influence contact has on the membrane stability of both Schwann cells and neurons in Chapter 2. I found that neurons possess more stable membranes compared to Schwann cells, as evidenced by reductions in both membrane velocities and membrane continuity. These parameters exhibited a decreasing trend upon the establishment of contact with each other suggesting a role for contact in stabilizing the two cell types. The work resulted in a first-author publication in Cellular and Molecular Bioengineering (reprinted with permission from Springer) [2].

Subsection 2: Myelination, material transfer, growth factor influences, ribosomal transfer

Recent evidence has shown another way Schwann cells aid neurons is by transferring ribosomes to neurons following injury [27,28]. These studies fail to identify mechanistically how this occurs but hypothesize that the transfer events may occur at Schmidt-Lanterman incisures (Figure 1-2) [27]. In order for this to occur, ribosomes must localize to Schwann cell projections during development and to the myelin following compaction. A niche of literature has identified roles for projection and myelin based ribosomes mainly focusing on the role of these structures to provide myelin basic protein

(MBP) during compaction [48-52]. Within these studies it is noted that ribosomes localize around, but not within, Schmidt-Lanterman incisures [48]. Missing from the current literature is a full understanding of how ribosomes are distributed within the Schwann cell and how they achieve this distribution over time.

My exploration of ribosomal distributions and the rates of ribosomal transport over early developmental time points following induction of myelination are discussed at length in Chapter 3. The goal for this study was to identify how ribosome trafficking and distributions change throughout development. Specifically, I looked to identify whether ribosomal populations remained within the early myelinating projections and whether these distributions were found to co-localize to particular cytoskeletal elements. I also wanted to determine if these ribosomal populations were maintained through anterograde trafficking to support the idea that populations are maintained and residing in the myelin fraction in the event Schwann cells are signaled to transfer ribosomes to the neurons they myelinate. I found that distributions are established along the Schwann established and maintained from early time points in culture. The net amount of ribosomal trafficking decreased as a result of myelination induction suggesting a decreased role for local synthesis within the myelin compartment. This work resulted in the submission of a first-author manuscript.

Section 6: Role of Strain

Another means being investigated for enhancement of PNS regeneration is the effect of strain application on neuronal outgrowth. Current surgical best practice is to leave nerves in a tensionless environment following nerve repair. However, evidence is building both *in vitro* and *in vivo* that application of strain can be beneficial for axonal outgrowth, accelerating the rate of axonal elongation.

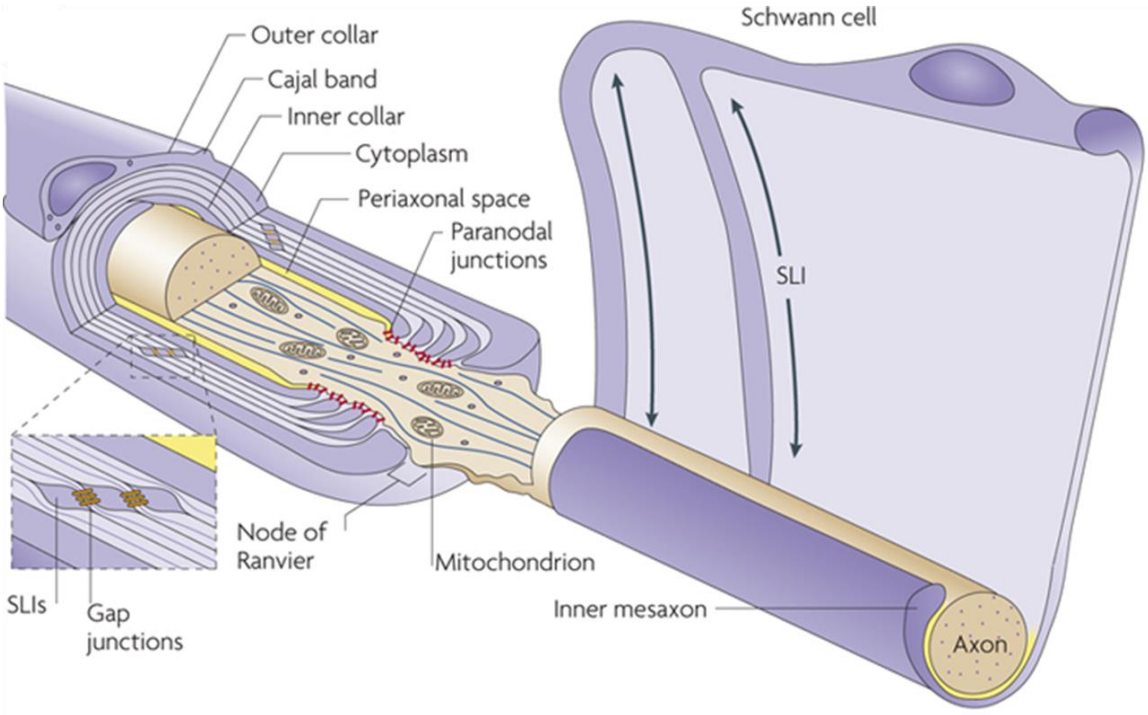

Figure 1-2: Myelinating Schwann cell [53]

Myelinating Schwann cells possess a number of distinct regions important in maintaining proper function. Schmidt-Lanterman incisures (SLI) are regions of direct membrane-membrane contact between Schwann cells and neurons. (Reprinted with permission from Nature Publishing Group)

Subsection 1: Neuronal architecture

Nerves *in vivo* are subject to fairly large deformations with minimal damage [54]. Studies have shown that deformations exceeding the physiological range negatively affect neuronal function as noted by conduction velocity and magnitude deficits [55,56]. This damage can be fully reversible for low level strains but is only minimally reversible for larger strains [55,56]. Nerves are able to accommodate physiological deformation due to a unique packing structure that imparts a native waviness on the axons within the nerve bundle [57]. In this way, the nerves are able to undergo large strains while being subjected to very low levels of stress [55]. As the nerve is strained the axons unravel imparting minimal strain on the axons themselves [58]. The microscopic packing

structure contributes to the macroscopic observation of bands of Fontana (Figure 1-3) [58]. These bands are apparent to the naked eye and respond to strain by elongating [3]. Due to the repeating nature of the bands, I looked to correlate the frequency of the bands with imposed strain using a Fourier analysis based method in Chapter 4 [3]. Development of this method would provide further evidence that the effect results from deformation of underlying physical structures, as elongating the physical specimen would decrease the observed frequency. Implementation of this technique could provide surgeons with an effective tool in the operating room for estimating accidental and intentional strains applied to nerves during surgery. In Chapter 4, I discuss how this technique found correlations between applied strain and banding frequency, as well as, agreement between the strain at which damage occurs (>20%) and the point when the bands ultimately are no longer visible. This work resulted in a first-author publication in *Muscle & Nerve* (permission requested for republication from John Wiley and Sons, Inc.) [3].

Figure 1-3: Bands of Fontana [3]

Subsection 2: Local protein synthesis

This geometry of neurons is a major confounding factor of axonal regeneration. The localization of neuronal cell bodies up to one meter away from the injury site in the most distal cases leads to a temporal delay in response to an injury stimulus. This delay affects both transcriptional and translational regulation at the cell body. The manufacture and shipment of proteins from the cell body to the injury site would, in the case of slow axonal transport (around 1 mm/day) [59,60], likely take months. In order to regenerate in

a timelier manner, the axon has the ability to locally produce proteins within the axonal compartment [61,62], as well as, the ability to respond to cues from the local cellular environment [63].

In the past twenty years, the observation of protein synthetic machinery including ribosomes, golgi, and ER components present in the axon has provided evidence for local synthesis of proteins [62,64]. The observation of specific mRNAs localized to the axonal compartment has offered further insight into the roles of local synthesis (Figure 1-4) [62,65]. Of these mRNAs, a number are cytoskeletal in nature including β-actin, all neurofilaments, and tubulin [66-68]. Additionally, evidence shows that axonal extension and regeneration is dependent on the ability of a neuron to produce proteins within the axon [69]. Other studies have shown that restoration of this process can lead to recovery of the axons ability to regenerate [70]. A combined look at this evidence provides support for the integral nature and therapeutic potential of this pathway with regards to neuronal regeneration.

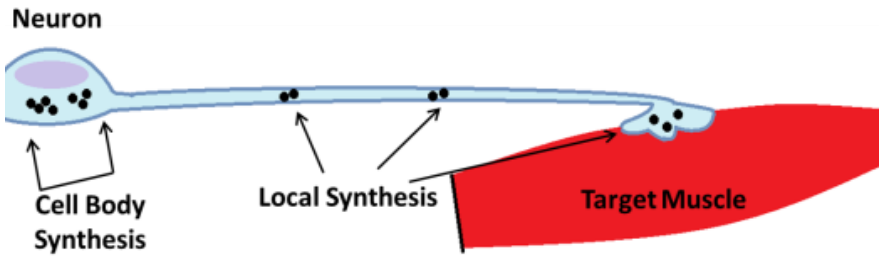

Figure 1-4 - Axonal protein synthesis

Neurons possess ribosomes in both the cell body and the axonal compartment. Both pools of ribosomes are integral in maintaining the well-being of the cell.

Subsection 3: Strain and axonal elongation

Since nerves are generally considered to be non-load bearing, the influence of mechanical strains on their growth potential was initially ignored. This generalization fails to consider the fact that neurons innervate muscles early in development and must grow over the life of an individual. Additionally, the positive outcomes seen in limb lengthening surgeries provide evidence for neuronal adaptability to applied strains [71]. In load bearing tissues including muscle, bone, and cartilage there is a wealth of evidence showing the influence of mechanical loading in affecting tissue adaptations (reviewed in [72-74]). This work shows, in most cases, physiological loading conditions can positively influence the development of these tissues. The subset of literature focusing on neuronal tissues appears to be closing in on a similar trend. *In vitro* evidence has shown that strain application can accelerate the process of axonal elongation up to eight-fold when applied at initially low strain rates are slowly increased [75-77]. More complex experiments are being completed *in vivo.* While the verdict is still out at this point, they do not seem to be negatively affecting neuronal regeneration [21,78]. This initial work has opened a number of questions related to the process of neuronal adaptation to strain, most notably the mechanism which allows for accelerated elongation.

Subsection 4: Strain-mediated signaling

While it is unclear how neurons adapt to strain application, the activated signaling pathways in other systems are very well-documented. In muscles it has been determined that mTOR activation during cyclic loading is responsible for observed increases in protein synthesis and hypertrophy [79,80] (pathway in Figure 1-5). The well-established role for mTOR signaling in axonal elongation and axonal protein synthesis makes this pathway particularly attractive for implication in the beneficial response of neurons to strain application. Axonal protein synthesis is required for axonal extension and

regeneration. Evidence also suggests that not only is mTOR activity necessary for axonal outgrowth [81,82] but enhancement of the mTOR signal via pTEN inhibition can enhance the outgrowth capacity [70]. A number of axonally synthesized proteins could be beneficial for axonal growth including the cytoskeletal proteins β-actin, neurofilament-H, and tubulin [66-68] Enrichment of the pools of these essential structural proteins could be responsible for the observed increase in axonal elongation rates. In Chapter 5 I investigated the role of mTOR signaling in response to locally applied strains *in vivo* and the affect this had on local cytoskeletal protein levels. This work builds upon the *in vitro* studies detailing I found that both mTOR and downstream S6 activation levels increase in whole nerve following the application of strain. Additionally, increased levels of β-actin and phosphorylated neurofilament-H (SMI31) were observed. In the presence of rapamycin, an inhibitor of mTOR activity, I found differential regulation of cytoskeletal elements in response to strain including a muting of the SMI31 response, as well as, a decrease in the levels of tubulin. While my work pertains to a protein synthetic requirement for axonal elongation, it is important to note that additional contributions in the form of lipid and energetic requirements must be considered to place this work in the context of whole cell growth and survival. This work is currently in preparation for submission of a first-author manuscript to a peer-reviewed journal.

Section 7: Intersection of research aims

The two-armed approach to my dissertation work has allowed me to explore diverse aspects of the nervous system each of which could prove critical to the regeneration process. While Chapters 2 and 3 focus on Schwann cell and neuron interactions in the context of development and potential regenerative application, Chapters 4 and 5 looked into the ability of nerves and neurons to positively respond to

strain. Nonetheless, the information obtained from each of these subsets provides initial evidence to tailor future research towards integrating approaches for optimal regeneration following peripheral nervous system injuries. Direct implications of both may be seen in the enhancement of axonal protein synthesis, a major requirement of the neuronal recovery process. On a broader scale, development of more effective regeneration strategies will allow individuals currently destined to live with chronic pain and reduced motor function to live lives not affected by these complications while reducing the financial burden on society as a whole. These advancements will reduce the burden on the individual in performing activities of daily living enabling easier living and a more positive outlook. My work comprises a small segment of the wealth of research that has been done and must continue in order to reach the point where surgeons can offer universal restoration of function to all individuals suffering from PNS injuries and diseases.

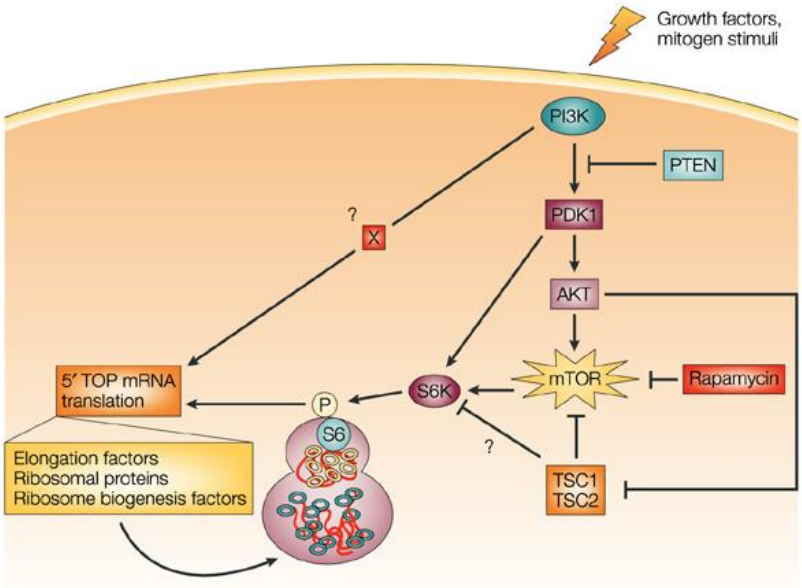

Figure 1-5: mTOR signaling pathway [83]

Diagram outlining important elements in the mTOR driven protein synthesis pathway (Reprinted with permission from Nature Publishing Group)

Chapter 2: Variability in membrane continuity between Schwann cells and neurons [2]

Section 1: Introduction

Sensory neurons of the dorsal root ganglia (DRG) and Schwann cells (SCs), two distinct cell types of the peripheral nervous system (PNS), cooperate to provide functional signaling between the spinal cord of the central nervous system (CNS) and the distal reaches of the human body. The health, well-being, and proper performance of the two cell types integrally depend on those of the other. Both neurons and SCs possess a distinctive bipolar morphology that results in a high surface area to volume ratio. Maintenance of this morphology requires careful regulation of the expansion and contraction of the cellular plasma membrane as well as its interactions with structural elements in adhesion complexes and the intracellular cytoskeleton. Such regulation is particularly critical during cell movement or the extension and retraction of cellular projections.

There are multiple common principles underlying the motility of neurons and SCs. In the context of neuronal outgrowth, several studies have demonstrated the essential role of the cytoskeleton in growth cone motility, axonal guidance, and axonal transport [84-86]. More recently, studies have also focused on the regulation of the biomechanical properties of the axonal shaft during its outgrowth. This may occur through the generation of tensile forces along the axon and at the growth cone [87-89] as well as reorganization of the cytoskeleton and adhesion complexes in response to stresses and mechanotransductive signals [90-92]. Mechanisms guiding the addition of cellular membrane have also been examined in neurons, particularly during axonal outgrowth.

The growth cone is the most frequent site of membrane addition and retrieval, though a significant component may be added along the axon or flow anterogradely from cell bodies [36-42]. Membrane addition and retrieval are tightly coupled to the stability of actin and microtubule components of the cytoskeleton [44,45] as well as adhesion and regional tension within of the cell membrane [41,46,47]. This contrasts greatly with migratory cell types like keratocytes which do not witness any lipid flow [43]. Key influences on lipid flow as well as its quantification are therefore likely to include the nature of membrane connectivity to the cytoskeleton as well as regional differences in membrane composition.

Fewer studies have investigated force generation, cytoskeletal stability, and membrane dynamics in the projections of SCs, despite the importance of these processes during their migratory phase prior to myelination [93]. Studies of SC movement along fibrous scaffolds suggest that they, like neurons, follow mechanical guidance cues and can generate traction forces sufficient to break attachments at the trailing end [94-97]. Magnitudes and orientations of these forces have not been examined in SCs, though they may be analogous to other migratory cell types such as fibroblasts [98]. As for neurons, there is evidence that their microtubule stability plays a role in the plasma membrane expansion in SCs [99]. In addition, it has been shown that dynamics of cellular adhesion and actin networks play critical roles in SC spreading and migration [34,100].

Despite these conceptual similarities between neurons and SCs, we hypothesize that regional differences in the continuity of the plasma membrane may contribute to differences in physiological function required for the two cell types to operate in a mutualistic fashion. This study investigated differences in the mobility of the plasma

membrane in neurons and SCs, and compared the degree to which and length scale over which the cellular membranes of neurons and SCs behave as a mechanical continuum. In combination with high-resolution fluorescence imaging, we applied two different methods for correlation analysis previously used in other contexts [86,101,102] to quantify the continuity of the cellular membrane at various length scales during neuronal and SC motility. The establishment of neuronal contact was investigated as an additional factor influencing continuity; for neurons, such contact indicates a major step in maturity prior to axonal fasciculation, and for SCs, neuronal contact is required both for elongation along an axon and myelination [34,103-107] We propose that cells with more mobile tendencies, like SC migration, may have membranes that act more like a continuum, enabling more efficient mechanical communication.

Section 2: Materials and Methods

Subsection 1: Cell culture

Day 1-5 Sprague-Dawley rats were euthanized using CO_2 followed by decapitation. All animal protocols were approved and carried out in accordance with IACUC at the University of Maryland, College Park and University of California, San Diego. DRGs were dissected and placed on ice in 400 µl of DRG media (F-12 media, 10% FBS, 1% L-glutamate, and 1% Penicillin/Streptomycin). The samples were supplemented with 20 µg/ml of collagenase type IA (Sigma-Aldrich) and incubated at 37°C for 20 minutes (adapted from Oh et al.) [101,108]. The samples were then centrifuged at 76xg for 5 minutes and the media was removed. The DRGs were resuspended and dissociated in fresh DRG media.

Schwann cells were harvested from DRGs (with neurons) or sciatic nerves (no neurons). For the latter, cells were digested; first, in 3.33 mg/mL collagenase in L-15 for

45 minutes followed by digestion in 3 mL of 0.25% trypsin-EDTA and 1 mL of 1.2 mg/mL DNase I in L-15. The cells were suspended and cultured in Schwann cell media (DMEM containing 10% FBS, 1% Pennicillin/Streptomycin, .02 μg/mL, and .1 mg/mL Pituitary Extract) (Adapted through correspondence with Megan Wright from original protocol of Porter et al.) [109]. Cells were dispersed on 35 mm glass-bottom culture dishes coated in 8 μg/ml laminin (Sigma-Aldrich) for future viewing at a density of ~4 DRGs per plate and supplemented with 2 ml of DRG media. The cells were cultured overnight at 37°C prior to experimentation.

For cultures of isolated neurons, following resuspension in DRG media, the cells were again centrifuged at 76xg for 5 minutes. Media was removed and the cells were resuspended in 100 μl Basic Rat Nucleofector solution (Amaxa). Cells were electroporated using Amaxa Nucleofector technology and program G-013 to minimize contaminating fibroblasts and SCs. Cells were placed in RPMI and incubated for 15 minutes prior to plating to facilitate recovery. Post-recovery, cells were placed on glass-bottom dishes and confined to a region ~10 mm in diameter at a density of ~4 DRGs per plate and supplemented with 500 μl of DRG media containing 10 μg/ml NGF 7-S (Sigma-Aldrich) and 2% B-27 (Sigma-Aldrich). The cells were cultured overnight at 37°C prior to experimentation.

Subsection 2: Experimental Groups

Four experimental groups were identified based upon cell type and contact state. These groups were contacting neurons (NC), non-contacting neurons (NNC), contacting Schwann cells (SCC), and non-contacting Schwann cells (SCNC). Contact was defined based on the contact of the distal tip of a neuronal growth cone or a Schwann cell projection with a neuron. Cell types were identified by morphology following initial

identification by immunostaining for S100 (Figure 2-1B) to identify SCs and the neurofilament SMI-31 (Figure 2-1D) to identify neurons.

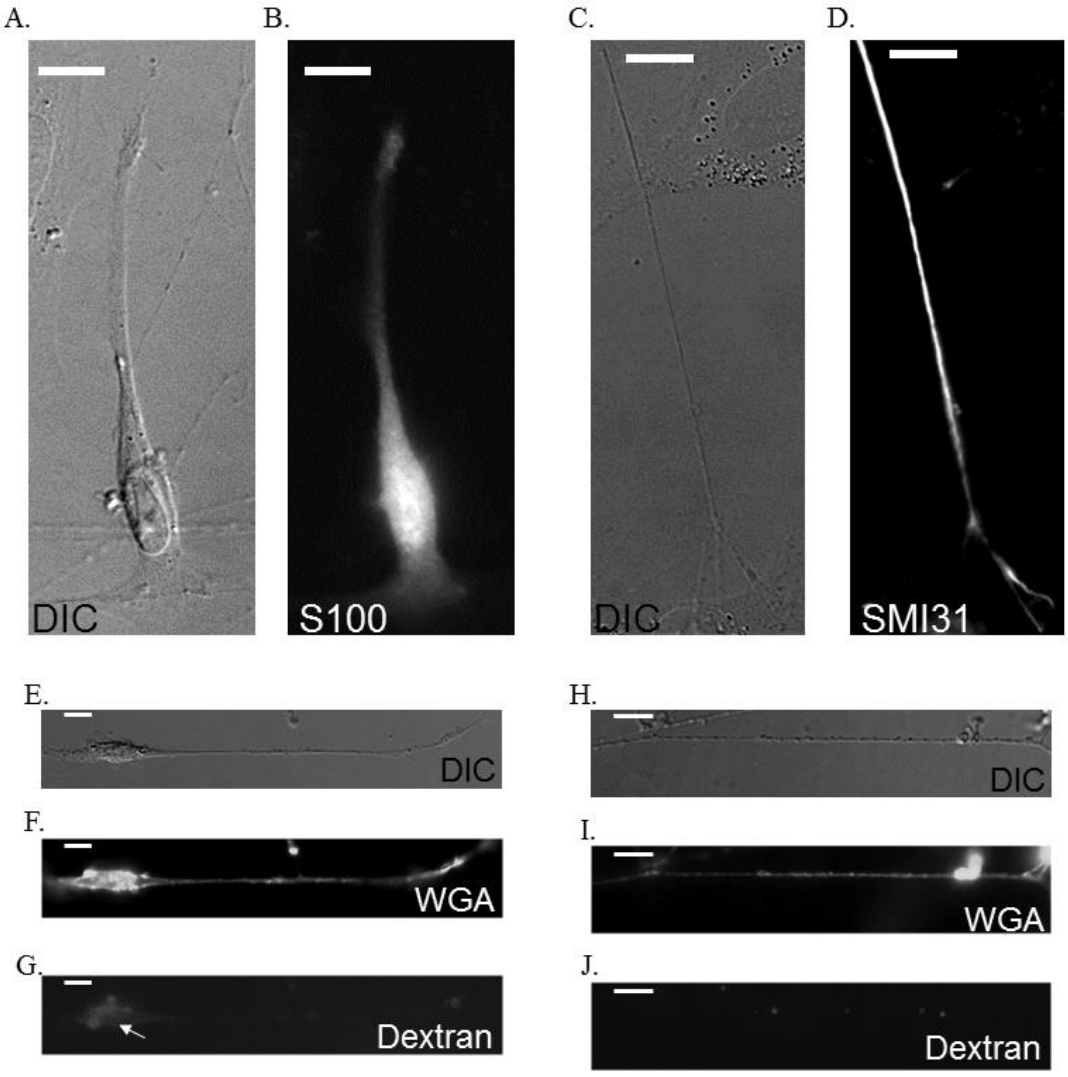

Figure 2-1: Identification of cell types and verification of imaging methods

Identification of Schwann cell imaged under DIC (A) confirmed by S100 immunostaining (B) and DRG imaged under DIC (C) confirmed by SMI31 immunostaining (D). Both Schwann cells (E,F,G) and DRGs (H,I,J) identified under DIC (E,H) were examined for internalization of wheat-germ agglutinin (F,I) identified by incubation with fluorescent dextran (G,J) with minimal internalization occurring at the cell body (note arrow). Scale bar, 10 μm

Subsection 3: Labeling of plasma membrane surface

Wheat germ agglutinin was used as a label for plasma membrane, as it has multiple binding sites for extracellular membrane bound sugars such as sialic acid and N-acetylglucosaminyl [110]. Wheat germ agglutinin conjugated to Oregon Green 488 (Invitrogen) was added to cultures at a concentration of 1.67 µg/ml, a concentration four-fold lower than that recommendation by the reagent literature. The cultures were then placed at 2°C for 10 minutes to allow binding and limit initial endocytosis. Imaging was performed immediately afterwards; as a positive control for endocytosis, cultures were examined after 4 hours (Supplemental Figure 2-1C). Minimization of endocytosis during refrigeration was confirmed through co-labeling with dextran conjugated to Alexa Fluor 594 (Invitrogen) added prior to refrigeration at a concentration of 5 mg/ml (Figures 2-1G and 2-1J). Minimal dextran internalization was observed at the cell body and growth cone and virtually absent along the projection/axon providing evidence that the majority, although perhaps not all, of the observed particles externally labeled the membrane. Following refrigeration, the plates were washed three times with cold PBS, media was replaced with cold DRG media and the cultures were imaged. An additional control was performed, imaging the WGA using confocal techniques (Supplemental Figure 2-1E).

Subsection 4: Imaging

Using an inverted TE-2000E microscope (Nikon) with a Lumen PRO2000 illumination system (Prior Scientific), CoolSNAP HQ2 (Photometrics), and Chroma filters (Bellows Falls,VT. EPI: 490 nm (FITC), 595 (Texas Red); Emission 525 nm (FITC), 620 nm (Texas Red)), both fluorescent (492 nm, 594 nm) and DIC images were gathered every 20 seconds for a period of 20 minutes to allow characterization of membrane mobility over time. This relatively infrequent imaging rate of fluorescence

combined with the low concentration of WGA dye reduced the likelihood of photoxicity, which otherwise manifest itself through axonal beading (Supplemental Figure 2-1B) or axonal retraction. Failure to see axonal elongation likely resulted from refrigeration prior to imaging slowing the rate of cellular processes. It should be noted that an elongation rate of ~30 μm/hr is seen following a four hour recovery at 37°C suggesting no permanent damage has been inflicted by refrigeration. An optimal environment was maintained at 37°C with ~4% CO_2 through a custom environmental chamber mounted around the microscope stage (Precision Plastics). For still fluorescent images of immunostains, this imaging system was also used without environmental considerations.

For direct examination of endocytosis, confocal microscopy was used. Cells were imaged using a Leica SP5 system. Standard lasers and filters were used. An argon laser enabled excitation at 488nm and emission was captured between 500-550 nm.

Subsection 5: Image Processing

The image sequences gathered from each sample were analyzed using custom MATLAB programs (Mathworks Inc.). In each image, the cellular projection was traced. A region of 9 pixels surrounding the trace (trace ± 4 pixels) was cropped and organized in order beginning with the first time point at the top and following with the second below it, etc. This organization represents time in y-direction and position along the cell in the x-direction much like a traditional kymograph and as such we will refer to our analysis technique as a kymograph as well (Figures 2-2C and 2-2F). The paths of particles that appear in the kymographs were then traced and analyzed using both MATLAB and Excel (Microsoft).

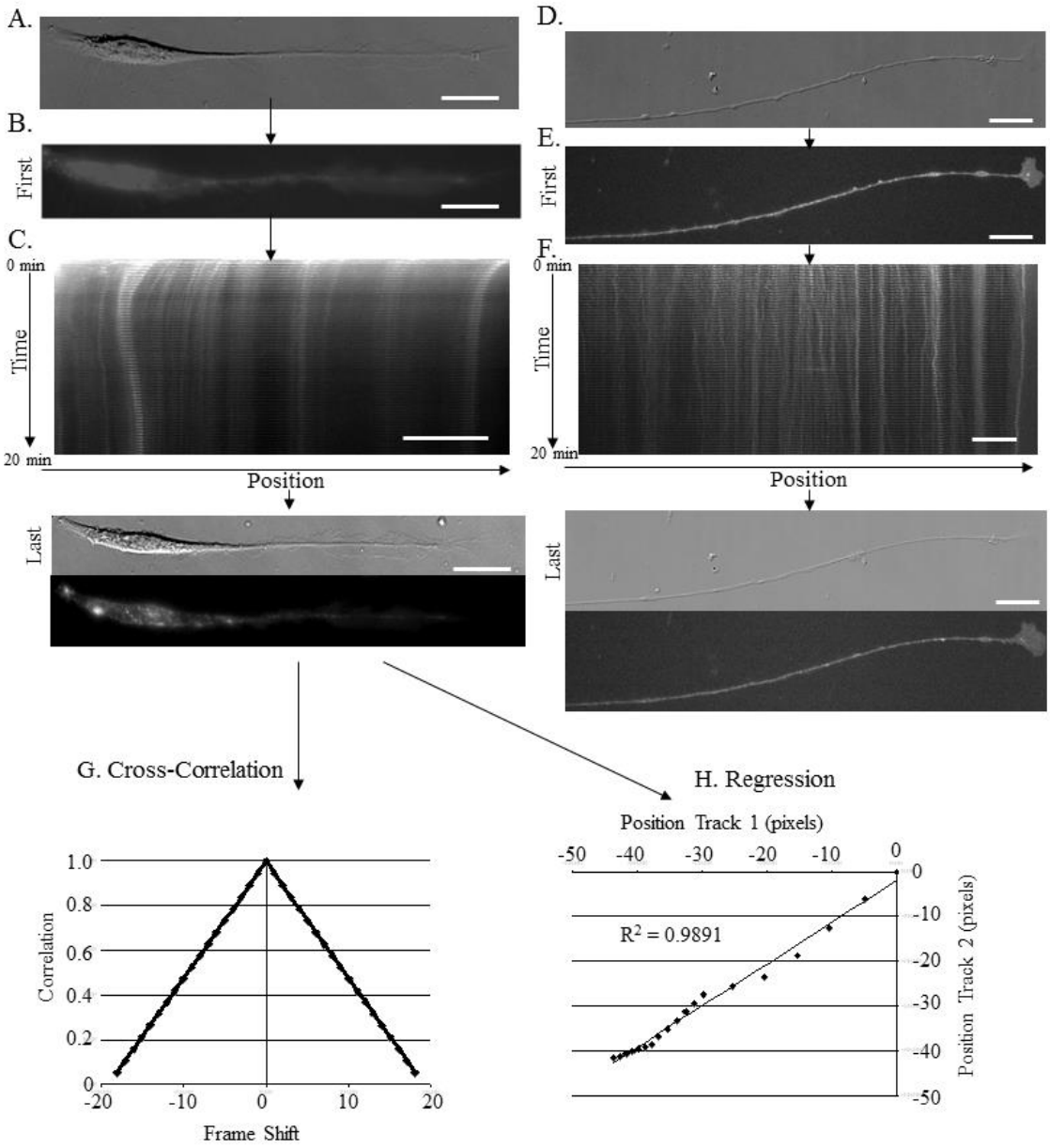

Figure 2-2: Methods of experimental analysis

Time lapsed images of the Schwann cells (A) and neurons (D) were taken under DIC and fluorescence to identify localization of fluorescent wheat-germ agglutinin (B, Schwann cells; E, neurons). Traces of the cellular projections at each time point were composed into a kymograph (C, Schwann cells; F, neurons) with tracks of wheat-germ densities being identified. Correlation of these tracks was identified using two methods of analysis: cross-correlation (G) and regression (H). Vertical arrows throughout figure represent process flow for imaging and analysis. Scale bars 20 μm.

Subsection 6: Analysis

Analysis was performed using MATLAB and all programs are available upon request. For analysis of correlation, particles were correlated by plotting the x-value corresponding to the position of one particle at a given time against the x-value corresponding to another particle at the same time [86,101]. This was done for all time points. It is important to note that this differs from conventional analysis of correlation and provides different measurements than traditional correlation length due to temporal and spatial resolutions and scope of our imaging techniques [111]. Traditional techniques are typically applied to individual lipid diffusion characteristics. The plot was fit using a linear regression and correlation was determined based upon the R^2 value of the fit. A high R^2 value represents two particles that move consistently in the same direction, although the magnitude of these displacements may not necessarily be the same (Figure 2-2H). An R^2 value of 0.9 or above was considered to represent strong correlation although the data appeared to be continuous and independent of the cut-off selection. Comparisons were made amongst all tracks in each video if the two tracks co-existed for over 1 minute. Lesser times were ignored due to inflated correlation among small data sets.

A second method, performed in MATLAB, utilized cross correlation analysis amongst tracks within a video and sequential frame shifts of the data to identify correlation regardless of slight temporal shifts in movement propagation. The sequences were normalized such that the autocorrelations at zero were equal to 1. The maximum correlation was then identified for each correlogram and a maximum value greater than 0.9 was used as a threshold for strong correlation between particles (Figure 2-2G). The

percentage of correlated particles in each sample (by either regression or cross correlation) was compared across cell type and across contact state.

To elucidate the role of regional velocity in the continuity of the membrane, the average velocity of all particles within a given sample was calculated by averaging the mean velocity of individual particles in the given sample. Also identified was the percentage of stationary tracks, defined based on a displacement less than that of a particle moving constantly at a velocity of 0.6 μm/min for the entirety of the movie. Statistical analysis was performed in Microsoft Excel (Microsoft) and SAS (SAS Institute Inc.). Means were compared using 1-way or 2-way ANOVA followed by Tukey's post hoc tests, and distributions were compared using Kolmogorov-Smirnov tests.

Subsection 7: Immunostaining

Samples were fixed in 4% paraformalin for 10 minutes. Following fixation, samples were washed three times with PBS followed by permeabilization with 0.2 % Triton-X 100 in PBS for 5 minutes. Again samples were washed three times with PBS and placed in blocking solution consisting of 10 % FBS in PBS for 25 minutes at room temperature. Post-blocking, the samples were washed three times with PBS. Primary monoclonal antibodies targeting talin (Sigma-Aldrich T3287), S100 (Sigma-Aldrich S2532) and SMI-31 (abcam ab24573) were diluted in blocking solution (1:750, 1:200, and 1:1000, respectively) and samples were incubated in the primary antibody for one and a half hours at room temperature. Following primary incubation, the samples were washed three times with PBS and placed for 2 hours in either Alexa Fluor 488-goat anti-mouse (Invitrogen A-11001) or Alexa Fluor 594-goat anti-mouse (Invitrogen A-11032) that had been diluted (1:200) in blocking buffer. The sample was washed three times with PBS, left in PBS and imaged. ImageJ (NIH) was used to determine fluorescence levels

for analysis performed Excel (Microsoft). A threshold level of 440 LUTs was chosen after identifying highly fluorescent patches on cells to have these mean values.

Section 3: Results

Subsection 1: Identification of Neurons and Schwann cells and labeling of plasma membrane

Schwann cells (Figures 2-1A and 2-1B) were initially identified by antibody labeling against S-100 as has been used previously [112]. Additionally, neurons (Figures 2-1C and 2-1D) were identified by antibody labeling against SMI-31, for identification of phosphorylated axonal neurofilaments. Subsequent live-cell imaging experiments relied on identification of SCs by their thicker projections (~3-4 μm) relative to neurons, bipolar morphology, and elliptical cell body (Figures 2-1A, 2-1C, 2-1E, and 2-1H). Neurons were identified based on observation of thin projections (~1 μm) and more rounded cell bodies.

Plasma membrane was labeled with wheat-germ agglutinin conjugated to Oregon Green 488. Fluorescent densities were observed along the projections of both cell types and allowed characterization of membrane dynamics in real time (Figures 2-1F and 2-1I). Neurons appeared healthy as evidenced by growth cone ruffling (Supplemental Figure 2-1A). In the rare case photodamage was witnessed by axonal blebbing, these samples were ignored (Supplemental Figure 2-1B). Due to incubation at 2°C endocytosis was minimized as evidenced by minimal uptake of fluorescently labeled dextran (Figures 2-1G and 2-1J). In SCs, slight uptake was observed at the cell body and lamellipodia. Additionally, fast rates of transport, indicative of WGA uptake and vesicular transport, were not observed following incubation at 2°C compared to a 4 hr incubation period at 37°C (Supplemental Figure 2-1C). Confocal imaging also revealed restriction of WGA to

the cellular surface and its absence within the cytoplasm of the cell (Supplemental Figure 2-1D).

Subsection 2: Membrane correlation and velocity in SCs and neurons

We generated kymographs (Figures 2-2A-F) to track the movement of particles throughout the duration of each experiment. We used two methods to identify the degree of correlation of particles with each other in each cell type (Figures 2-2G and 2-2H). Using cross-correlation analysis of all particles along a neuronal projection (Figure 2-2G), the percentage of correlated pairs with a maximum correlation value of over 0.9 was found to be 24.51%. This percentage rose significantly ($p<0.0145$, t-test) to 42.37% in SCs (Figure 2-3A). Similarly, the percentage of correlated pairs based on regression analysis (Figure 2-2H) and a minimum R^2 of 0.9 in all neurons was 7.07%. This percentage rose, though not significantly ($p<0.0757$, t-test) to 14.87% in all SCs (Figure 2-3B).

The length scale at which correlation occurs also depended upon cell type, and varied slightly depending on the method used to classify correlation. Using cross-correlation analysis, the median distance between correlated particles was found to be 39.05 μm for neurons and 35.86 μm for SCs (Figure 2-3C). This reduction in length scale in the correlated particles of SCs was not significantly different ($p=0.0814$, Kolmogorov-Smirnov). Similar analysis was performed using regression analysis; the median distance was 46.27 μm for neurons and 16.70 μm for SCs (Figure 2-3D). Distributions here were significantly different ($p<0.0001$, Kolmogorov-Smirnov). The results are suggestive of

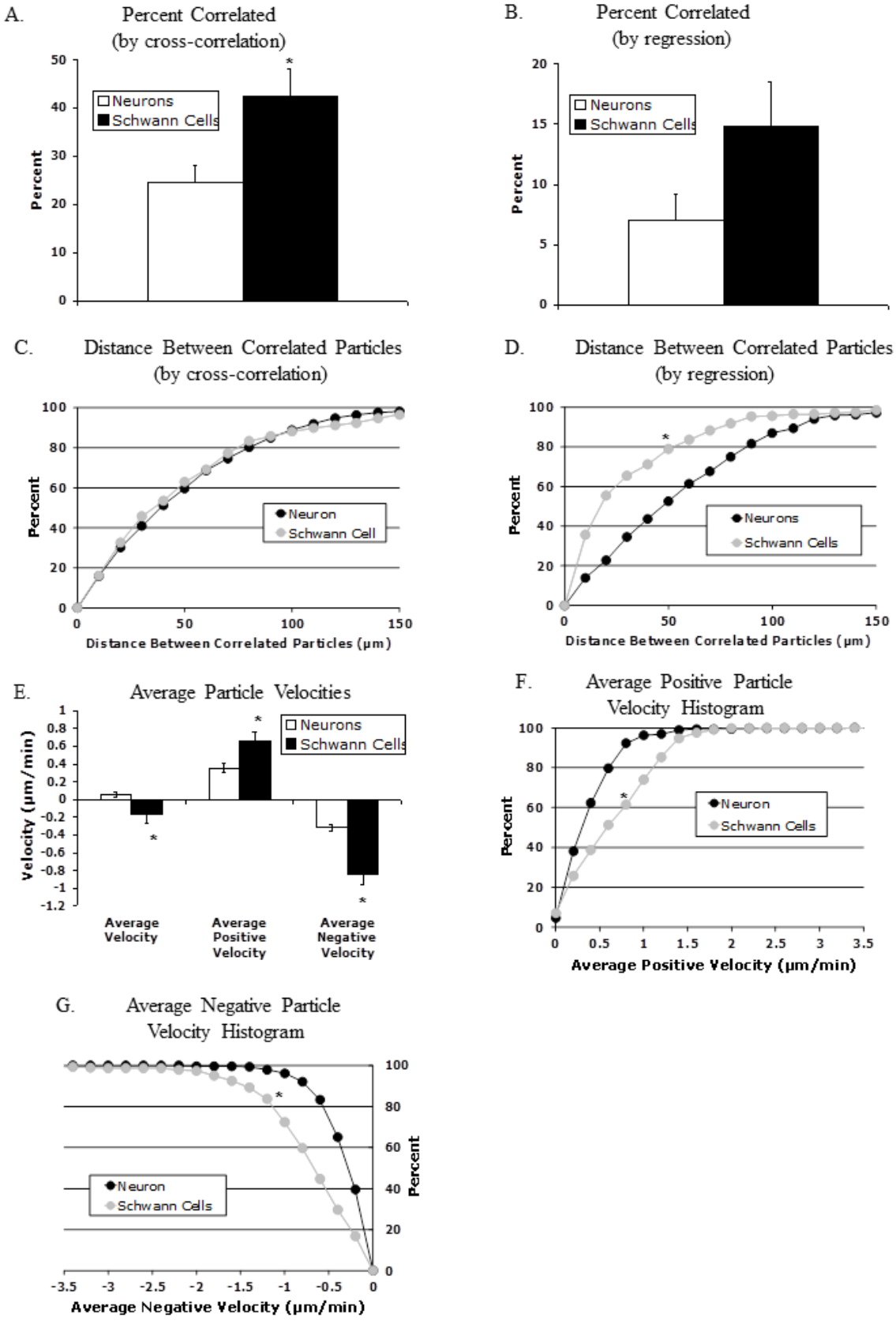
A.
Percent Correlated
(by cross-correlation)
Neurons
Schwann Cells
Percent
B.
Percent Correlated
(by regression)
Neurons
Schwann Cells
Percent
C.
Distance Between Correlated Particles
(by cross-correlation)
Neuron
Schwann Cell
Percent
Distance Between Correlated Particles (µm)
D.
Distance Between Correlated Particles
(by regression)
Neurons
Schwann Cells
Percent
Distance Between Correlated Particles (µm)
E.
Average Particle Velocities
Neurons
Schwann Cells
Velocity (µm/min)
Average Velocity
Average Positive Velocity
Average Negative Velocity
F.
Average Positive Particle
Velocity Histogram
Neuron
Schwann Cells
Percent
Average Positive Velocity (µm/min)
G.
Average Negative Particle
Velocity Histogram
Neuron
Schwann Cells
Percent
Average Negative Velocity (µm/min)

Figure 2-3: Membrane correlation and velocity by cell type

Percentage of correlated WGA pairs by cross-correlation (A) and regression analysis (B) *p < 0.015 (v. neurons, t-test). Values represent means ± SEM (n = 15). Cumulative histogram of the distance between correlated particles within given pairs for both cross-correlation (C) and regression analysis (D) *p < 0.0001 (v. neurons, Kolmogorov-Smirnov test). Average velocities of WGA particles (E) *p < 0.05 (v. neurons, t-test). Values represent means ± SEM (n = 15). Cumulative histogram of individual positive (F) and negative (G) velocities *p < 0.0001 (v. neurons, Kolmogorov-Smirnov test).

longer-range correlation throughout neuronal membranes and continuity over a shorter length scale in SCs. These metrics should not be confused with traditional correlation lengths of lipids; rather they simply refer to the distances between particles observed to possess correlated movement patterns. Both cross-correlation and regression analysis presented consistent trends in correlation in these initial comparisons; subsequent analysis was performed utilizing only cross-correlation analysis.

The velocity of particles on the membrane, corresponding to regions of the membrane, was identified to test whether physical mobility may affect or be affected by membrane correlation. The average velocity of neuronal membrane particles was found to be 0.052 μm/min with those of SCs averaging -0.165 μm/min (Figure 2-3E). Significance was identified for the two experimental populations (p = 0.0469, t-test). The average positive velocities also differed significantly (0.351 μm/min, neurons; 0.662 μm/min, Schwann cells; p = 0.0062, t-test), as did the average negative velocities (-0.319 μm/min, neurons; 0.843 μm/min, Schwann cells; p = 0.003, t-test). It is of note that the movement witnessed in Schwann cells was observed throughout the projection. Neuronal particles from the study possessed a reduced average positive velocity compared to those incubated at 37°C for 4 hours (Supplemental Figure 2-1D), characterized by the rightward shift in the graph and increase in half-max value (0.283 μm/min, no incubation;

0.459 μm/min, 4-hour incubation; $p<0.0001$, K-S). The particles observed after 4 hours thus likely contain an additional sub-population of mobile, presumably internalized particles in addition to less mobile particles seen under both incubation conditions.

Subsection 3: Membrane correlation and velocity in SCs and neurons by contact state

To test whether differences in membrane correlation between SCs and neurons were influenced by their contact with another neuron, we utilized cross-correlation analysis on subsets of neurons and Schwann cells subdivided by their contact state. Neurons contacting another neuron (NC) presented 21.3% correlated pairs, versus 27.3% correlated pairs in neurons not contacting another neuron (NNC; Figure 2-4A). In SCs the numbers were 40.2% and 44.3% for those in contacting and non-contacting states, respectively. We then tested whether pooling data along the entire length of the axon masked any such effects at the leading edges of the cell (i.e., growth cone or lamellipodium); however, analysis of correlation at the edge (< 30 μm) also failed to identify differences between the edge and the whole cell (Figure 2-4B).

Identification of particle velocities in the experimental groups by contact state provided average positive particle velocities in NCs of 0.301 μm/min and in NNCs of 0.394 μm/min (Figure 2-4C). In SCs, velocities were found to be 0.582 μm/s and 0.732 μm/s contacting and non-contacting states, respectively. Neuronal velocities were significantly different from their SC counterparts ($p< 0.05$, Tukey's t-test); however, despite a strong trend towards increased velocity in non-contacting SCs compared to contacting SCs, no significant differences were found within a cell type (Tukey's t-test). Again, characterization of the velocity at the edge (< 30 μm) failed to identify an edge

effect when compared to the whole cell (Figure 2-4D). Distributions of particle velocities were also investigated (Supplemental Figure 2-2).

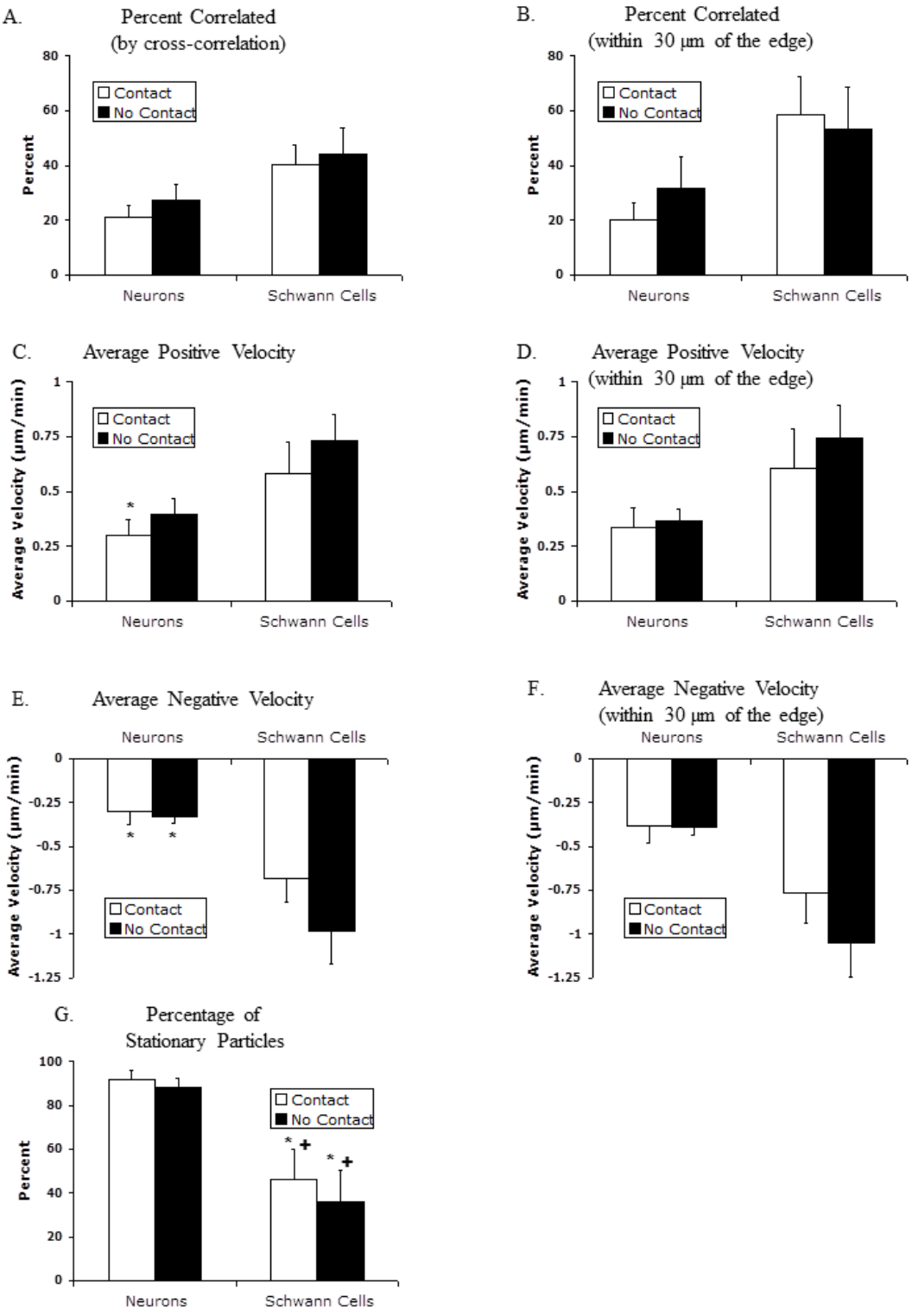

Figure 2-4: Membrane correlation and velocity by contact type

Percentage of correlated WGA pairs by cross-correlation along the entire projection (A) and within 30 μm of the edge (B). Values represent means ± SEM (n = 7-8). Average positive velocity of WGA particles along the entire projection (C) and within 30 μm of the edge (D) *p < 0.05 (v. Schwann cells without contact, ANOVA with Tukey's post-hoc test). Values represent means ± SEM (n = 7-8).). Average negative velocity of WGA particles along the entire projection (E) and within 30 μm of the edge (F) *p < 0.005 (v. Schwann cells without contact, ANOVA with Tukey's post-hoc test). Values represent means ± SEM (n = 7-8). Percentage of particles deemed stationary with velocity less than 0.01 μm/s *p < 0.05 compared to contacting neurons, +p < 0.05 compared to non-contacting neurons, (ANOVA with Tukey's post-hoc test). Values represent means ± SEM (n = 7-8).

There was observable contact state dependence witnessed in the average positive or negative velocities both along the entire cell or localized to the edge (Figures 2-4C-F). The percentage of stationary particles (those below 0.6 μm/min) was identified as an indicator of relative membrane immobility. In the case of neurons, NCs possessed 91.51% stationary particles while NNCs had 88.96% stationary particles (Figure 2-4G). Particles of SCs were more mobile with only 46.33% and 36.27% of particles in SCCs and SCNCs identified as stationary. Using a two-way ANOVA, a strong cell type dependence was identified ($p < 0.00005$, ANOVA)

Subsection 4: Levels of the adhesion molecule talin in contacting versus non-contacting cells

The levels of the adhesion molecule talin were quantified by the intensity of immunostaining as an indirect measure of adherence (Figure 2-5B). NCs had the highest percentage of staining along their projections at 31.68%. NNCs were stained along 28.79% with SCCs stained along 26.39% and SCNCs stained along 11.15%. Neurons overall demonstrate a trend towards more stable adhesions in the form of talin compared to SCs, though the development of contact in SCs also trends towards an increase in talin

densities. No significance was identified between any of the groups using both a two-way ANOVA and Tukey's post hoc test, likely due to the low sample number.

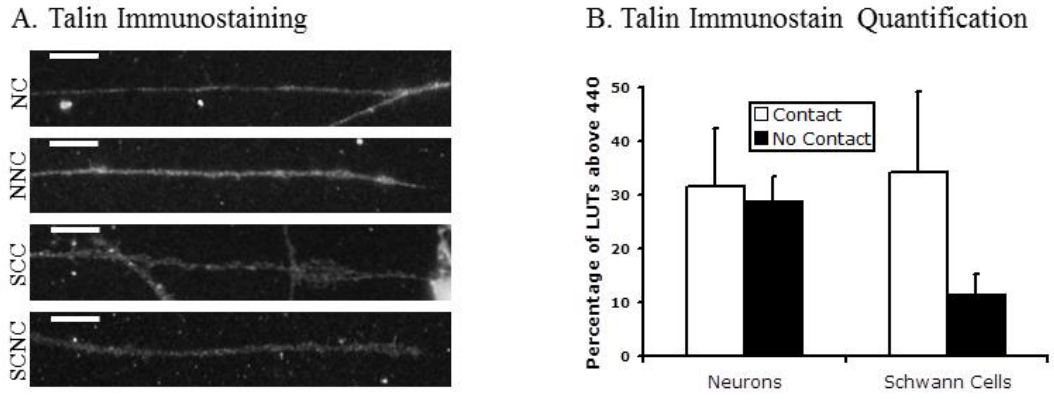

Figure 2-5: Talin immunostaining

Immunostaining for talin levels (A) in neurons with contact (NC), neurons without contact (NNC), Schwann cells with contact (SCC), and Schwann cells without contact (SCNC). Quantification of immunostaining levels by thresholding (B) revealed no significance (ANOVA, $p > 0.05$). Scale bar, 10 μm.

Section 4: Discussion

Using fluorescent WGA as a membrane label provides the unique ability to track regional membrane movement during the growth and migration of cells. Previously, membrane correlation has generally been studied on a much smaller scale, identifying extremely localized diffusion of individual particles in membrane patches and lipid rafts [113,114]. Applying time-lapse fluorescence microscopy to cells fluorescently labeled with WGA as a marker for the movement of membrane patches allows identification of membrane correlation and continuity on a larger scale. Earlier work has focused on the localization of membrane insertion and membrane flow [41-43]. Our study focuses on more stable regions of the membrane to identify the dynamics of whole cell mechanics during normal growth and function.

Subsection 1: Quantitative analysis of continuity in the membrane

Multiple methods of analysis were used to identify correlation between particle pairs. Regression analysis was employed following the precedent of previous literature [86,101]; however, this method relies implicitly on a dependence of one particle on the other. In this study, because neither particle within a pair is explicitly dependent on the other, analysis using cross-correlation may provide a more appropriate characterization of the relationship. It was shown that independent of methodology, levels of correlation displayed similar trends (Figures 2-3A and 2-3B).

Quantitative characterization and analysis of particle mobility allows for a more rigorous investigation due to the level of detail and number of identifiable parameters such as relative positions and velocities. Comparisons between these variables can be easily obtained to explore previously unidentified relationships and describe the mechanical connectivity. Additionally, quantitative analysis allows for efficient, unbiased processing of data to provide impartial results. In future studies, one might be able to comb through large sets of data and quickly determine localization of membrane expansion and contraction.

Subsection 2: Influence of cell type on membrane correlation

One particular finding of interest is that although both cell types possess strong bipolar morphologies, a cell type influence exists in the correlation of membrane patches when comparing SCs and neurons (Figure 2-3A and 3B). A major contributor to this difference is likely the mobility and cytoskeletal architecture of each cell type. While neurons of the CNS have been known to migrate along glia during development [115], this behavior opposes what is known to occur in the PNS, especially in DRGs where neurons secure their cell bodies and proceed to extend axons [116]. Once migrating SCs

become committed to a myelinating phenotype, their cytoskeletal composition changes and they lose their ability to migrate [93]. Additionally, non-myelinating SCs are known to respond to signals, such as NGF, during development and injury to migrate along axons in the PNS [93,117]. This migratory phenotype is consistent with the higher level of regional mobility in SC membranes compared to those of neurons (Figure 2-3E). It is therefore likely that the increased velocity is responsible for a portion of the correlation increase witnessed in SCs compared to neurons.

In the case of SCs, there is obvious, movement along the entirety of the cell. While migrating, typically, the distal edge of the cell extends and the cell body follows with some regularity. Not only does this extension happen at a larger rate than that of axonal growth cones, the propagation of this movement is generally limited to a much smaller portion of the cell in neurons compared to SCs. Due to the mechanics of the movement, it is likely that higher levels of membrane correlation allows the SC membrane to mechanically compensate with the dynamic movement. It is of note that correlation of low velocity particles may be underestimated due to the inability to distinguish the relationship of truly stationary particles leading to their determination to be uncorrelated.

Regional continuity in the movement of plasma membrane is likely to be influenced by the underlying cytoskeletal framework of the two cell types; however, the length scale over which such correlation occurs may be different from that in the cytoskeleton. Neuronal membranes were shown to possess a larger length-scale over which correlation occurs (Figure 2-3D); this length-scale is considerably larger than that previously reported for cytoskeletal continuity (<20μm; Chetta et al., 2010, Figure 6E

[101]) in a similar experimental model system. Microtubules of neurons average around 100 μm whereas the microtubule networks of migratory SCs are much less mature with length scales around 20 μm [93,118]. The variation in correlation length-scale may be directly attributable to immaturity in the cellular cytoskeleton and dynamics therewith.

Subsection 3: Influence of contacting state on membrane correlation

While the establishment of contact was shown to limit the mobility of the membrane (Figures 2-4C and 2-4E), our data fails to identify a role for contact in affecting the correlation of the membrane in either cell type (Figure 2-4A). In neurons, although cell-adhesion densities increase upon contact, thereby limiting growth cone motility and initiating synapse formation, this does not appear to limit the overall continuity of the cellular membrane (Figure 2-4A) [119]. In SCs too, focal adhesions have been hypothesized to increase following the establishment of contact [34]. However, such contact *in vitro* has been established to be insufficient to induce myelination [104]. Furthermore, the induction of myelination, not simply the establishment of contact, is required for wide-scale cytoskeletal reorganization of all cytoskeletal classes [104,120]. It is therefore likely that much of the observed correlation at our intermediate resolutions (microns) is reliant, directly or indirectly, on cytoskeletal stability and organization in addition to the movement of the cell. To more specifically identify the influence of contact state, the specific changes in both movement and correlation were identified at the edge (Figures 2-4B, 2-4D, and 2-4F). The variation in the data between the edge and the overall cell is so small that this should serve to support the fact that contact establishment has no observable effect.

As an initial step in understanding mechanisms underlying changes in mobility with contact, we analyzed the presence of talin, a cytoskeletal protein concentrated at

focal cell-substrate adhesions. While the average levels of talin along projections or in the vicinity of the cell terminal did not present significant differences across cell types, there was an identifiably lower amount of talin staining in SCs that had not established contact with other cells (Figure 2-5B). In SCs, though not neurons, talin levels are inversely proportional to the level of membrane correlation. This may also be a consequence of reduced adhesion in more mobile cells, though this hypothesis remains to be tested. It is possible that the establishment of focal adhesions compartmentalizes the membrane to a degree, limiting membrane correlation and continuity. Further investigation into the role of both cell-cell and cell-substrate adhesion, both of which change dramatically during myelination, fasciculation, and synapse formation [92,103,112], would be required to make a definitive statement on the role of adhesion on membrane correlation.

Subsection 4: Differences in membrane velocity amongst cell types

The major focus of this work was to test the regional correlation of movement rather than examine the mobility of freely diffusing lipids within the plasma membrane. However, it is instructive to place our results in the context of related studies both in neurons and non-neuronal cells. At first glance, our results appear very different from membrane addition and flow rates observed in previous experimental systems, to the point of being nearly an order of magnitude smaller [41,42]. However, a closer examination of differences in methodology and the experimental model provide some insight into these differences, and, in fact, suggest some conceptual consistency.

A strong possibility exists that the brightly fluorescent regions we observed correspond with the approximately 30% of stable particles noted by Dai and Sheetz, which were posited to be attached to the cytoskeleton, but not considered in their analysis [41]. Such stable particles were also noted in other similar studies using larger beads

[36,37]. Furthermore, they identified retrograde flow of membrane in embryonic chick DRGs due to relative differences in tethering forces at both proximal and distal regions of the axon [41]. In contrast, the consistency in talin staining along the projections of postnatal rat DRG and SC in our cultures points to the likelihood of a more consistent or less predictable tension. This could provide additional rationale for the lack of observed membrane flow in our experimental system, and are consistent with the low average velocities but the relatively higher directional velocities that we observed. These observations are also consistent with observations in other classes of migratory cells that are known to not possess directed membrane flow [43]. A direct comparison of different cell types using identical experimental methodology may address some of these hypotheses.

A key factor that could influence the interpretation of our data is the possibility that WGA is being internalized. Four observations suggest that this is highly unlikely. First, internalization was blocked methodologically by incubation of WGA during refrigeration. Second, immediately following this block, dextran co-incubated with WGA was internalized at the growth cone and cell body, but not along the axon. Third, rates at which these internalized dextran particles moved were not sufficient to deposit them along axons, following internalization at the growth cone, within the time frame of our movement analysis. Finally, we compared WGA particle movement in time-lapse movies captured immediately after blocking internalization versus those captured 4 hours later, during which time internalization may have occurred (Supplemental Figure 2-2D). Our data suggest that at the later time point, internalized WGA moves at a faster velocity and with more frequent changes of direction than at the earlier time point. This more mobile

sub-population of particles reflects similar movement to that of Rab5 during early phases of endocytosis [51].

Section 5: Conclusions

The methods presented here provide a unique look into large-scale membrane mobility. Quantitative analysis allows for unbiased conclusions about the membrane dynamics. The cellular membrane of SCs displays a markedly higher level of correlation amongst membrane patches compared to neurons. This relationship appears to correlate with increases in velocity and is inversely proportional to the presence of adhesive markers. These findings support an intuitive model where two mechanisms could work antagonistically to influence the level of membrane correlation and relative continuity. First, a higher velocity movement of the cell leads to increased membrane correlation due to directional forces generated by the cell to develop motion. Conversely, focal adhesion development and associated cytoskeletal stability would serve to resist these forces generated to develop motion.

It would be interesting in future studies to further investigate the role of cytoskeletal filaments and their associated proteins with respect to membrane continuity, as well as compare the response of neurons and Schwann cells to the direct application of a load. Exploration of changes in SC membranes following myelination would also be an appealing extension due to the large-scale cytoskeletal changes known to occur during myelination [93].

Section 6: Supplemental Figures

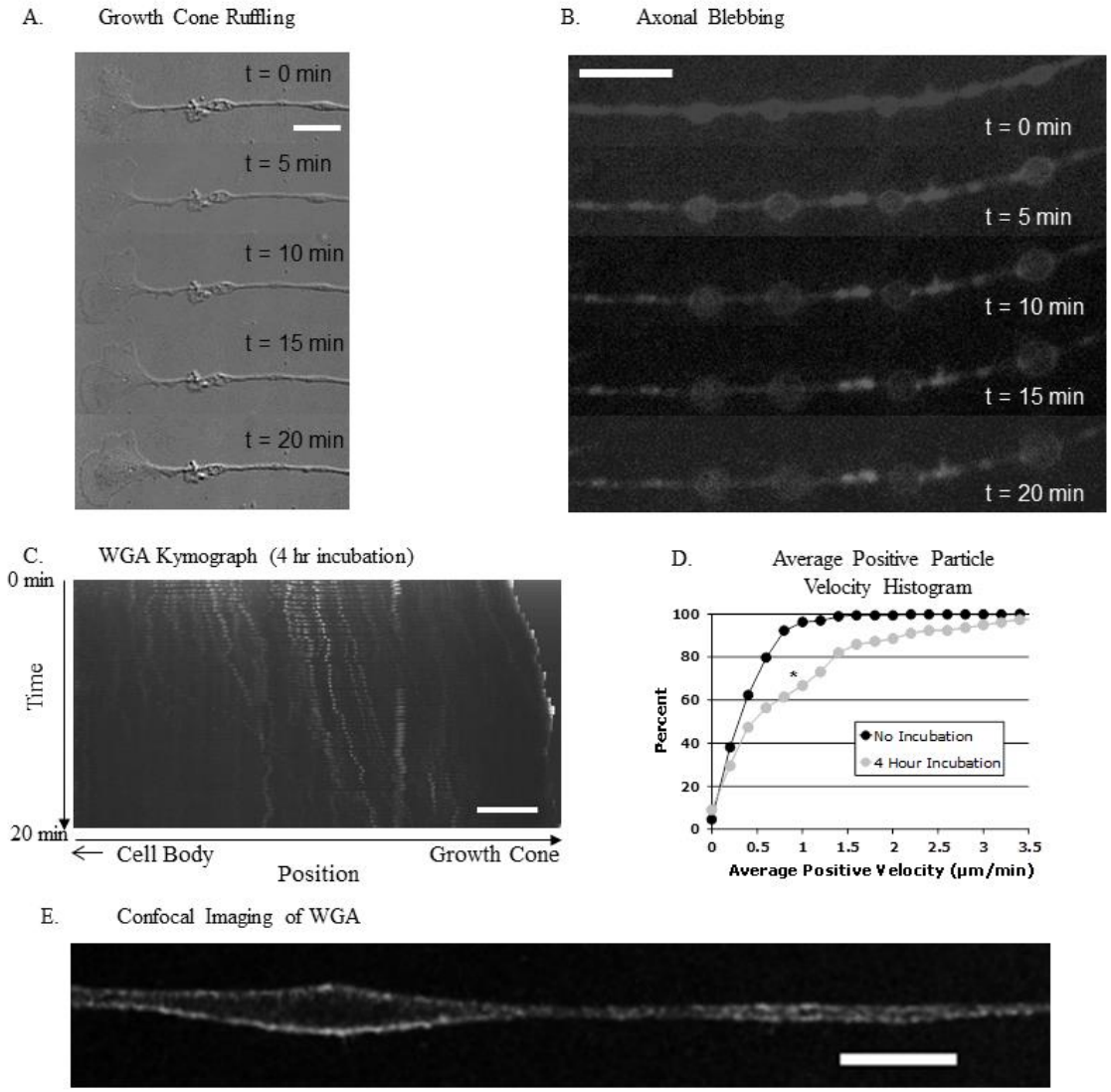

Figure 2-1 (Supplemental): Control experiments

Growth cone ruffling was observed in non-contacting neurons (A) as an indication of overall neuronal health, scale bar 10 μm. Axonal blebbing (B) was observed in a limited number of neurons. These neurons were excluded from the study, scale bar 10 μm. High velocity membrane movement was observed in axons that were given 4 hours to recover following WGA application (C), scale bar 20 μm. To exclude internalized membrane, the 4-hour incubation was removed from the protocol. Cumulative histogram of individual positive particle velocities on neurons (D) *$p < 0.0001$ (v. no incubation, Kolmogorov-Smirnov test). Confocal imaging of fluoresce revealed the absence of internalized WGA following initial incubation (E), scale bar 20 μm.

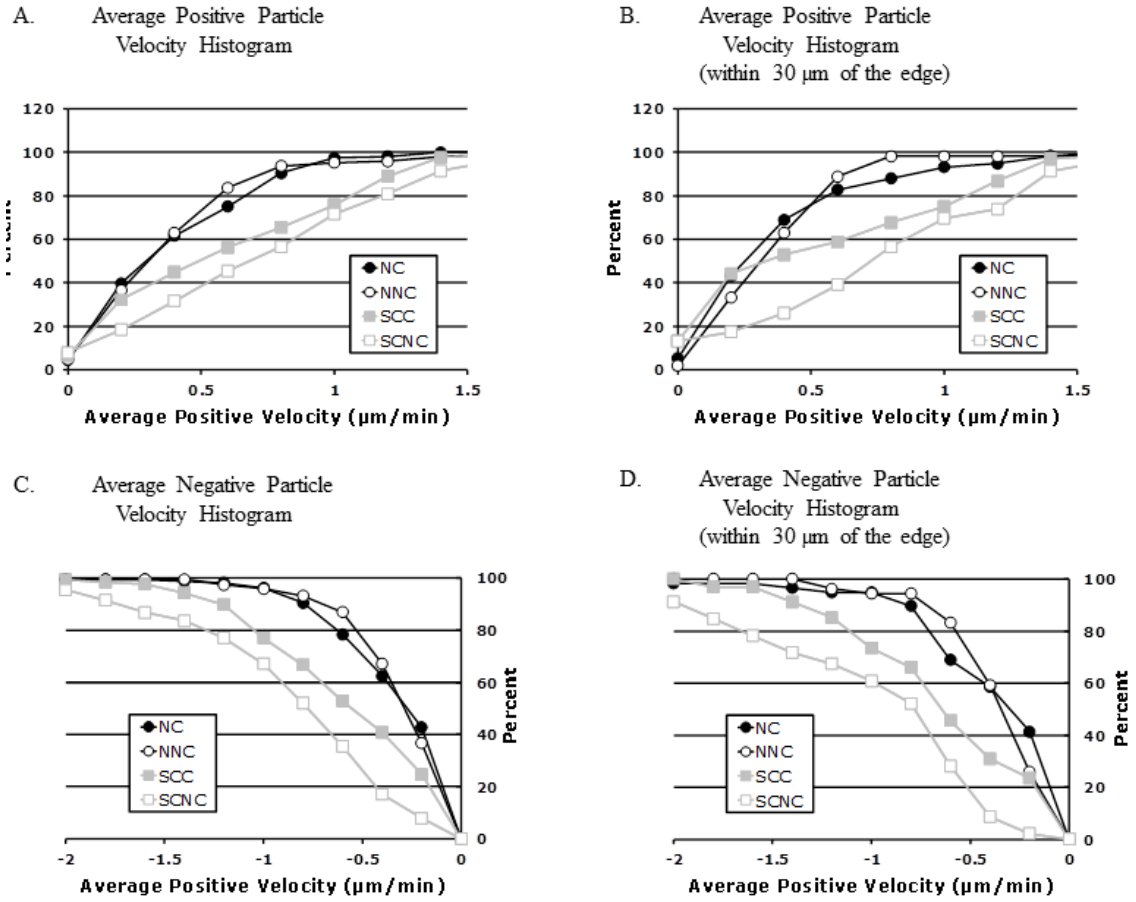

Figure 2-2 (Supplemental): Particle velocity histograms by cell type and contact state

Additional histograms of positive (A) and negative (C) particle velocities (analogous to Figures 3F and 3G). Focused characterization of the velocities of particles in regions within 30 μm of the edge (B and D) yielded little difference. Significant differences ($p<0.05$, Kolmogorov-Smirnov) are as follow: (A) NC vs. SCC, NC vs. SCNC, NNC vs. SCC, NNC vs. SCNC; (B) NC vs. SCNC, NNC vs. SCC, NNC vs. SCNC, SCC vs. SCNC; (C) NC vs. SCC, NC vs. SCNC, NNC vs. SCC, NNC vs. SCNC, SCC vs. SCNC; (D) NC vs. SCC, NC vs. SCNC, NNC vs. SCC, NNC vs. SCNC.

Chapter 3: Ribosomal trafficking in Schwann cells depends on early myelination cues

Section 1: Introduction

Schwann cells (SCs), a major cell type of the peripheral nervous system, are tasked with supporting neurons in numerous ways, from enhancing electrical conduction [121] to providing trophic factors for axonal growth and regeneration [23,122]. In this capacity, they possess a distinctive bipolar architecture; internode distances of up to 500 μm require distances between the Schwann cell body and distal processes to reach over 200 μm [123]. As in neurons, another polarized cell of unusual geometry [124], myelinating and unmyelinating SCs appear to synthesize particular proteins at the site of demand within projections, rather than in the cell body [48].

In contrast to ER-bound ribosomes, which are mainly tasked with the production of membrane-associated or secreted proteins [125-127], cytosolic protein synthesis occurs on free ribosomes and is typically responsible for producing many proteins locally, including intracellular signaling molecules, transcription factors, and cytoskeletal elements [128]. Evidence of local protein synthesis in myelinating cells remains mostly indirect, based on the presence of mRNA in isolated polysomes and granules within both unmyelinating and myelinating glial cells [129]. Additionally, myelin basic protein (MBP) mRNA has been observed to be distributed throughout SC and oligodendrocyte projections [48-51], and radiolabeled MBP (2 min) appears early compared to the cell body-synthesized protein PLP (30 minutes) in the myelin fraction of oligodendrocytes, providing additional evidence for translation of MBP within the myelin fraction [52].

Lacking from our current understanding is how these free ribosomal populations are distributed in Schwann cells during development and how ribosomal distribution is influenced by Schwann cell interactions with neurons. Developing a better understanding of these mechanisms may provide better insight into protein synthetic dynamics as well as the stability of observed ribosomal structures, in preparation for translation of Schwann cell proteins as well as, intriguingly, those potentially transmitted to neurons [27,28]. We used quantitative biological and theoretical approaches to probe the hypothesis that the induction of myelination would increase trafficking of ribosomes, to account for the required increase in production of myelin associated proteins. Expression of fluorescently labeled ribosomal subunits in primary Schwann cells allowed us to track ribosomal transport in real time, and quantify changes in patterns of ribosomal localization and transport during both their initial interactions with neurons in culture and in early phases of myelination. Multiple regression analysis and the development of a data-driven rate kinetic model enabled us to develop further insight into these changes. Our data suggest that stable ribosome-enriched foci appear early during Schwann cell projection extension and are maintained during early stages of myelination. However, transport of new ribosomes into projections slows upon induction of myelination, primarily due to increased conversion of anterograde (outward) moving particles to a stationary pool.

Section 2: Materials and methods

Subsection 1: Animal usage and euthanasia

Animal usage was in accordance with protocols approved by the UCSD Institutional Animal Care and Use Committee (IACUC). Pregnant female rats were euthanized by asphyxiation with CO_2 followed by confirmation via secondary means

(removal of major organs). P2 neonates were incapacitated with CO_2 followed by euthanization via decapitation.

Subsection 2: DRG collection and culture

DRG culture methods were adapted from previously published methods [130]. Dorsal root ganglia (DRGs) were removed from E15 Sprague-Dawley rats in HBSS. DRGs were dissociated in trypsin for 30 minutes at 37°C. Following trypsinization, samples were washed 3x in fresh pre-warmed media. DRGs (~30,000 per plate) were plated on laminin-coated glass coverslips placed within 24-well plates supplemented with 500 µl of prewarmed DRG media consisting of MEM with 10% FBS, 2% B27, 1 ng/ml NGF, and 1 % Penicillin/Streptomycin. One day post plating, culture media was supplemented with 1 ug/ml FdU to eliminate contaminating fibroblasts and Schwann cells. Media was alternated every 2-3 days between FdU application and fresh media for a period of two weeks to obtain a mostly purified neuronal culture (Figure 3-1A).

Subsection 3: Schwann cell isolation

Schwann cells were isolated and cultured per previously published methods [130]. Primary Schwann cells were obtained from the sciatic nerves of ~10 P2 Sprague-Dawley rat pups (20 nerves). Nerves were dissected into 14 ml of L15 media then spun down at 3000 rpm for 2 min. Media was aspirated off and nerves were resuspended in 2 ml L-15 and 1 ml 10 mg/ml collagenase type P and incubated at 37°C for 45 min, mixing every 10 min. Tissue was spun down for 2 min at 1000xg, media aspirated off and pre-warmed digestion solution added (3 ml 0.25% trypsin and 1 ml DNase [1.2 mg/ml]) Sample was incubated for 15 minutes at 37°C. Following incubation, the reaction was halted by supplementing sample with 5 mL DMEM and 10% FBS. Sample was centrifuged for 2

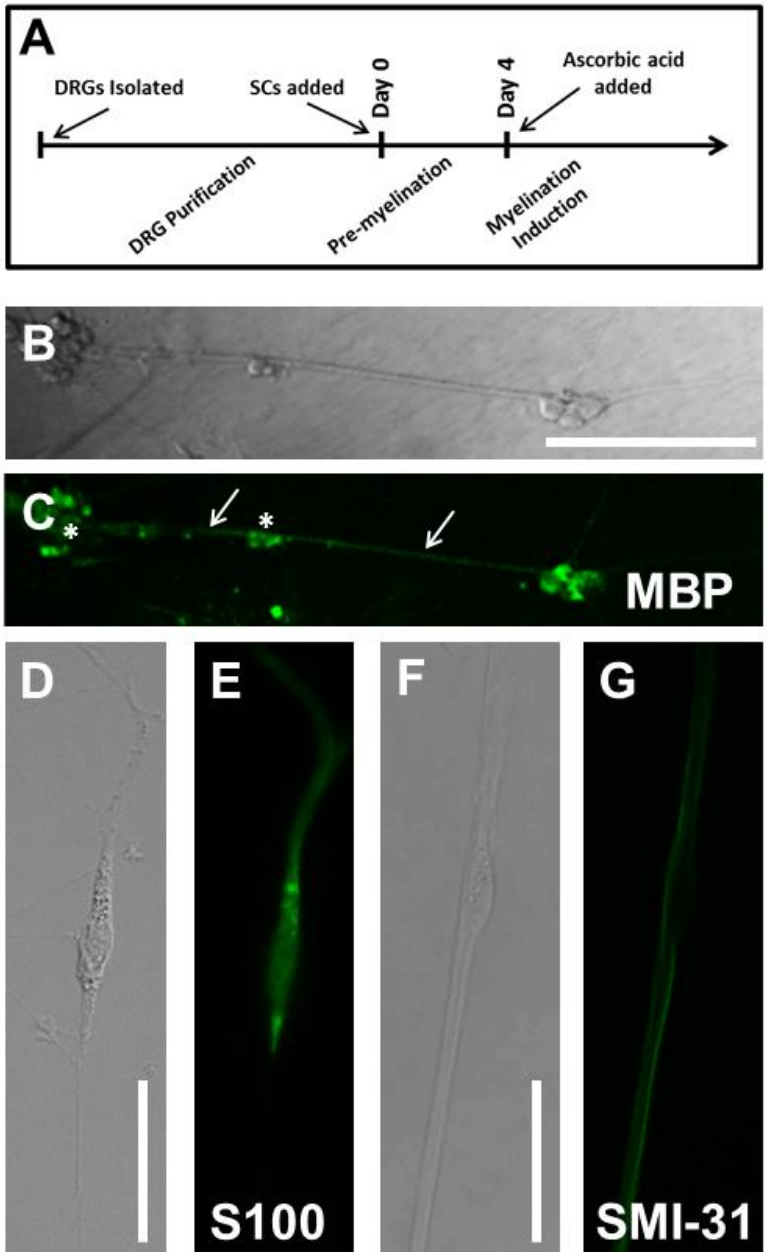

Figure 3-1: Experimental Design

(A) Cell culture timeline. All experimental days reference days since Schwann cell addition to neuronal culture; Confirmation of myelination protocols and cell culture techniques was observed through immunolabeling: (B) DIC image of Day 14AA culture indicates several clusters of Schwann cells and neurons (stars) as well as fascicles of myelinated DRG axons (arrows); (C) MBP immunostain of Day 14AA culture shows low levels of MBP expression, indicative of early myelination; (D) DIC image of cultured Schwann cells at Day 1 (E) S100 immunostain identifies cultured Schwann cells; (F) DIC image of a single Schwann cell (star) abutting neuronal processes; (G) SMI-31 (phosphorylated neurofilament) immunostain identifies location of neuronal processes relative to Schwann cell body (star); Scale bar B/C: 200 µm, D/E/F/G: 50 µm

minutes at 1000xg followed by two washes with 10 ml of ice cold L15 media followed by 1000xg centrifugations. Samples were supplemented with 5 ml of media and triturated. Cells were spun down at 1000xg and media removed for transfection.

Subsection 4: Transfection

Nucleofection was performed according to manufacturer's instructions (4D-Nucleofector™ System, Lonza AG, Switzerland) using P3 primary cell solution and program setting DC-100 to transfect. Either 3 μg of L4-GFP plasmid (a generous gift of Tim Krüger [131] or control GFP plasmid (Lonza AG, Switzerland) were used.

Expression persisted for up to two weeks in culture. However, the percentage of cells expressing the plasmid decreased over time, as has been previously reported [132]. Thus, our experimental time course was conservatively chosen to span early phases of myelination, and includes cells from one day post transfection (Day 1) to cells one week post transfection (Day 7) (Figure 3-1A).

Subsection 5: Induction of myelination

Myelination was induced with ascorbic acid per published protocols [133]. On the fourth day of co-culture with neurons, Schwann cell media was supplemented with 50 μg/ml ascorbic acid to initiate the process of myelination. Cells treated with ascorbic acid and observed were designated (Day 7AA) in contrast with untreated cells (Day 7 No AA). Myelination was confirmed using immunocytochemistry at day 14 (Figure 3-1C).

Subsection 6: Immunocytochemistry

Immunocytochemistry was performed at various developmental time points, using published protocols [2]. Samples were labeled with one or a combination of the following primary antibodies: mouse anti-S100 (Sigma-Aldrich S2532), mouse anti-SMI31 (abcam

ab24573), mouse anti-MBP, human anti-Ribo-P (Immunovision HPO-0100), mouse anti-RPL4 (Sigma-Aldrich WH0006124M1), mouse anti-tubulin (Sigma-Aldrich T9026). Appropriate species specific fluorescently-labeled secondary antibodies were used to visualize primary antibody localization. Secondary antibodies used included: Alexa Fluor 488-goat anti-mouse (Invitrogen A-11001), Alexa Fluor 594-goat anti-mouse (Invitrogen A-11032), Alexa Fluor 594-goat anti-rabbit (Invitrogen A-11037), and Alexa Fluor 594-goat anti-human (Jackson Immunoresearch 109-585-003). Desired samples were incubated for 30 minutes prior to mounting in Alexa Fluor 594-phalloidin (Invitrogen A-12381) to visualize actin.

Analysis for co-localization was performed using ImageJ plugin JACoP.[134] Images were analyzed for overlapping expression using the Manders coefficient, which incorporates both position and fluorescence intensity into assessment of co-localization [135].

Subsection 7: Imaging

Cells were imaged using a Leica SP5 system within an environmental chamber (Tokai Hit, Japan) that, for live-imaging experiments, enabled maintenance of the environment at 37°C and 5% CO_2. Standard lasers and filters were used. An argon laser enabled excitation at 488nm with HeNe lasers for 594nm. Emission was captured between 500-550 nm (GFP, Alexa-Fluor 488) and 600-650 (Alexa-Fluor 594). Laser power and gains were adjusted to provide best images for each sample.

Time course images of transfected cells were captured at 5 second intervals for a period of 5 minutes. The capture rate and imaging period were chosen based upon several factors including anticipated transport rates, desired resolution, and minimization of photobleaching and phototoxicity.

Subsection 8: Image processing and analysis

Custom Matlab (Mathworks, Inc.) programs were modified from previous studies [2,136]. to convert time course images into a kymograph. Kymographs allow for visualization of changes in an intensity profile of a 1-dimensional trace over time with the time variable displayed along the y-axis and cellular position along the x-axis. Kymograph traces in our analysis were made along the long axis of the SC projection allowing visualization of transport throughout the projection with a thickness of 9 pixels. Application of a standard deviation filter in MATLAB to processed kymographs enabled background and noise suppression with signal enhancement, by replacing a given pixel with the standard deviation of its surrounding 3x3 pixel neighborhood. At this point, the individual traces were reduced to a central 3-pixel thickness encompassing the centerline of the projection. Kymographs were analyzed for both ribosomal distributions along the projection as well as transport characteristics of mobile ribosomal populations.

For characterization of ribosomal distributions, kymographs were averaged along the y-axis providing an average projection profile for the five minute imaging duration. The profile was manually segmented to separate the cell body from the projection for characterization. Stable populations of ribosomes were noted within the projections through identification of peaks in the average intensity above background fluorescence levels (>3x). Peaks within 5 pixels (~2.5 μm) were counted as a single peak to minimize double counting due to inherent noise from averaging. Average fluorescence levels were identified for both the cell body and projection regions. Peak distance values were determined from identified peak locations and specified projection start.

Transport parameters were computed based upon manual identification of mobile ribosomal particles with a continuous trajectory from frame to frame and an intensity of

at least 3x above background. Traces were made of moving particles, and parameters for each ribosomal particle were computed. Mean particle parameters were computed and presented as average values. Net velocity was computed based on the aggregate distance traveled by all particles in a given sample divided by the time window of observation [6]. This provides a reasonable surrogate for the collective level of transport conducted by a cell throughout the duration of the 5 minute imaging window.

Subsection 9: Multiple regression analysis

Multiple regression analysis was performed on the z-scored data of all individual traces within an experimental group. The dependent variable (net displacement) was regressed against the independent variables average velocity, total duration, anterograde velocity, anterograde duration, stationary velocity, stationary duration, retrograde velocity, and retrograde duration. Higher β-weights indicate a stronger contribution to the regression model.

Subsection 10: Modeling

A ribosomal transport model was implemented using a rate kinetics model to evaluate transitions from stationary, retrograde, and anterograde ribosomal populations. The model, modified slightly from its original form [137], used a system of coupled differential equations for each population:

$$\frac{d[Stat]}{dt} = k_{-1}[Ant] + k_{-2}[Ret] - k_{+1}[Stat] - k_{+2}[Stat] - k_{+3}[Stat] \quad (1)$$

$$\frac{d[Ant]}{dt} = k_{+1}[Stat] - k_{-1}[Ant] \quad (2)$$

$$\frac{d[Ret]}{dt} = k_{+2}[Stat] - k_{-2}[Ret] \quad (3)$$

The model schematic can be seen in Figure 3-7. Particle amounts while modeled as concentrations within the equations refer to instantaneous particle counts. The model was implemented in MATLAB (MathWorks, Natick, MA) using the differential equation solver ode45 which implements a Runge-Kutta method with a variable step size. In order to find a unique best solution, rates were varied between 0.001 and 1.001 in 0.01 steps for each rate constant. Sensitivity analysis for each model parameter was performed by varying each parameter over its allowed range, and plotting model outputs. Best fit was determined by minimizing the mean square error (MSE) between modeled parameters and experimental data for net displacement and the number of particles in each state. Initial model fit was made using the time points untreated with ascorbic acid. A fit was then made between the Day 4 time point of the fit (when ascorbic acid was added) and the Day 7 treated group. Within the model, net velocity was calculated by multiplying the instantaneous particle populations of each state by the instantaneous velocity of the population for a given time step and summing the two populations. Experimentally measured velocities were fit using linear regression to provide an approximate instantaneous velocity (Table 3-1).

Subsection 11: Statistical analysis

In all cases a 1-way ANOVA was performed across all experimental groups (Day 1, Day 3, Day 7 No AA, Day 7AA). Additionally, Tukey's HSD was performed post-hoc to determine significant differences between individual groups of interest while accounting for multiple comparisons. Differences were considered significant for $p < 0.05$. A minimum sample size of 7 was used for each group, corresponding to a statistical power of 0.91 and effect size capable of being detected of 0.96.

	Velocity (μm/s)			
	Anterograde		Retrograde	
	Ax	B	Ax	B
No AA	-0.02655	0.827899	-0.00584	0.001029
AA	-0.03348	0.855631	0.001029	-0.48095

Table 3-1: Model parameters

Constants for linear fits of velocities used in transport model for each experimental state (based on fits of experimental velocity data)

Section 3: Results

Subsection 1: L4-GFP transfection and ribosomal expression in Schwann cells

We confirmed and characterized transfection of SCs with the L4-GFP plasmid (Figure 3-2A). Only ~15% of cells were successfully transfected; however, comparison of transfected cells with fixed cells immuno-labeled for ribosomal protein L4 showed strong agreement in localization (Figure 3-2B). Of particular note was the punctate expression within the nucleolus and higher relative fluorescence within the cell body compared to the projection of the SC. Comparison with Ribo-P, a marker for phosphorylated ribosomes, showed strong co-localization outside of the nucleus (Figure 3-2C). The expression profile of L4-GFP also differed greatly from that of GFP expression (Figure 3-2D), which was evenly distributed in low levels throughout the entirety of the SC.

Subsection 2: Ribosomal expression characteristics within Schwann cell projections

Following successful transfection, SCs associated with neurons were identified based on the position of cell bodies and projections of each cell type. We investigated these cells to determine the development of ribosomal distributions within SC projections over time and following myelination induction (Figure 3-1A). We compared early (Days

1 and 3) and late (Day 7 No AA) time points for untreated cells, and for the late time point, also cells treated with ascorbic acid at day 4 to induce myelination (Day 7AA).

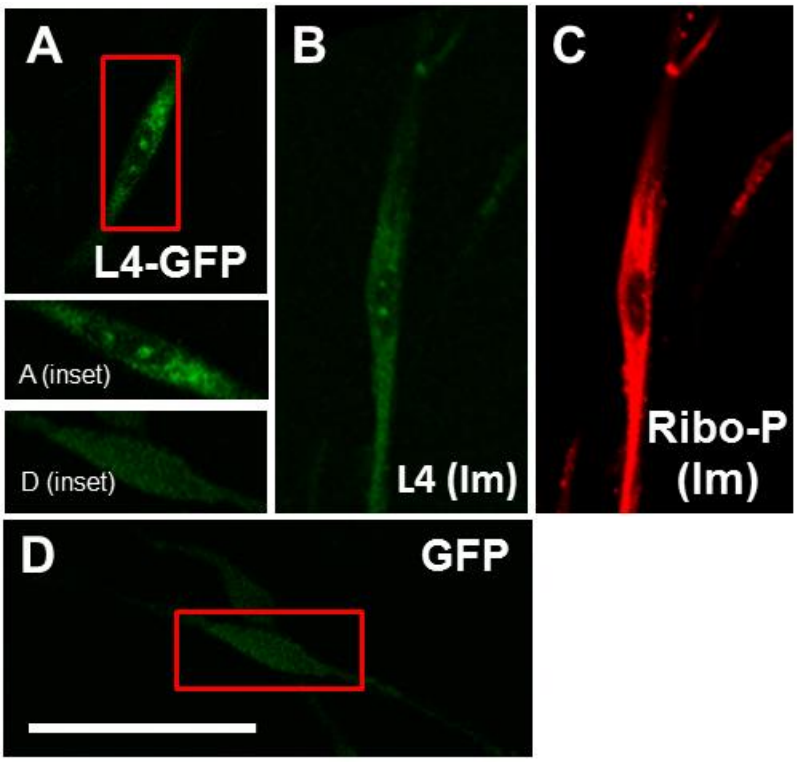

Figure 3-2: Transfection and ribosomal labeling

(A) Transfected Schwann cell expressing L4-GFP (magnified in inset); (B) Schwann cell immunostained with anti-L4; (C) Schwann cell immunostained with anti-Ribo-P shows strong extra-nuclear co-localization with L4 expression; (D) Transfected Schwann cell expressing GFP (magnified in inset) shows continuous low-level expression throughout cell, including the nuclear compartment, and differs from L4-GFP labeling pattern; Scale bar: 50 µm

The ratio of cell body fluorescence to projection fluorescence was used to determine any difference in bulk localization of ribosomes. This ratio was calculated for sub-saturation fluorescence, and was independent of any cell to cell differences in fluorescence expression. The ratios at each time point were consistent, falling between 0.406 and 0.429 ($p = 0.486$; One-way ANOVA, Figure 3-3A), suggesting no net increase or decrease in projection expression levels among all experimental groups.

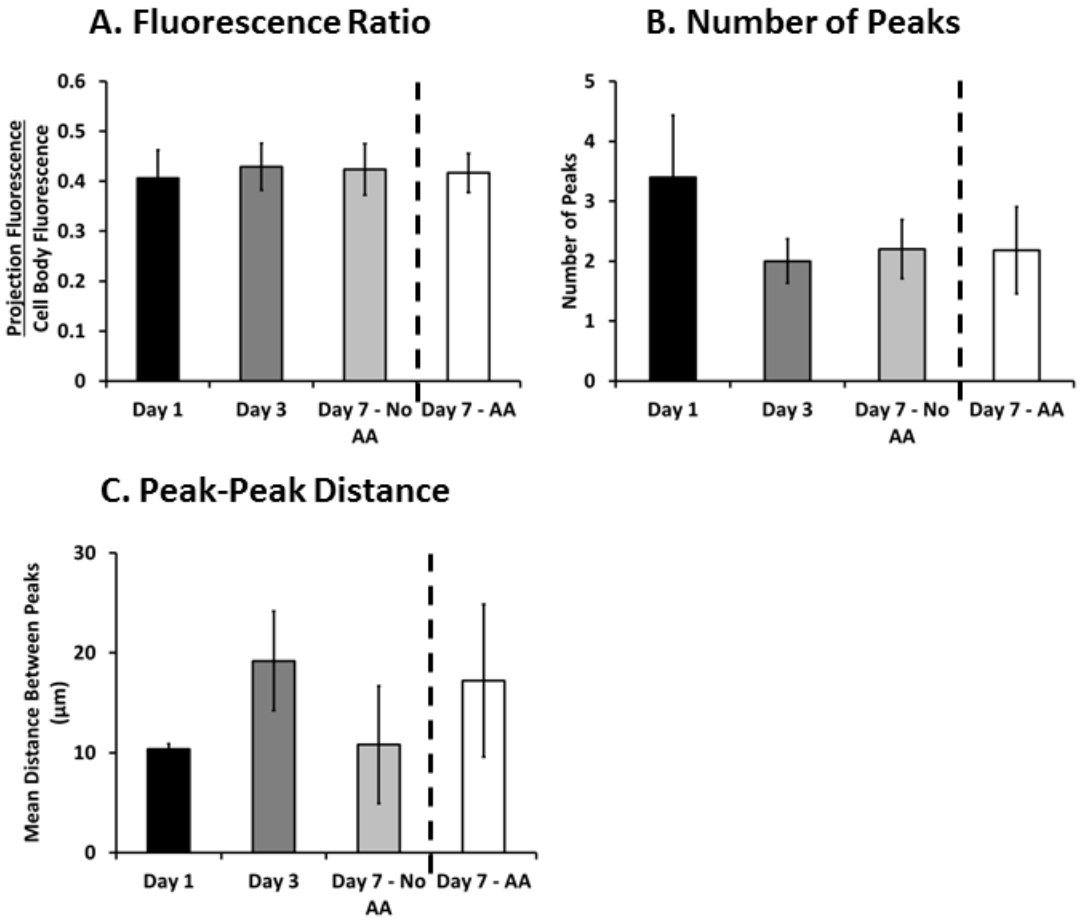

Figure 3-3: Projection ribosomal distributions

Ribosomal expression in the projections of Schwann cells remained relatively consistent throughout the experimental proceedings according to a number of metrics: (A) The ratio of fluorescence in the projection compared to the cell body remained consistent throughout the experimental groups; (B) The number of observed ribosomal peaks (or puncta) did not vary significantly throughout the experimental groups; (C) The distance between peaks varied albeit not significantly throughout the experiment (Means ± SEM). *Statistics: 1-way ANOVA.*

Bright, stationary ribosomal patches dotting the Schwann cellular projection were consistently observed at each time point. The peaks were characterized by a minimum 3x increase in fluorescence over the average projection expression level. The number of these peaks did not change amongst the experimental groups (between 2.2. and 3.4; $p = 0.77$; One-way ANOVA, Figure 3-3B). Additionally the peak to peak distance did not

vary (p = 0.605 One-way ANOVA, Figure 3-3C). Several additional morphological and fluorescence parameters of interest, including projection length, raw fluorescence, and distances of peaks from cell bodies were also calculated (Table 3-2). These also yielded no significant differences. This evidence points to an early establishment and inherent stability of the ribosomal clusters following SC alignment with neurons, independent of time or early myelination.

	Day 1	Day 3	Day 7 - No AA	Day 7 AA	P Value (ANOVA)
Projection Length (µm)	62.33 ± 9.08	80.19±10.423	71.58±9.52	93.15±24.45	0.486
Cell Body Avg. Intensity	12.94±2.4	12.65±2.1491	13.28±1.58	13.89±1.29	0.496
Projection Avg. Intensity	4.68±0.46	4.63±0.69534	5.22±0.41	5.63±0.72	0.77
Projection/Cell Body Ratio	0.41±0.06	0.43±0.046995	0.42±0.05	0.42±0.04	0.605
Number of Peaks	3.4±1.03	2±0.36927	2.2±0.49	2.18±0.72	0.663
Avg. Distance Peak to Cell Body (µm)	24.78±6.28	35.04±10.52	30.75±12.83	41.62±17.79	0.525
Avg. Distance Peak to Peak (µm)	10.38±0.51	19.19±4.9773	10.8±5.88	17.22±7.65	0.713

Table 3-2: Projection data

Additional values from projection analysis show little variability between experimental groups, p-values based on 1-ANOVA of experimental group

Subsection 3: Cytoskeletal characteristics of ribosomal clusters in Schwann cells

Based on observations of apparently stable ribosomal clusters, we tested whether any particular cytoskeletal components were associated with local ribosomal clusters. In neurons, previous reports indicated high densities of F-actin subjacent to ribosome-enriched periaxoplamic ribosomal plaques (PARPs) [62]. We therefore tested whether a similar phenomenon also occurred in SCs, by examining co-localization of immunolabeled L4 and phalloidin-labeled F-actin. We did observe bright regions of actin along the SC projection, interspersed with dim regions, enabling analysis of co-localization with ribosomal clusters. However, L4 clusters in SC projections showed no specific co-localization or apparent proximity to F-actin in SCs alone (Manders =

0.179±0.082), in the presence of neurons without induction of myelination (Day 1; Manders = 0.341±0.288) and in the presence of neurons following induction of myelination (Day 7AA; Manders = 0.197±0.113) (Figures 3-4A-C). We also examined localization of RPL4 relative to microtubules, indicated by tubulin. However, fluorescent intensity of tubulin was consistent along axons at the imaged resolution, and thus precluded any analysis of co-localization (Figure 3-4D).

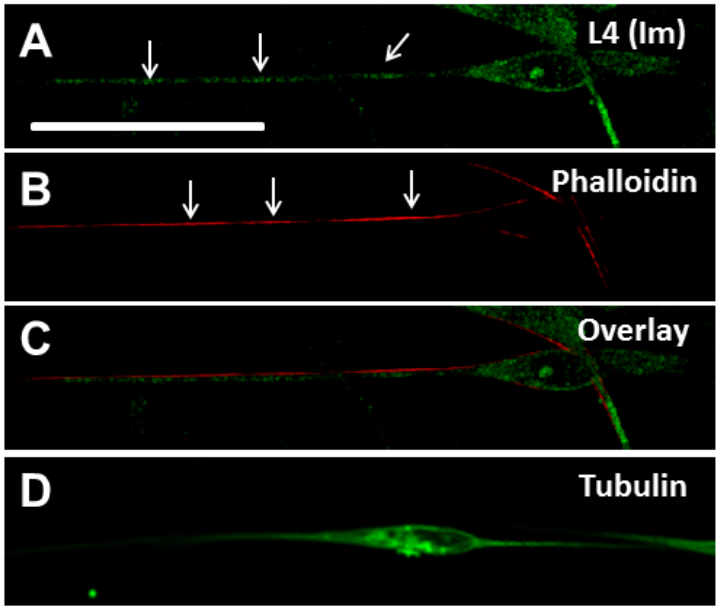

Figure 3-4: Cytoskeletal distributions in Schwann cells

(A) Schwann cell immunostained for L4 shows expression throughout the projection with specifically punctate regions (arrows) corresponding to ribosomal rich regions; (B) Phalloidin staining highlights cortical regions rich in actin (arrows) but not necessarily corresponding with ribosomal rich regions (C); (D) Tubulin immunostain revealed consistent ubiquitous expression throughout Schwann cells showing no preference for ribosomal puncta; Scale bar: 50 µm

Subsection 4: Ribosomal transport characteristics within Schwann cell projections

Though densities were apparently stable, movies of L4-GFP dynamics, captured using time-lapse fluorescence microscopy, revealed movement of less intense L4-GFP puncta between densities. Thus, to examine whether ribosomal transport contributed to

the maintenance of densities, we next quantitatively characterized the movement of L4-GFP using kymograph analysis, which allowed the observation of moving L4-GFP particles, and the characterization of puncta directionality, velocity, and duration of movement (Figure 3-5). Individual puncta were treated as single particles, independent of fluorescence intensity.

The summation of net displacement for each individual L4-GFP particle within a given movie offers a summary of directionality and extent of movement within a cell during our imaging period. Normalization of this displacement to the imaging duration yields net velocity, which enables comparison with bulk transport rates captured over a longer time frame [2,6]. There are significant differences in net velocity of ribosomes over the course of Schwann cell development ($p = 0.0038$, One-way ANOVA, Figure 3-6A). In particular, though ribosomal transport is anterograde (away from the Schwann cell body) at all time points, ribosomal transport at Day 7 increases in the absence of ascorbic acid, but is suppressed in the presence of ascorbic acid. (Mean ± SEM; No AA: 0.388±0.074; AA: 0.129±0.025, $p = 0.00189$, Tukey's HSD).

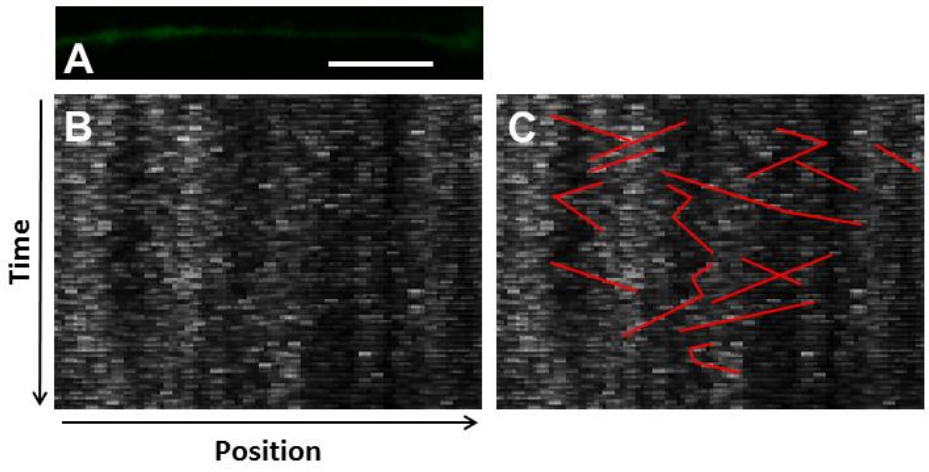

Figure 3-5: Kymograph development

(A) Schwann cell projections were cropped and traced to develop (B) a kymograph (y-axis: time, increasing downward; x-axis: position along the projection, with anterograde to the right); (C) Trajectories for puncta observed in continuous frames were traced on the kymograph to identify ribosomal movement throughout the projection, and allow for quantification of transport parameters during the course of the experiment; Scale bar: 20 μm, duration 5 minutes.

We further examined individual transport parameters to determine their contribution to net displacement/velocity in each experimental group. The comprehensive data set, including statistical analysis, is summarized in Table 3-3. For clarity, we discuss key findings below.

	Day 1	Day 3	Day 7 - No AA	Day 7 AA	P Value (ANOVA)
Net Velocity (μm/s)	0.233 ± 0.046	0.198 ± 0.02	0.338 ± 0.074	0.129 ± 0.025†	0.0038
Avg. Velocity (μm/s)	0.496 ± 0.064	0.558 ± 0.062	0.246 ± 0.039^	0.216 ± 0.09^	0.00258
Avg. Ant. Vel. (μm/s)	0.765 ± 0.055	0.802 ± 0.065	0.624 ± 0.086	0.621 ± 0.075	0.178
Avg. Ret. Vel. (μm/s)	-0.52 ± 0.234	-0.38 ± 0.122	-0.525 ± 0.148	-0.474 ± 0.08	0.848
Tot. Ant. Part	6.86 ± 0.67	5.13 ± 0.46	8.25 ± 0.8^	5.6 ± 0.58†	0.00628
Tot. Ret. Part.	1.71 ± 0.52	1.56 ± 0.26	4.63 ± 0.53*^	4.67 ± 0.61*^	0.00000615
Ant. Duration (s)	24 ± 1.64	27.34 ± 1.45	32.77 ± 3.02	25.79 ± 2.83	0.173
Ret. Duration (s)	21.3 ± 2.12	27.43 ± 3.34	35.22 ± 2.27	25.76 ± 2.61	0.0761

Table 3-3: Ribosomal transport data

Transport data values from transport analysis showing variability among velocities and particle distributions between groups, p-values passed on 1-ANOVA (Tukey HSD, $p < 0.05$ compared to *Day 1, ^Day 3, †Day 7 – No AA)

The average ribosomal velocity was also dependent upon the developmental state of the Schwann cell ($p = 0.0025$ One-way ANOVA, Figure 3-6B). Most notably, there was a significant reduction in average velocity from Day 3 (0.56 μm/s) to Day 7 (No AA: 0.25 μm/s; AA: 0.22 μm/s) irrespective of ascorbic acid treatment (Day 3 – Day 7 No AA: $p = 0.041$; Day 3 – Day 7 AA: $p = 0.004$, Tukey's HSD). While the reduction in average velocity might be expected in the case of Day 7AA, where net velocity is also reduced, this was unexpected in the case of the untreated Day 7 group, where net velocity

in fact increases. This apparent paradox indicates that other phenomena are integral in determining the net velocity.

Average particle run durations varied between 24 and 33 seconds in the anterograde direction and 21 and 35 seconds in the retrograde direction. Though there were no significant differences in particle durations in either direction (Figure 3-6C), interestingly, durations in each direction seemed to mirror one another, with the ratio of anterograde to retrograde durations confined to a narrow range of 0.93-1.12. This may indicate that variations in duration could result from a more systematic reduction in ribosomal transport regardless of directionality.

A final component of net velocity is the number and proportion of particles being transported in each direction. There were significant differences in both particle populations (Anterograde: $p = 0.006$; Retrograde: $p = 0.000006$, One-way ANOVA, Figure 3-6D). Of note in the case of the anterograde particles is the significant increase in anterograde particles from Day 3 (5.125 particles) to Day 7 (No AA: 8.25 particles) in the absence of ascorbic acid ($p = 0.005$, Tukey's HSD), but not the presence of ascorbic acid (AA: 5.6 particles; $p = 0.918$, Tukey's HSD). This increase in particle number thus may be a key factor contributing to the observed increase in net velocity.

Subsection 5: Multiple Regression

We performed multiple regression analysis on a particle by particle basis to determine the individual contributions of each component measurement (independent variables) to the resultant net velocity (dependent variable). A complete summary of regression results is found in Table 3-4. At early time points, anterograde velocity had a strong influence on net velocity (Day 1: 0.431; Day 3: 0.474), with additional contributions from directional durations (Day 1 total duration: 0.537; Day 1 retrograde

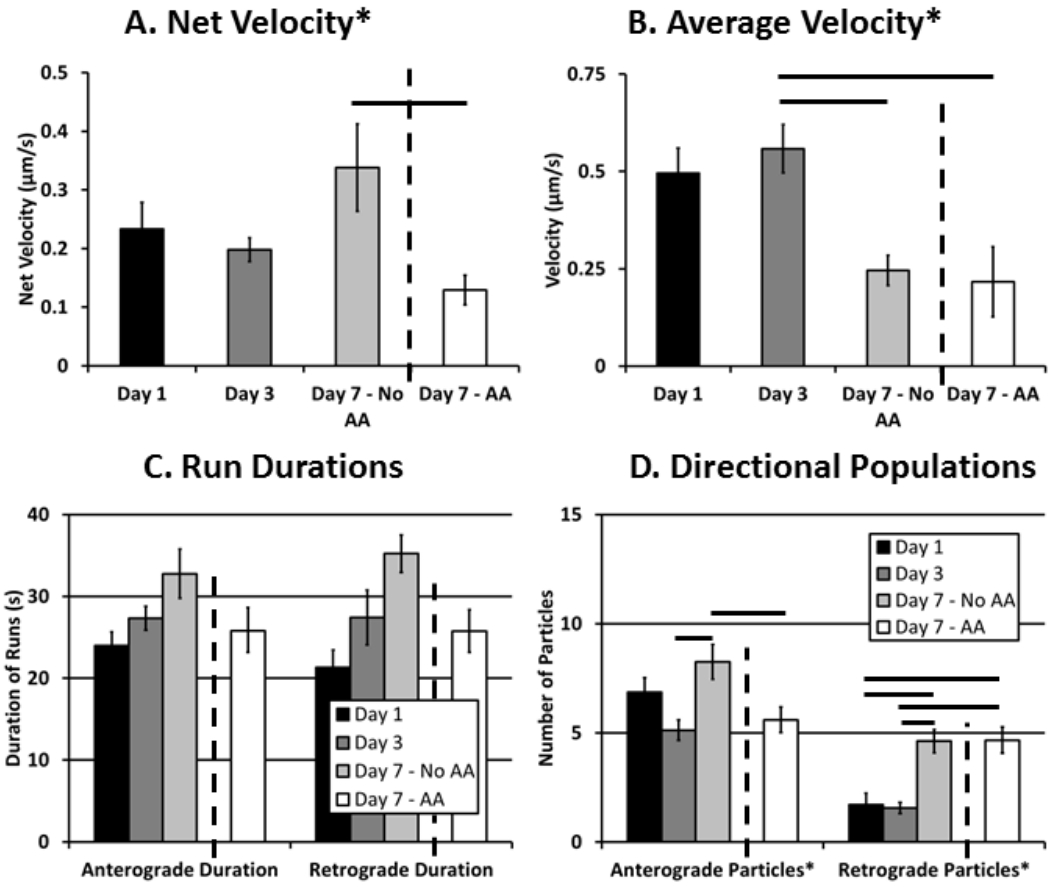

Figure 3-6: Ribosomal transport measures

Kymograph analysis provided a clear picture of the dynamics of ribosomal transport. (A) Net velocity, a measurement that provides a relative comparison of the bulk transport occurring in the cell, showed increased levels after 7 days. These levels were decreased when the cultures were treated with ascorbic acid indicating an effect of this treatment and early myelination on ribosomal transport; (B) In both day 7 treatment groups, the average velocity was decreased compared to day 3; (C) Anterograde and retrograde durations varied over the course of the experiment but failed to show any significant differences; (D) The number of anterograde particles increased after 7 days in the absence of ascorbic acid compared to both the day 3 and day 7 ascorbic acid treated groups. Additionally, there was an increase in retrograde particles in both the day 7 groups compared to the earlier time points, likely influencing the observed changes in net velocity (Means ± SEM) *Statistics: 1-way ANOVA (* $p < 0.05$); Tukey HSD (▬ $p < 0.05$).*

duration: -0.595; Day 3 anterograde duration: 0.474). At later stages, irrespective of ascorbic acid treatment, directional (anterograde) duration continued to contribute most strongly to net velocity (Day 7 AA: 0.630; Day 7 no AA: 0.925). Though the effect of anterograde velocity was sharply diminished, average velocity also contributed strongly to the model (AA: 0.525; No AA: 0.480). Thus, under the assumption that each parameter is modulated, at least partially, by a different set of biological influences, these results suggest that regulation of ribosomal transport in Schwann cells evolves temporally, but is not influenced by early myelination.

	Day 1	Day 3	Day 7 No AA	Day 7 AA
Avg. Vel.	0.021	0.022	0.480	0.525
Tot. Time	0.537	0.003	-0.352	-0.250
Avg. Ant. Vel.	0.413	0.474	-0.041	-0.041
Time Ant.	0.000	0.474	0.952	0.630
Avg Ret. Vel.	0.028	0.042	-0.060	-0.081
Time Ret.	-0.595	-0.244	0.295	-0.028

Table 3-4: Multiple regression

β-weights for multiple regression of z-scored data for independent variables regressed against the dependent variable net velocity show a shift from anterograde velocity dependence at early time points (Days 1 and 3) to anterograde time dependence at later time points (Day 7)

Subsection 6: Ribosomal Transport Model

A limitation of the narrow temporal window during which transport was assessed as well as a finer understanding of factors underlying outcomes from multiple regression analysis was an inability to examine directional transitions in particle movement. Thus, we developed a simple yet informative kinetic model, driven and validated by our experimental data, which was captured over a time frame of minutes, on net transport, which was measured over a time frame of days (Figure 3-7). The model determined a set

of rate constants that best fit experimental parameters for net velocity and the number of anterograde and retrograde particles, based on computed mean squared error. Numerical solution of the system of differential equations was stable. Model fits were extremely strong (No AA: MSE = 0.068; AA: MSE = 0.0018), and were unique within the wide range of allowed parameter values. Sensitivity analysis was also performed for each rate constant over this range of values (Supplementary Figure 3-1), and revealed that the model was most sensitive to changes in k_{+1} followed by k_{+2}.

The transition of rate constants upon addition of ascorbic acid provided information about the shift in ribosomal transport during onset of myelination. In both cases the rate of conversion from stationary to anterograde particles remained comparatively stable (k_{+1}, No AA: 0.151; AA: 0.181). This was not the case for retrograde particles, which showed a large decrease in conversion from stationary to retrograde particles (k_{+2}, No AA: 0.961; AA: 0.281), suggesting increased particle retention within projections. Further, the rate of conversion back to stationary increased dramatically with the addition of ascorbic acid for both anterograde (k_{-1}, No AA: 0.001; AA: 0.441) and retrograde particles (k_{-2}, No AA: 0.611; AA: 0.761), consistent with observed decreases in transport durations bidirectionally. Cumulatively, these results suggest that the increases in k_{-1} and k_{-2} are the likely drivers of decreased anterograde and retrograde particle number, as well as net velocity following induction of myelination.

Section 4: Discussion

The localization, dynamics, and activity of protein synthetic machinery have received increased attention in neurons [6,48,124,138,139], motivated in large part by the demands imposed by neuronal polarity and geometry. Local protein synthesis has been less extensively studied in Schwann cells, though they also extend long projections, and

thus also face similar metabolic, structural, and biochemical demands [48,52,123]. Additionally, recent evidence has suggested that Schwann cells are a source of mRNA and ribosomes for neurons recovering from injury, providing additional rationale for localizing protein synthetic machinery to SC projections [27,28].

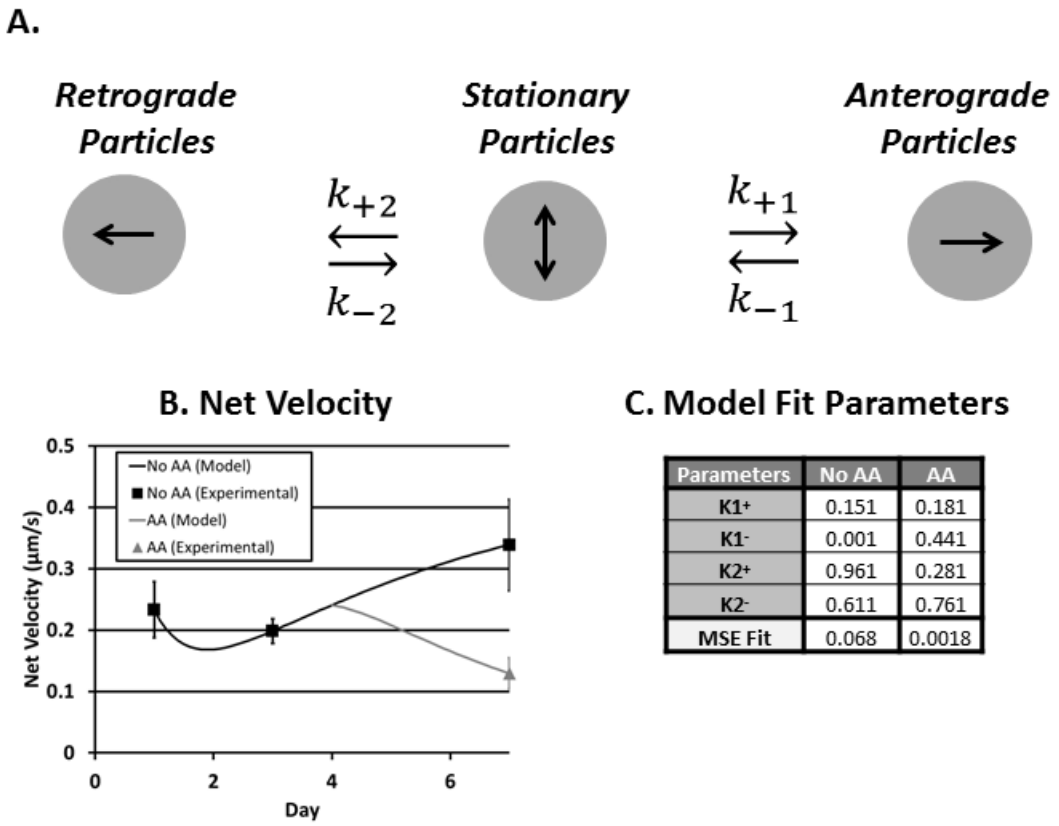

Figure 3-7: Rate kinetic model of ribosomal transport

(A) Schematic of the rate kinetic model shows possible particle states and transition rate constants between the three states; (B) Plotting of the optimized model (lines) shows strong agreement with experimental data (points); (C) Following ascorbic acid treatment the rate of conversion from anterograde to stationary (k_{-1}) increased while the rate of conversion from stationary to retrograde decreased (k_{+2}), leading to the overall reduction in net velocity.

This study used a combined experimental and theoretical approach to examine the localization and movement of ribosomes within the projections of Schwann cells at high resolution. While several important studies have documented the presence of mRNA and ribosomes in SC projections [48-52], the development and plasticity of ribosomal populations locally remain unknown. Our overall hypothesis was that local populations would be developed early during projection extension to enable projection outgrowth. However, such populations would then require supplementation, both for maintenance, given the ~40 hour half-life of ribosomes [140], as well as to sustain increased interactions with neurons, which may be stably myelinated for years [141]. Our results support our original hypothesis of anterograde transport of ribosomes developing ribosomal populations in the projections of Schwann cells during initial projection elongation. In early phases of myelination, ribosome trafficking decreases slightly as expected, in line with a shift towards a maintenance regime.

Subsection 1: Stable ribosomal populations

Localization of L4-GFP in transfected Schwann cells showed strong agreement with immunolabeled L4. Two characteristics of ribosomal expression in Schwann cell projections, seen both in transfected cells and immuno-labeled cells, are of particular note. First, similar to MBP mRNA distributions described previously,[48,50,51] there was a level of punctate ribosomal expression throughout the projection. It is possible that these ribosomes are associated with RNA granules of varying size and function, as suggested for oligodendrocytes [142]. Second, there were 2-3 stable peaks of high fluorescence intensity within each Schwann cell projection, likely pointing to locations of ribosomal clustering. These peaks were apparent upon initial projection extension on day 1 and persist throughout the seven days of observation both in the presence and absence

of ascorbic acid. This pattern too is similar to MBP mRNA densities within SC projections [48]. Future studies will reveal whether ribosomal densities synthesize proteins for stages of myelination or participate in ribosomal transfer to neurons[27,48] at structures yet to be formed. For instance, Schmidt-Lanterman incisures have been suggested as the region of ribosomal transfer following injury and occur at similarly spaced intervals (~25-30 μm) [143] as the observed ribosomal clusters [27,143]. Interestingly, while protein synthesis does not appear to extend into the Schmidt-Lanterman incisures there does seem to be significant ribosomal localization to the surface network in the region adjacent the incisures [48].

To probe a possible structural basis for observed ribosomal densities, cells were co-labeled for RPL4 and cytoskeletal components. In neurons, ribosomal clusters (periaxoplasmic ribosomal plaques) are observed within axons and cluster around regions enriched in F-actin [62]. Similarly, Schmidt-Lanterman incisures are enriched in F-actin [27,28,144]. However, co-labeling of ribosomal subunits with F-actin and tubulin failed to display any obvious co-localization with ribosomal clusters (Figure 3-4). On the other hand, it is possible that a specific set of actin- or tubulin-associated proteins rather than the filaments themselves may play a role in docking or sequestering ribosomes [145].

Subsection 2: Ribosomal movement

By Day 1 after neuronal contact, newly synthesized ribosomes containing L4-GFP were already distributed throughout Schwann cell projections. Additionally, distributions revealed minimal changes between Day 1 and Day 7, in the presence or absence of ascorbic acid. Though it was somewhat surprising that ribosomal densities were stabilized so rapidly, also of interest was the activity of more dynamic populations of directionally moving ribosomes observed using time-lapse microscopy. Kymograph

analysis, which captured ribosomal transport characteristics at each experimental time point at high resolution, enabled us to quantify and compare transport parameters in greater detail.

Individual transport parameters were integrated into an estimate of net movement (net velocity) of ribosomal populations, which served as a rough surrogate for ribosomal demand at a given stage of growth or myelination. The nucleus was the source of newly synthesized fluorescent ribosomal subunits, and as such explains the net anterograde velocities for each experimental group. Bulk rates were ~0.1–0.3 μm/sec (~8–25 mm/day), which corresponds to an intermediate rate of transport in a neuron [146]. Interestingly, at early time points, the net velocity remained quite stable, but diverged at Day 7, dependent upon ascorbic acid treatment; ascorbic acid treatment led to an overall reduction in net anterograde velocity, whereas the absence of ascorbic acid led to an increase.

The cellular processes driving reduced net velocity in the presence of ascorbic acid are mostly unexplored. Reduced ribosomal demand may simply represent a more focused diversion of translational machinery to the myelination process [33]. On the other hand, several Schwann cell activities appear to be coupled to early stages of SC-neuron contact and myelination. Structurally, neuronal contact alters the nucleation, polarity, and distribution of microtubules within myelinating Schwann cells [147]. In addition, consistent with reduced cellular extension and crawling during neuronal interactions, mobility of Schwann cell membranes and their associated cytoskeleton is reduced and adhesion is enhanced [2,148,149]. It is not inconceivable that such structural changes during early stages of myelination could influence the directionality, duration,

and overall levels of ribosomal transport. Indeed, initiation of myelination in regenerating nerves results in altered expression and distribution of several genes and proteins in Schwann cells, including neurofilaments [150], TGF-beta [151], P0 glycoprotein [152], and ion channels [153].

While there are drastic changes in net velocity with the initiation of myelination, the average anterograde and retrograde velocities did not change, suggesting that the regulation of molecular motor activity is changed, not the responsible motors themselves. While it is unclear which motors are responsible for ribosomal transport in Schwann cells, in other cellular systems the distribution of ribosomes depends on early endosome trafficking of both kinesin-3 and dynein [154,155]. Parameters that might change include binding affinities, number of available motor proteins, and initiation of transport all of which would affect net velocity but not the individual components of velocity [156]. The observed decrease in ribosomal trafficking is mostly attributable to the increased levels of retrograde moving particles. The increase in retrograde particles at Day 7, for both ascorbic acid-treated and untreated cells, are perhaps due to ribosomal recycling [157]. However, the net velocity remains positive at these times indicating that ribosomes are still required in the periphery and needed to maintain and replenish the stable ribosomal pools.

Subsection 3: Theoretical modeling of ribosomal transport

To further understand differences in transport, we used our high-resolution assessment of transport to develop and validate a simple, yet powerful, data-driven rate kinetic model of ribosomal transport. This model was particularly effective at describing the transfer of particles from one movement state (stationary, anterograde, or retrograde)

to another, providing insight into underlying transport dynamics not amenable to other types of analyses.

For example, population analysis indicated that both anterograde and retrograde populations decreased, and as a consequence, the magnitude of net velocity was also reduced. Our model enabled us to assess whether these reductions in anterograde and retrograde populations resulted from increased transition from moving to stationary particles, decreased transition from stationary to moving particles, or both. For our case, the model revealed an increased rate of conversion from anterograde to stationary (higher k_{-1}), a decreased rate of conversion from stationary to retrograde (lower k_{+2}), and a slightly higher rate of conversion from retrograde to stationary (higher k_{-2}) upon addition of ascorbic acid. These three changes thus drove the observed reduction in bidirectional movement and net velocity.

The model also raises hypotheses about different mechanisms for the decrease in both anterograde and retrograde populations. The decreased recruitment of retrograde particles may result from decreased recruitment of motor proteins and a desire to conserve established ribosomal populations within the projections. The increased conversion of anterograde particles to stationary may be resultant of myelin compaction and other restrictions on transport within the projection compartment, a systemic effect that could additionally affect retrograde transport. Such possibilities may be considered and tested in future experiments.

Section 5: Conclusions and future directions

This study provides a first quantitative look into the establishment of ribosomal populations within Schwann cells following neuronal contact and myelination, and transport changes associated with a hypothesized change in demand for a local protein

synthesis source. While others have shown that proteins are synthesized locally in Schwann cell projections and are required for myelination, we are the first to observe, quantify, and model the process dynamics during early development and myelination. The observed ribosomal transport decrease into the Schwann cell projection is likely tied to a decrease in demand for protein synthesis. However, many questions remain to be answered about how and why such dynamics occur, including which motor proteins are at work, the effect of early and late myelination on local protein synthesis, and the role, if any, early ribosomal localization may have on the proposed process of transcytosis [27]. Our initial findings open the possibility for a number of future studies that might be integral in developing translational clinical solutions for nervous system disease and injury.

Section 6: Acknowledgements

We gratefully acknowledge funding support from the Alzheimer's Association (NIRG09133270) and National Science Foundation (CBET-0932590). We also acknowledge helpful conversations with members of the Neuromuscular Bioengineering Laboratory.

Section 7: Supplemental Figure

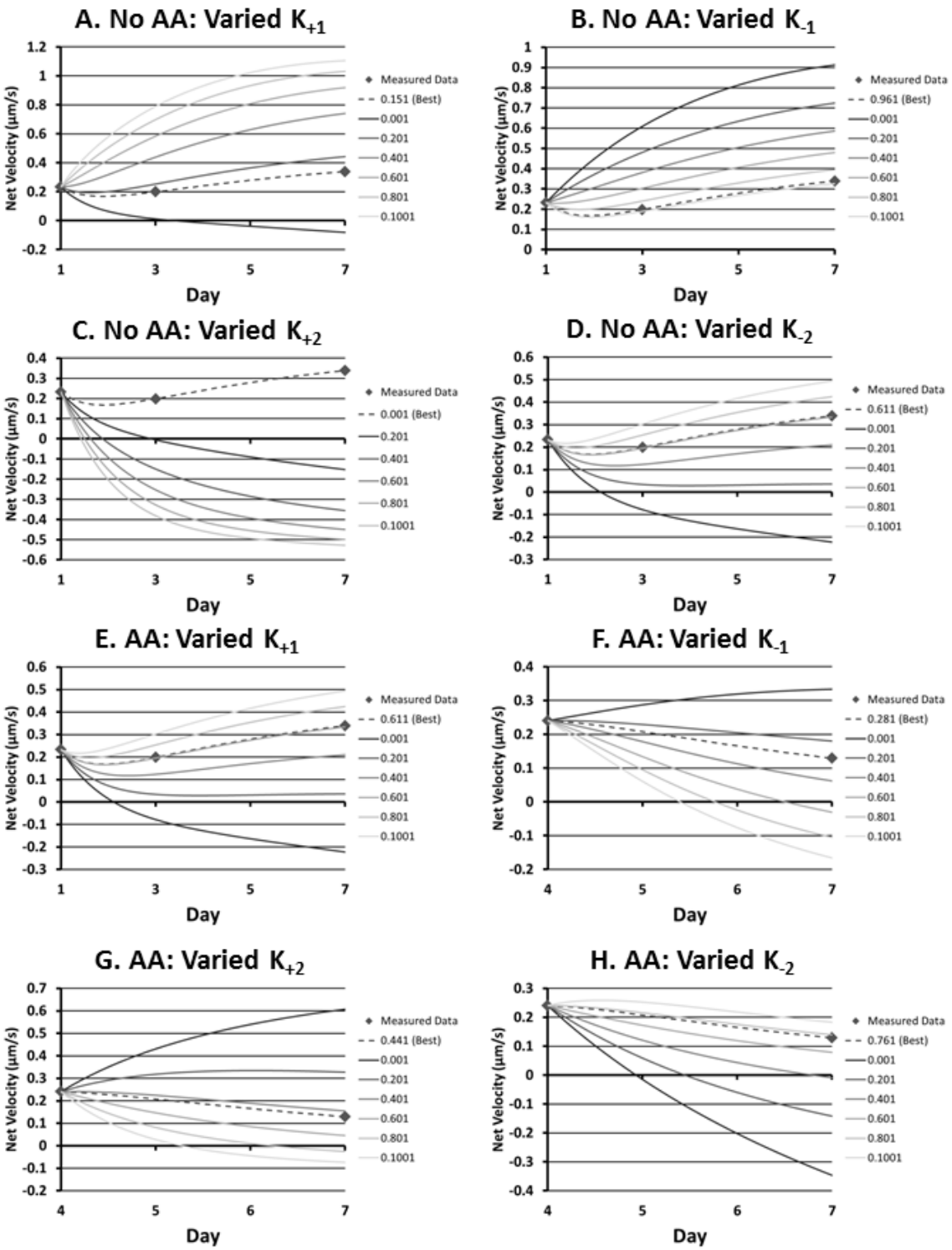

Figure 3-1 (Supplemental): Variation of model rate constants

Model traces for varying rate constants show degree of sensitivity for the unique solution. No AA groups were highly sensitive to both forward rate constants, k_{+1} (A) and k_{+2} (C), yet slightly less sensitive to variations in both reverse rate constants, k_{-1} (B) and k_{-2} (D). Similar results held for parameter variations in the AA treated model with higher sensitivity to changes in both forward rate constants, k_{+1} (E) and k_{+2} (G), and lower sensitivity to the changes in the reverse rates, k_{-1} (F) and k_{-2} (H).

Chapter 4: Nerve strain correlates with structural changes quantified by Fourier analysis [3]

Section 1: Introduction

Peripheral nerve deformation affects electrophysiological function. Excess deformation results in functional deficits and the amount of strain dictates the reversibility of deficits [55,158,159]. This concept is particularly important during repair of severed nerves or limb lengthening procedures. Surgeons rely primarily on their experience and "feel" when they determine the appropriate tension for nerve reattachment [160,161]. Though tension-free repairs are a clinically accepted standard, some studies suggest that a modest level of strain can benefit nerve repair [78] and may even enhance neuronal function and promote survival [162]. Therefore, the ability to accurately and objectively monitor physiological strain may ultimately be of clinical utility.

Originally identified in 1781 [163], one can observe the bands of Fontana, a distinct optical phenomenon that results from undulations in axonal tracts and their surrounding connective tissue [58,164-166]. The periodicity of bands of Fontana varies with strain; they ultimately disappear at ~14% strain (8% beyond resting strain) in the sciatic nerve of rats [164], which correlates with functional loss [55,158,159]. Thus, bands of Fontana may provide a sensitive structural predictor of nerve function.

We report an automated Fourier-based image processing method to quantify periodicity of bands of Fontana in rat sciatic nerves from digital images. Positive correlation between periodicities and applied strain was observed. Application of this method to immuno-labeled longitudinal sections of nerves at varying strain provide a

structural correlate for changes in the bands of Fontana, and demonstrate the versatility of the analytical method.

Section 2: Methods

Subsection 1: Animals and tissue collection

Sciatic nerves were excised from 8 3-month old male Sprague-Dawley rats (Charles River Labs). Procedures were approved by the UCSD Institutional Animal Care and Use Committee. Six nerves from 3 animals were examined for *in situ* and *severed* studies. Following sacrifice, sciatic nerves were exposed, and *in situ* images of banding patterns at relaxed knee and ankle joint angles were collected (85-95° each). Nerves were then transected just proximal to the trifurcation, and images were obtained of the severed nerve. Nerves were then excised 15 mm proximal to the site of transection. Three nerves, 1 from each animal, were pinned to cork board and imaged at 0% (prior to stretch), 10%, and 20% strain.

Subsection 2: Imaging

Bands of Fontana were imaged using a D5100 digital camera with a DX SWM VR Aspherical ∞ - 0.28m lens (Nikon). Histological sections were imaged with a Leica SP5 confocal imaging system and a 10x objective (resolution of 3.027 μm/pix). An argon laser enabled excitation at 488nm. Emission was captured between 500-550 nm. Vertical stacks of ~24 images were acquired for each sample, with section thickness of 0.5-0.7 μm.

Subsection 3: Histology

Nine separately excised nerves from 6 specimens were pinned at specified strains, flash-frozen in liquid nitrogen-cooled 2-methylbutane for 2 minutes, and stored at

-80°C. Excised nerves were embedded in OCT, sectioned longitudinally and placed on Superfrost® Plus slides (Fisher 12-550-15).

Subsection 4: Immunostaining

Triplicate washes were performed in PBS. Samples were permeabilized with 0.2% Triton-X 100 in PBS for 5 minutes, washed, blocked with 10% FBS and 3% BSA in PBS for 30 minutes at room temperature, washed, and incubated with a monoclonal primary antibody targeting myelin-basic protein (MBP) (MAB382, Millipore) for 1.5 hours at room temperature. Samples were then washed and incubated for 2 hours in Alexa Fluor 488-goat anti-mouse secondary antibody (Invitrogen A-11001). Primary and secondary antibodies were diluted in blocking solution (1:200).

Subsection 5: Signal processing

Images were cropped and contrast enhanced to visualize bands in ImageJ (NIH) (Figure 4-1A). Cropped images were analyzed using a custom Matlab (Mathworks Inc.) program. Images were treated as two-dimensional matrices, with 8-bit pixels possessing an intensity normalized between 0 and 1. For each horizontal image row, using logic similar to subtracting DC-offset, a smoothed intensity trace ["smooth" function, Lowess method, span of (row length – 1)] was subtracted from the raw intensity profile to minimize zero-frequency artifacts during subsequent analysis (Figures 4-1B and 4-1C). A fast Fourier transform of this trace provided a peak frequency corresponding to the frequency (reciprocal of peak-to-peak distance) of bands of Fontana (Figure 4-1D) or axonal undulations. Residual zero-frequency peaks were ignored. The average frequency was computed for each sample by averaging individual row frequencies.

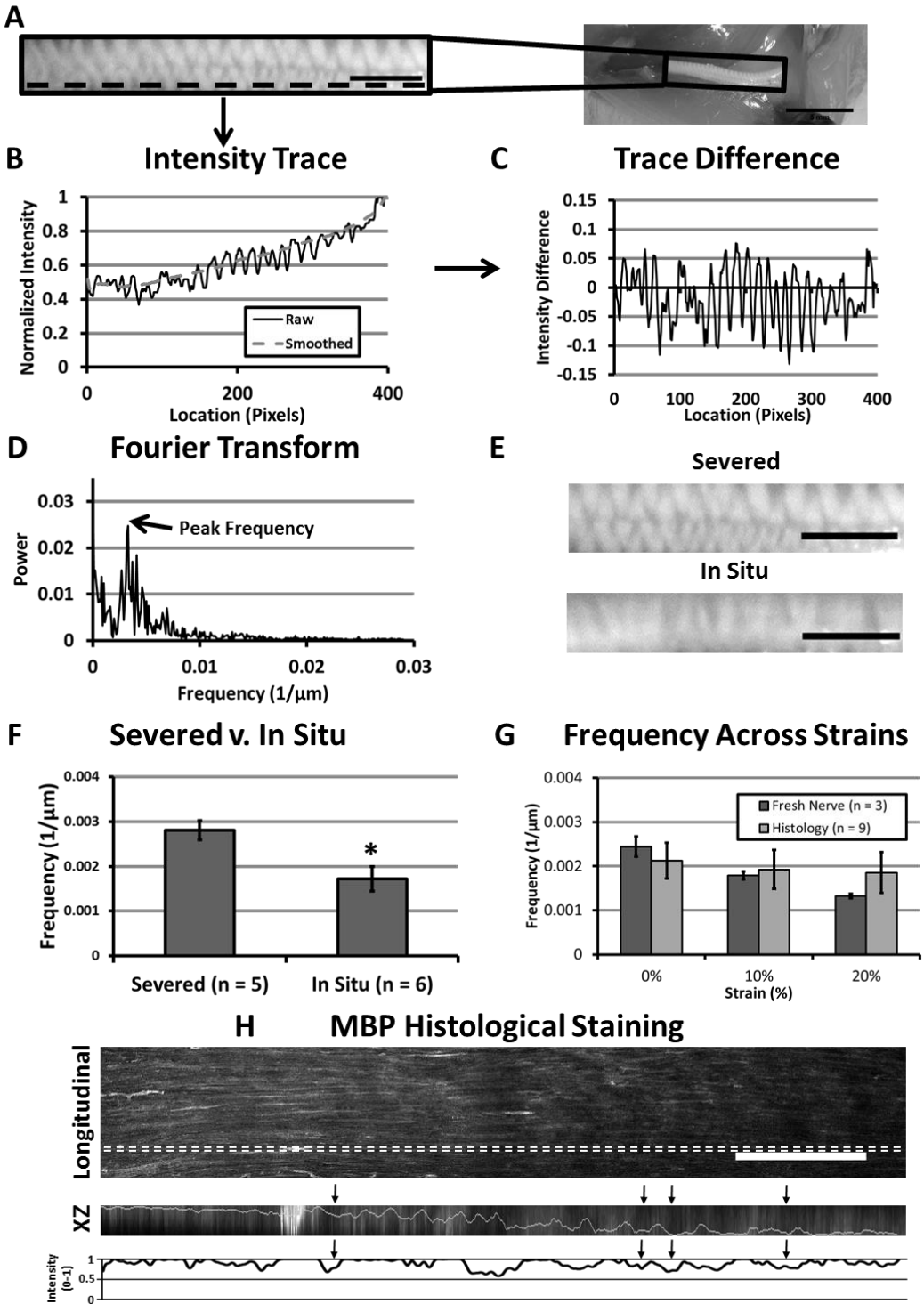
A
B
Intensity Trace
Normalized Intensity
Raw
Smoothed
Location (Pixels)
C
Trace Difference
Intensity Difference
Location (Pixels)
D
Fourier Transform
Peak Frequency
Power
Frequency (1/µm)
E
Severed
In Situ
F
Severed v. In Situ
Frequency (1/µm)
Severed (n = 5)
In Situ (n = 6)
G
Frequency Across Strains
Fresh Nerve (n = 3)
Histology (n = 9)
Strain (%)
H
MBP Histological Staining
Longitudinal
XZ
Intensity (0-1)

Figure 4-1: Correlation of band frequency with nerve strain

A: Sample of cropped section used to identify bands of Fontana frequency; bar = 1 mm B: Plot of sample trace and corresponding smoothed function from custom MATLAB program C: Plot of sample trace offset by smoothed trace, providing a waveform that reflects around 0 D: Sample Fourier power spectrum used to identify peak frequency of each trace E: Samples of bands of Fontana imaged in situ and following transection; bars = 1 mm F: Average frequencies of bands of Fontana between severed and in situ samples (Mean ± SEM, *p < 0.05) G: Frequency changes with varying strain in histological cross-sections and bands of Fontana in fresh nerve (Mean ± SEM) H: Longitudinal nerve slice stained against MBP and projected into XZ plane between dotted lines. Solid line indicates smoothed fit of the maximal intensity location shows axonal undulations in the Z-direction; bar = 500 μm. Intensity plot of maximal intensities along projection reveals regional agreement between decreased intensity and axonal undulations designated by arrows.

Subsection 6: Statistics

Means were compared using *t*-test or ANOVA with $\alpha = 0.05$ for hypothesis testing. Strain and frequency correlations were tested using linear regression.

Section 3: Results

In situ, bands of Fontana were periodic but appeared slightly disjointed and blurred. Bands appeared sharper and narrower upon severing the nerve (Figure 4-1E), which resulted in a 10% recoil of the nerve and a corresponding 60% increase in band frequency. (Figure 4-1F; $P < 0.05$, unpaired *t*-test, n = 5 or 6).

To correlate nerve strain with band frequency, we stretched excised nerves by 10% and 20%. Comparison of the means revealed a significant effect of strain on frequency ($P < 0.05$, 1-way ANOVA, n = 3), and a strong linear relationship between nerve strain and band frequency (Figure 4-1G; $-0.0056\ \mu m^{-1} \cdot \%^{-1}$, $r^2 = 0.829$; $P < 0.05$, regression, n = 9). To investigate a structural basis for bands of Fontana, Fourier analysis was applied to longitudinal sections immuno-labeled for MBP. Alternating light and dark regions indicated waviness in the perpendicular plane, as confirmed by three-dimensional

reconstruction (Figure 4-1H). Higher variability compared to intact nerves, possibly due to varying planes of undulation, resulted in an underpowered statistical comparison. Nevertheless, a trend similar to that in fresh nerve was observed at low strains. Increased frequencies at large strain may result from observed structural damage incurred at super-physiological strains. Manual measurement of frequencies in both whole nerve and sections confirmed the accuracy of computed frequencies (e.g., Figures 4-1E and 4-1H).

Section 4: Conclusions

Using Fourier analysis, we successfully correlated increases in nerve strain with decreased frequencies of bands of Fontana and axonal undulations. These relationships are consistent with the concept that axons first unravel within deformed nerves to minimize their exposure to tensile loads. Differences in the magnitude of bands of Fontana and axonal undulation frequencies may indicate that additional structures contribute to bands of Fontana, such as superposed undulations of perineurial structures ensheathing fascicles [165]. Crimped epineurial collagen has been posited previously to contribute to bands of Fontana. This is unlikely, as crimp frequency is higher than axonal undulations [167]. A comprehensive three-dimensional study of nerve architecture will further clarify the relationship between structural elements and bands of Fontana.

Methodologically, similar Fourier-based techniques have been used to identify periodic patterns in other tissues, including tendon and skeletal muscle [168-170]. Our approach is both accurate and objective and thus has considerable value towards understanding structure-function relationships in the nervous system and guiding the preservation or enhancement of neural function.

Section 5: Acknowledgements

This research was supported by grant W81XWH1010773 from the U.S. Army Medical Research and Materiel Command and the State of Maryland Stem Cell Research Fund. We also acknowledge helpful discussions with members of the Neuromuscular Bioengineering Laboratory.

Section 6: Abbreviations

PBS: phosphate buffered saline, FBS: fetal bovine serum; BSA: bovine serum albumin; MBP: myelin basic protein; ANOVA: analysis of variance; SEM: standard error of the mean

Chapter 5: Strain induced mTOR signaling leads to enhanced protein synthesis in Peripheral nerves

Section 1: Introduction

Excessive tensile strain (stretch) or high strain rates can damage peripheral nerves and their component neurons, often irreversibly [55,56]. On the other hand, neurons also possess a remarkable ability to accommodate and respond to moderate levels of tensile loading. Nerves are stretched during rapid phases of organism growth [171], bear acute strains up to 25% during joint movement [54], and also adapt to more persistent strain, such as that occurring during limb lengthening [71]. Consistent with the latter, *in vitro* evidence suggests that strained axons can increase both their growth capacity and rate of elongation [75-77].

These concepts have recently been translated into strain-based neuroregenerative strategies, with varied success [21,78,172]. Limiting our ability to optimize strain-driven regenerative strategies, though, is a poor understanding of biological mechanisms underlying neuronal response to strain. Axons gain volume rather than simply thinning while under strain [173], and thus require an increase of cellular material to support this expansion. Such a response is analogous to that occurring during axonal outgrowth during development or following injury, in which the production of many proteins, including those associated with the cytoskeleton, is increased [66,174,175].

Local protein synthesis provides an efficient way to mobilize structural elements required for increased neuronal volume. To this end, a number of mRNAs encoding cytoskeletal proteins are present locally within the axonal compartment, including β-actin, tubulin, and neurofilament heavy subunit (NF-H) [66-68]. These transcripts appear

to be translated under conditions of stress. For example, severed axons require axonal protein synthesis to regenerate [69,81,82], in an mTOR dependent manner. Consistent with these findings, suppression of PTEN, an inhibitor of mTOR, enhances axonal elongation [70]. A role for mTOR in regulating strain-associated axonal expansion has not yet been tested. However, several other tissue systems, including skeletal and cardiac muscle, respond to strain by activating mTOR-dependent protein synthetic pathways , which are initiated by FAK phosphorylation [79,80].

Considering the importance of mTOR in axonal extension as well as its role in responding to strain in non-neuronal cells, we hypothesized that applied peripheral nerve strain activates mTOR-mediated signaling pathways within axons, resulting in increased local synthesis of cytoskeletal proteins within the nerve. Our data reveal that mTOR-associated pathways are activated and cytoskeletal proteins increase their expression upon rat sciatic nerve strain. However, mTOR differentially regulates the synthesis of individual cytoskeletal proteins.

Section 2: Methods

Subsection 1: Animal care

Animal usage was in accordance with protocols approved by the UCSD Institutional Animal Care and Use Committee (IACUC). For *in vivo* experiments, adult male rats between the ages of 10 – 13 weeks were utilized. For *in vitro* experiments, pregnant female rats were euthanized to obtain embryos for primary DRG culture. All adult animals were sacrificed by asphyxiation with CO_2 followed by confirmation via removal of major organs. Embryonic rats were sacrificed by decapitation.

Subsection 2: Animal surgery and nerve strain

Anesthesia was induced with 5% isoflurane, and maintained for the duration of the experiments at 1.5– 3% isoflurane. The strained experimental limb was randomly assigned and contralateral limb was used for paired comparison. Surgery consisted of sciatic nerve exposure through separation of the fascial band of the biceps femoris. The nerve was then freed from the tissue bed by removing superficial fascia. A custom wedge (Figure 5-1B) was placed beneath the sciatic nerve, creating strain by elevating the nerve from the tissue bed (cf. bow-stringing in single axon studies [176]). This method avoided potential damage associated with grasping or clamping strategies for nerve lengthening. It also avoided regional variability in strain incurred by manipulating joint positions. Nerves were strained for a period of either 15 minutes (acute signaling) or 6 hours (protein synthesis) depending upon the desired outcome measurement. The strained section of the sciatic nerve was excised and flash frozen in liquid nitrogen-cooled isopentane, and stored at –80°C for future processing. Sham surgeries were performed on contralateral limbs, exposing and freeing the sciatic nerve without wedge insertion.

Subsection 3: Rapamycin treatment

To inhibit mTOR activity, rats were injected with 5 mg/kg rapamycin (J62473; Alfa Aesar) in a solution consisting of 1 mg/ml rapamycin, 5% v/v ethanol, 4% v/v Tween 80, 4% v/v polyethylene glycol in sterile water (as described in [177]). Carrier control rats were injected with the same solution without rapamycin.

Subsection 4: Tissue homogenization and sample preparation

Individual nerves were homogenized in 150 µl of homogenization buffer consisting of 20 mM Tris-HCL, 150 mM NaCL, 1% v/v NP-40, 20 mM NaF, 2 mM EDTA, 2.5 mM NaPP, 20 mM β-glycerophosphate and 10% glycerol [178,179].

Homogenization buffer was supplemented with cOmplete (04693116001; Roche) and phosSTOP (04906845001; Roche) to inhibit protein degradation and dephosphorylation. Whole protein levels were quantified by BCA analysis. Samples were diluted to 1 µg /µl total protein with additional homogenization buffer, and supplemented with Laemmli sample buffer at 3:1 (sample:LSB). Samples were boiled at 100°C for 10 minutes to denature proteins prior to storage at –80°C.

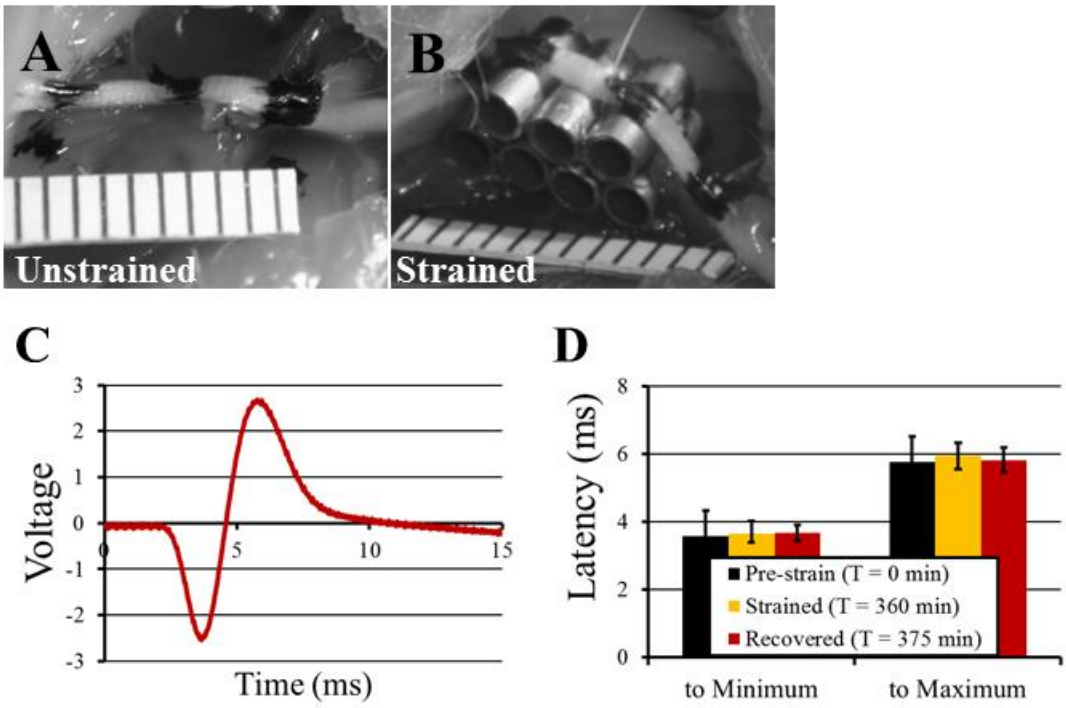

Figure 5-1: Experimental set-up and electrophysiology

(A) Sciatic nerves were marked and imaged following exposure for baseline reference. (B) Insertion of custom wedge strained the nerve locally while minimizing damage. Markings were used to ensure consistent strain of the nerves. (C) Sample EMG recording from the TA displays characteristic depolarization and hyperpolarization following sciatic nerve stimulation. (D) Latency measurements made from stimulation to minimum and maximums of the recording trace revealed no difference following stretch compared to pre-stretch (paired t-test); *Mean ± SEM*

Subsection 5: Western blotting

Samples were removed from –80°C and heated at 60°C for 6 minutes. Samples were loaded into precast 3-8% Tris-acetate gels with 20 μg total protein per well. Gels were run in Tricene running buffer for 95 minutes with a constant voltage of 110 Volts. Following electrophoresis, proteins were transferred from the gel to a nitrocellulose membrane. Transfer occurred at 4°C and 200 mA for 2 hours in transfer buffer (18 g glycin, 3.8 g Tris base in 1 L H_2O supplemented with 200 ml of methanol). The membrane was then blocked in 5% milk in TBS-T (2.43 g Tris base, 8 g NaCl, 0.5 μl in 1L H_2O; pH = 7.5) for 1 hour. Membrane was washed 4x (10 min, 10 min, 5 min, 5 min) after blocking and then placed in primary antibody in TBS-T overnight at 4°C on a rocker. Primary antibody was removed and membrane was again washed 4x (10 min, 10 min, 5 min, 5 min) and secondary was added (1:1000 in TBS-T) for 1 hour. Secondary antibody was removed and the membrane was again washed 4x (10 min, 10 min, 5 min, 5 min). Proteins were visualized using ECL. Blots were stripped and reprobed for additional proteins. Image capture and quantification of western blots was performed using ImageLab software. Phosphorylated levels of proteins were normalized to the total levels of the particular protein. To avoid confounding effects of anticipated fluctuations in levels of cytoskeletal proteins, which are often used for normalization, we normalized total protein levels to those of GAPDH (Ning 2010). Antibodies used were: $pmTOR^{Ser2448}$ (5536P; Cell Signaling), total mTOR (2983P; Cell Signaling), $pFAK^{Y397}$ (44624G; Life Technologies), total FAK (05537; Millipore), $pS6^{Ser240/244}$ (2215S; Cell Signaling), total S6 (2317S; Cell Signaling), β-actin (A5060; Sigma-Aldrich), tubulin (T9026; Sigma-

Aldrich), SMI-31 (ab24573; abcam), GAPDH, p-p38 MAPK$^{T180/Y182}$ (9211S; Cell Signaling), total p38 MAPK (9212; Cell Signaling).

Subsection 6: Electrophysiology

Methods were similar to [180], excepting the use of the TA rather than interosseus muscles to record muscle response to nerve stimulation. Briefly, following sciatic nerve exposure, a miniature bipolar nerve hook electrode (501650; Harvard Apparatus) was positioned proximal to the strained region. The tibialis anterior was exposed and needle recording electrodes (Grass F-E2) were positioned adjacent to the endplate zone [181]. A ground needle electrode was placed in the contralateral limb. Single pulses of 7 V were used to excite the nerve and elicit a response. At each time point, five consecutive recordings were made to ensure consistency of stimulation and recording, and averaged together to determine the latency between stimulus and recording. Unstrained measurements were made with the nerve in a neutral configuration, with knee and ankle neutral. As acute strain could not be measured with the wedge in place, for these measurements, strain was applied by elevation of the nerve cuff to match the degree of strain applied via wedge implantation. Wedges were used to impose strain during the 360 minute period. Measurements were made at the following time points in the following order: unstrained T=0 min, strained T=0 min, strained T = 15 min, unstrained 15 min, strained 360 min, unstrained 360 min, unstrained 375 min (an additional 15 min rest period following wedge removal).

Subsection 7: Statistics

Paired t-tests were used to compare contralateral strained versus unstrained nerves (Excel; Microsoft). We used R to run two-way ANOVAs to compare the effects of both

rapamycin treatment and strain for signaling characterization. Experimental groups of 8 rats were used for all experiments except where otherwise noted.

Section 3: Results

Subsection 1: Validation of strategy for in vivo nerve strain

We developed methodology to strain rat sciatic nerves without incurring damage associated with clamping or grasping the nerve. Insertion of a custom-made isosceles trapezoidal wedge into the underlying nerve bed imparted a consistent tensile strain on the top edge of the wedge by bow-stringing the nerve. Rounded corners of the wedge minimized any nerve tethering, and allowed a gradual reduction of strain along regions of the nerve descending from the wedge. Nerves were subjected to calculated strains of 11.24 ± 0.95% (Mean ± SEM, n = 5), within the upper limits of physiological strains [54].

To confirm that nerves did not experience injurious compression or damage over the course of the experiment, conduction latencies to the TA were measured, following stimulation of the sciatic nerve proximal to the site of strain (Figure 5-1C). Comparison of pre-stretch latencies with those following 360 minutes showed no significant differences in both the latencies to primary and secondary peaks (Figure 5-1D, Table 5-1). Additionally, while signal amplitude was variable from time point to time point (though not for repeated measurements within a time point), at no point did we see a significant reduction in amplitude to peak amplitude between pre-stretch (4.26 ± 2.22 V), 5 hours stretch (7.09 ± 1.40 V), and recovered (6.49 ± 1.38 V). The apparent increase in amplitude is likely a result of increased recruitment of fibers by the electrode due to flattening of the nerve following stretch.

	Latency to Min (ms)	Latency to Max (ms)
Pre-strain (T = 0 min)	3.59±0.73	5.76±0.75
Strained (T = 360 min)	3.64±0.24	5.94±0.38
Recovered (T = 375 min)	3.68±0.23	5.82±0.37

Table 5-1: ***TA EMG latencies***

Latency values from TA EMG recordings following sciatic nerve stimulation (Mean ± SEM, n = 3). No significant difference, paired t-test to pre-stretch (all $p > 0.05$)

Subsection 2: mTOR pathway activation and cytoskeletal protein expression following nerve strain

To determine if mTOR-associated translational pathways were activated in strained nerves, away from neuronal cell bodies, we first used Western blot analysis to examine the response of FAK and mTOR activation levels following 15 minutes of applied strain. Consistent with other model systems, a trend towards rapid mTOR activation with strain was observed by a 40% increase in the p-mTOR/mTOR ratio for strained nerves compared to unstrained ($p = 0.070$, paired t-test; Figures 5-2A-B). Interestingly, however, FAK signaling was unresponsive at this early time point suggesting an alternate mode of initiation (Figures 5-2A-B). Following 6 hours of applied strain, mTOR signaling persisted, with an increase of 37% over unstrained nerves ($p = 0.002$, paired t-test; Figures 5-2C-D). Consistent with this activity, we also observed a 28% increase in activation of S6, a translational regulator downstream of mTOR, at 6 hours, in strained compared to unstrained nerves ($p = 0.014$, paired t-test; Figures 5-2C-D).

We then tested whether strain induced a correlative increase in cytoskeletal expression. We focused on expression of β-actin, neurofilament heavy subunit (NFH) and tubulin, which have been hypothesized to be synthesized locally in neurons [66-68].

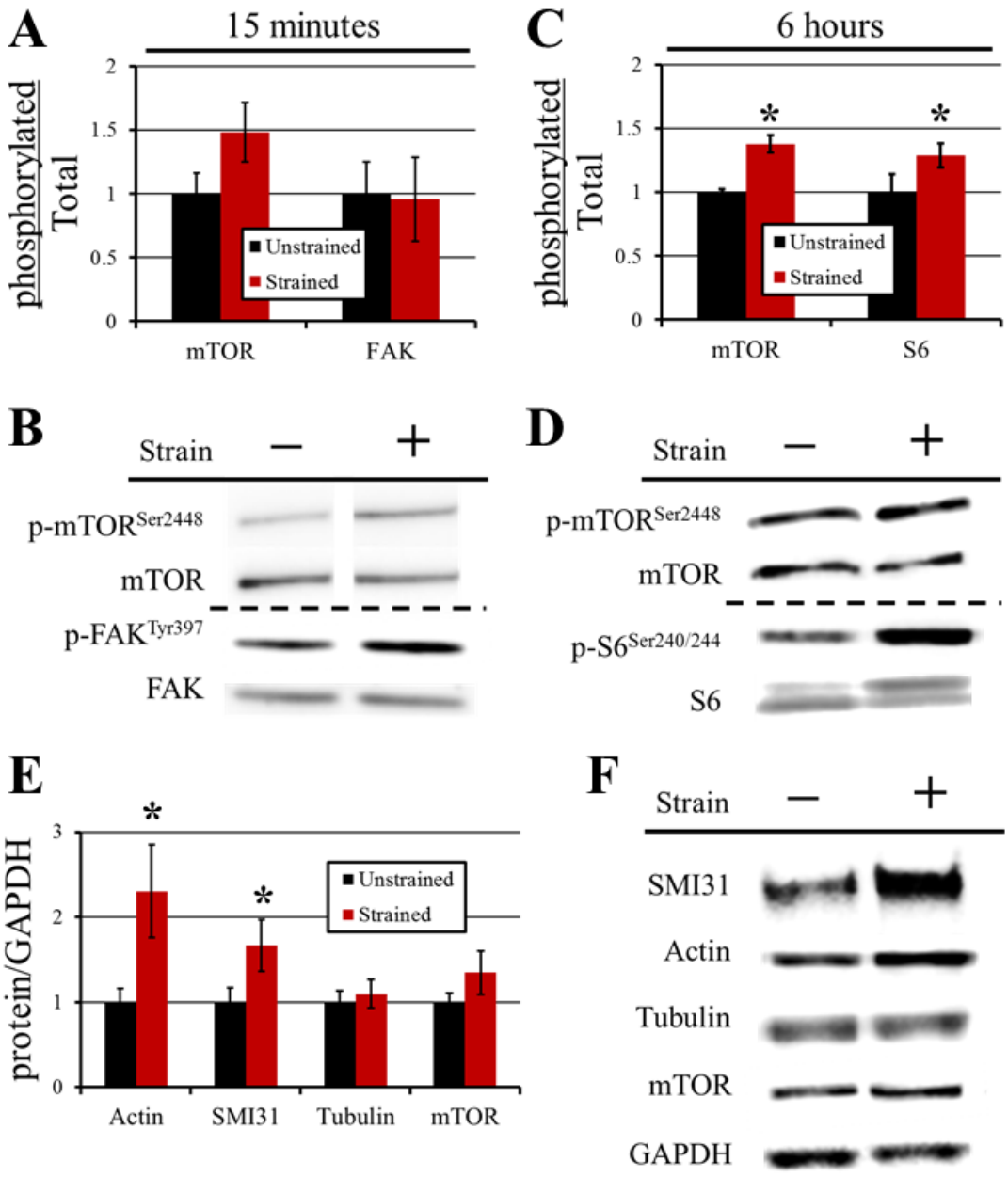

Figure 5-2 Strain induced signaling and protein expression

(A) Application of strain for 15 minutes revealed a trend towards increased mTOR phosphorylation with constant levels of FAK signaling (n = 4) as revealed by western blotting (B). (C) Following 6 hours of strain application, a significant increase was observed in both mTOR and S6 phosphorylation levels following the application of strain as revealed by western blotting (D). (E) β-actin and SMI31 levels significantly increased following application of strain while tubulin and total mTOR levels remained constant (*$p < 0.05$, paired t-test); *Mean ± SEM; all graphs normalized to unstrained levels*

Cytoskeletal protein levels were normalized to GAPDH, a non-cytoskeletal marker. Following 6 hours of strain, relative to unstrained contralateral nerves, we observed increases in both β-actin (130%; p = 0.035, paired t-test; Figures 5-2E-F) and SMI-31 (67%; p = 0.008, paired t-test; Figures 5-2E-F). Tubulin, on the other hand, failed to show any change in levels following strain application (p= 0.446, paired t-test; Figures 5-2E-F).

Subsection 3: Rapamycin differentially regulates strain induced cytoskeletal protein synthesis

Given the correlation between increased mTOR and S6 activation and increases in cytoskeletal protein levels following 6 hours of strain, we next tested the hypothesis that inhibition of mTOR complex 1 (the mTOR complex associated with activation of S6) via systemic rapamycin administration would suppress these increases. Rapamycin was administered 1 hour prior to the 6 hour period of strain application. To confirm rapamycin activity we examined the level of mTOR activation following strain application by western blot. Both the contralateral, unstrained nerve (50% reduction; Figures 5-3A-B) and strained nerves (30% reduction; Figures 5-3A-B) revealed a significant reduction in mTOR activation. Two-way ANOVA analysis for strain and rapamycin revealed a significant rapamycin dependent decrease in mTOR activation ($p = 6.86 \times 10^{-13}$). Additionally, a strain effect ($p = 1.18 \times 10^{-6}$) and slight interaction effect (p = 0.074) were observed, suggesting that mTOR activation may be disproportionately suppressed in strained nerves. Consistent with these data, similar analysis of activated S6 levels again revealed suppression of activated levels in both the contralateral, unstrained

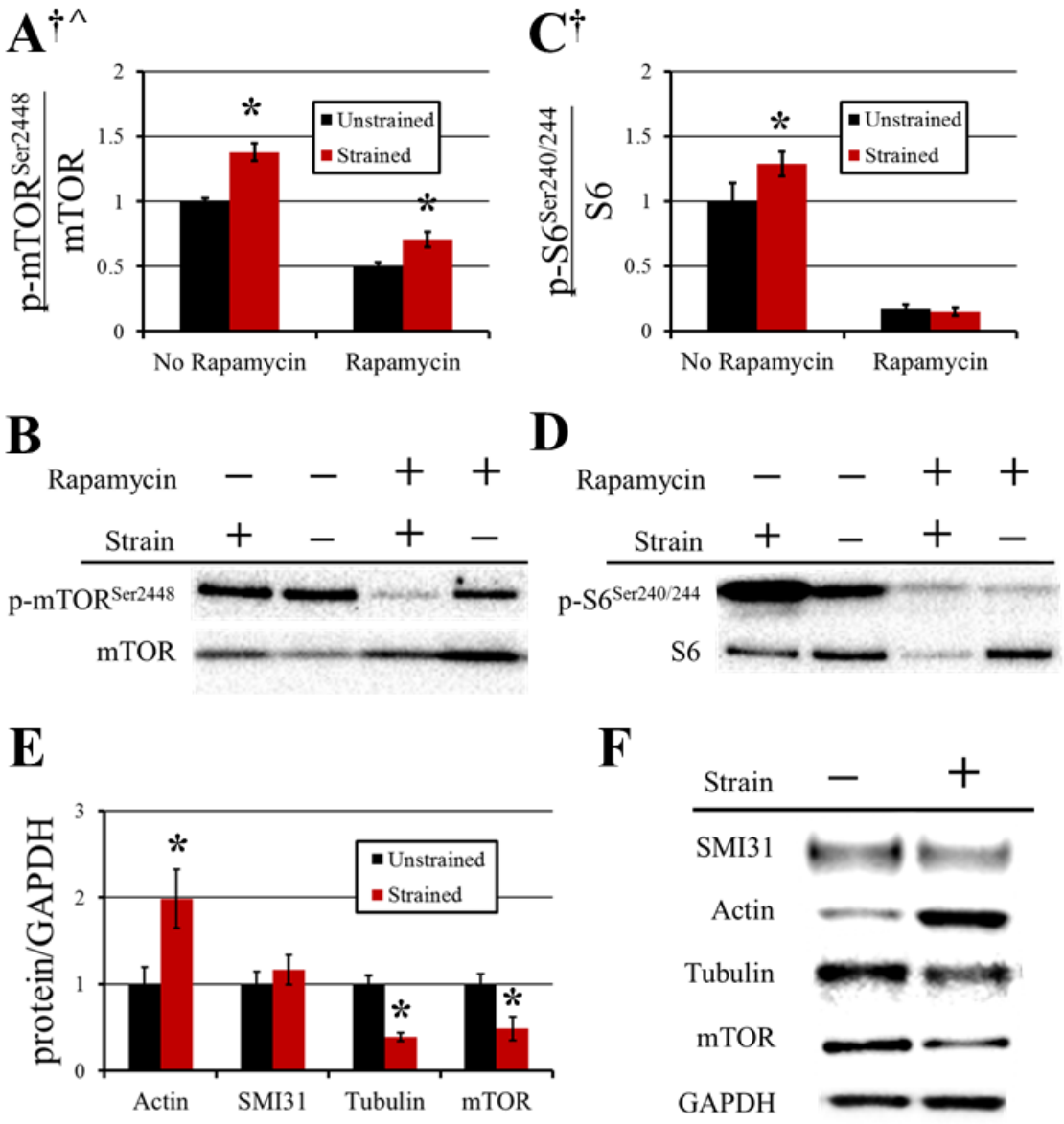

Figure 5-3: Effect of rapamycin on strain induced signaling and protein expression

Application of mTOR led to a reduction in phosphorylated levels of both mTOR (A, B) and S6 (C, D). The effect of strain remains following rapamycin administration but was muted at the level of S6. Administration of rapamycin prior to strain differentially regulated protein levels (E, F): β-actin remained elevated, SMI31 was suppressed to baseline, and both tubulin and total mTOR were reduced beyond baseline (*$p < 0.05$, paired t-test; two-way ANOVA, Strain: ^$p < 0.05$, Rapamycin: $^{+}p < 0.05$); *Mean ± SEM*

limb (82% reduction; Figures 5-3C-D) and the strained nerve (85% reduction; Figures 5-3C-D). Two-way ANOVA analysis for strain and rapamycin also revealed a significant decrease in S6 levels following rapamycin administration ($p = 8.89x10^{-12}$). In this case there was no strain effect ($p = 0.15$) but a slight interaction effect ($p = 0.0841$). Post hoc comparison of individual groups revealed a significant effect of strain in the absence of rapamycin which disappears following rapamycin administration (No Rapamycin, $p = 0.014$; Rapamycin, $p = 0.632$).

Interestingly, rapamycin treatment revealed differential translational regulation of the three probed cytoskeletal proteins. β-actin expression remained elevated following strain application ($p = 0.027$; Figures 5-3E-F). However, PNF returned to levels nearly equal to those of the unstrained nerve ($p = 0.58$; Figures 5-3E-F), while tubulin saw a significant *decrease* relative to the unstrained nerve (61% reduction; $p = 0.002$). These results suggest differential activation of mTOR associated pathways at the expense of baseline maintenance pathways.

Subsection 4: Alternative protein synthesis pathways are activated in response to strain application

In light of the differential regulation of mTOR, and the possibility that other translational pathways are also at work, p38 activation was probed. There was no effect of strain or rapamycin treatment (Strain: $p = 0.918$, Rapamycin: $p = 0.123$, Interaction: $p = 0.123$, two-way ANOVA). However, in the absence of rapamycin, there was an almost 70% reduction in p38 activation levels following the application of strain ($p = 0.075$; Figures 5-4A-B). Interestingly, though, in the presence of rapamycin, there was a trend towards increased levels following strain application in the rapamycin group ($p = 0.430$;

Figures 5-4A-B), suggesting complex interactions between mTOR signaling, p38 signaling, and strain.

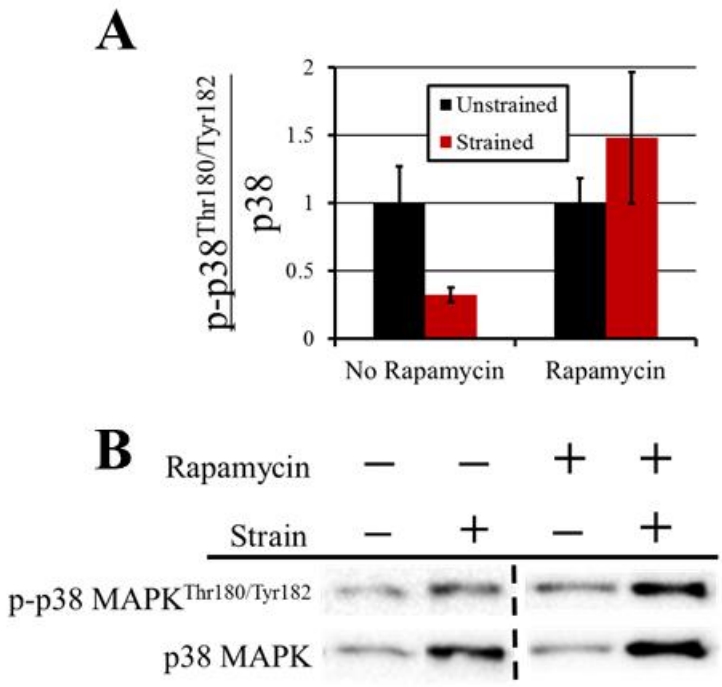

Figure 5-4: p38 MAPK signaling response to strain

Application of mTOR led to a reduction in phosphorylated levels of both mTOR (A, B) and S6 (C, D) (*graphs normalized to unstrained, no rapamycin group*). The effect of strain remains following rapamycin administration but was muted at the level of S6. Administration of rapamycin prior to strain differentially regulated protein levels (E, F) (*protein data normalized to unstrained, rapamycin treated*): β-actin remained elevated, SMI31 was suppressed to baseline, and both tubulin and total mTOR were reduced beyond baseline (*$p < 0.05$, paired t-test; two-way ANOVA, Strain: ^$p < 0.05$, Rapamycin: $^{\dagger}p < 0.05$); *Mean ± SEM*

Section 4: Discussion

In this study, we implemented a novel experimental model to examine translational pathways in response to nerve strain, in the absence of nerve injury. Our results suggest that strain induces increased cytoskeletal expression in sciatic nerves. This

increase in expression is at least partially coupled to activation of mTOR pathways for neurofilaments and tubulin, but not β-actin.

Although not a prototypical load-bearing tissue, nerves experience, accommodate, and respond to tensile deformations [54,56]. At the tissue level, such loading is well-described during joint movement, limb lengthening surgery [54,71], and more recently, strategies for end-to-end nerve repair [78] and strain-based regenerative strategies [21,182]. In single neurons, moderate strains induce beneficial outcomes [75-77], with one study reporting a dramatic ~eight-fold increase in axonal elongation rates [75].

In vivo, axons themselves may, at least partially, be protected from nerve strain by their unique undulating packing architecture within the nerves as well as properties of the extracellular matrix [3,56,57]. However, when axons themselves are strained, whether in vivo or in vitro, details on how they respond to deformation are poorly understood. An important observation was that axons do not display reduced caliber with strain, indicating volumetric expansion as well as structural stability [173]. Multiple sources of material may contribute to this expansion. In the short-term, pre-existing pools of material may be rapidly recruited from flanking regions of the cell body, consistent with the anterograde cytoskeletal flow posited during axonal outgrowth [41,173]. To accommodate long-term volume expansion additional material must be newly synthesized, either in the cell body or, as we hypothesize, locally within the axon.

Though not evaluated until this study in the context of neuronal strain, the mTOR pathway was hypothesized to be a strong candidate for modulating strain-induced local protein synthesis. This pathway is known to respond to loading in muscles by enhancing protein synthesis and leading to hypertrophy [79]. Additionally, in neurons it is known to

be vitally important in axonal elongation and regeneration following nerve injury [70,81,82], as well as for local protein synthesis, which is central to both of these processes [69]. In support of this hypothesis, we observed that strain induced a rapid and persistent increase in mTOR activation as well as downstream activation of S6 (Figures 5-2A-B).

While any number of proteins may be regulated through mTOR-S6 pathways, we focused on cytoskeletal proteins, whose synthesis is essential to volume expansion [183-185]. Expression of each of the three cytoskeletal elements that we examined, β-actin, neurofilament-H, and tubulin, appeared to be differentially induced by stretch. As observed following nerve injury, β-actin levels also increased following nerve strain. Similarly, phosphorylated neurofilament levels also increased. On the other hand, tubulin levels remained relatively unchanged with strain.

Intriguingly, regulation of cytoskeletal protein translation was also differentially regulated. Rapamycin treatment induced an approximately 50% reduction in activated mTOR levels and an over 80% reduction in activated S6 levels across experimental groups. Following reduction of mTOR activation, β-actin levels remained elevated but the response of both PNF and tubulin were altered. PNF levels were reduced in the strained configuration, leading to no difference in protein levels relative to the unstrained configuration. A reduction in tubulin levels in response to strain was also observed. It is thus likely that mTOR signaling is responsible for the observed increase in PNF following strain application, as well as some component of maintenance of tubulin levels. The maintained increase in β-actin levels suggests that an alternative signaling pathway is responsible for either de novo synthesis of β-actin or local recruitment to the region of

strain. This prompted our investigation of the p38 MAPK/eIF2 pathway as an alternate regulatory mechanism for β-actin levels following rapamycin treatment. We observed opposing trends in strain activation of p38 MAPK, depending on the presence of rapamycin, suggesting the potential for interaction between the two pathways in responding to strain. An alternate possibility is translational regulation of β-actin via RNA binding proteins. A likely candidate for such regulation is the β-actin binding protein zipcode binding protein 1 (ZBP1), whose activity appears to be controlled by calcium-mediated Src pathways [186,187]. While manipulation of these non-mTOR pathways is necessary to conclude a formal role, our results leave open the compelling possibility of competing or synergistic translational regulatory pathways.

While decreased PNF and tubulin levels in nerves following mTOR inhibition points to a strong likelihood for local synthesis, we cannot exclude contributions from other sources for the cytoskeletal protein increases. Both the cell body and flanking regions may potentially provide material for axonal growth and response to strain, however at our six hour time point this contribution is likely to be negligible. Transport of cytoskeletal cargoes is well characterized as slow component transport, with bulk rates of β-actin, tubulin, and neurofilaments transport rarely exceeding mm/day [59,60]. At these rates, six hours is likely an insufficient amount of time for newly transported proteins to appreciably contribute to measured increases, which were on the order of 50%.

While we cannot exclude contributions from other cellular populations in the *in vivo* response, SMI-31 is almost exclusively neuronal and likely represents a specifically neuronal response.

Section 5: Conclusions

Application of excessive strain and tension on nerves has a major deleterious effect which at the greatest extremes fully eliminates a nerve's conductive capacity while under experimental load [55,56]. At the extremes only minimal recovery of the signal is seen following relaxation [55,56]. In our study we were able to minimize damage as evidenced by our electrophysiological results. Nonetheless, application of moderate strain led to enhancement of mTOR signaling and cytoskeletal protein levels. The enhancement of cytoskeletal protein levels responded differentially to the inhibition of mTOR via rapamycin suggesting differential regulation of the local synthesis response to strain. Our work is among the first to identify a partial mechanism for the nerve's ability to respond and adapt to strain. It also provides the first evidence that developmental pathways may be, at least in part, recapitulated in a non-injury situation.

Section 6: Acknowledgements

We gratefully acknowledge funding from NSF (CMMI1130997 and CBET1042522) as well as the National Skeletal Muscle Research Center at UCSD. We also acknowledge helpful discussions with members of the Neuromuscular Bioengineering and Muscle Physiology Laboratories.

Chapter 6: Conclusions

Section 1: Introduction

Peripheral nervous system (PNS) injury affects many people every year. If function cannot be fully restored results in a number of burdens ranging from reduced or complete loss of motor and sensory function [8]. Current regenerative techniques are sufficient in a number of cases but best expected outcomes still result from grafting of donor tissues which are coupled with a number of complications ranging from donor site morbidity to host rejection [188,189]. For these reasons a number of alternative regenerative strategies including grafting of Schwann cells to application of strain are being explored in the hope of enhancing restoration of primary function to individuals [5]. While, both Schwann cells and strain have been noted to provide enhancements in the regenerative capacity of neurons both *in vitro* and *in vivo* [20,75-77,190], the mechanisms by which these two methods are able to achieve this are still poorly understood. My work, formatted in the framework of a two-arm study, examined mechanisms underlying both Schwann cell-neuron interactions as well as the response of nerves to the application of strain in the context of future applications to PNS regeneration techniques.

Arm 1: I investigated the interaction of Schwann cells and neurons in the context of membrane stability (Chapter 2) and transport and localization of ribosomes in Schwann cells during early myelination (Chapter 3).

Arm 2: I investigated both the physical (Chapter 4) and molecular signaling (Chapter 5) responses of whole nerve to the application of strain.

Section 2: Implications of my work

My work in the broadest sense has begun to open the doors for future studies with direct translational applications for peripheral nerve repair. In a narrower sense, each chapter advances the field's understanding of how neurons and nerves respond to their environment in a particular context. My work achieved this by enhancing the understanding of how neurons and Schwann cells interact and affect each other (Chapters 2 and 3) and how nerves respond to strain application (Chapters 4 and 5) with the specific details of each chapter found in the subsequent subsections.

Subsection 1: Variability in membrane continuity between Schwann cells and neurons [2]

In Chapter 2, I investigated the differences between the membrane stability of Schwann cells and neurons and how interactions between the two cell types can affect the stability. I found inherent differences between the membrane stability of Schwann cells and neurons. This difference manifested itself through changes in both membrane velocity and membrane correlation. The more mobile Schwann cells exhibited both higher membrane velocity and more correlated movement of membrane patches. We posited that these differences may result from the underlying cytoskeletal structure and developmental demands of each cell type.

Interesting trends were observed based upon the contact state of the cells. In this case when Schwann cells were contacting neurons and vice versa there were trends towards decreases in both membrane velocity and membrane correlation. The velocity decreases point towards a more stable cellular state. Further support for this idea of cellular stability emerged from the identification of a trend towards increased levels of cell-cell or cell-substrate contact inferred from increased levels of talin immunostaining

in Schwann cells upon development of contact with neurons. This is in agreement with previous observations of Schwann cells' ability to upregulate adhesion following neuronal contact [34]. Additionally Schwann cells are capable of increasing neurofilament phosphorylation levels [35] a hallmark of mature axons [191-193]. It is perhaps through increased neurofilament phosphorylation that the trend towards stable neuronal membrane was established in my study. Extrapolating from what I have found, scientists that intend to incorporate Schwann cells into their regenerative strategy may wish to explicitly consider their delivery method. Introduction of Schwann cells via engraftment within the conduit or injection at the site of repair could have vastly different effects on the physical stability of the cells and the regeneration process.

Subsection 2: Ribosomal trafficking in Schwann cells depends on early myelination cues

Inspired by the work detailing the transfer of ribosomes from Schwann cells to neurons following axonal injury [27,28] I investigated the development and maintenance of these populations in an *in vitro* culture model of the initial stages of myelination in Chapter 3. I found that Schwann cells initially develop distributions of stable ribosome clusters along the length of their projections within the first day of plating. These distributions are well conserved throughout the early development of the Schwann cell and following initiation of myelination. Interestingly the level of ribosomal transport decreased over time with the induction of myelination. In the absence of myelination induction, the level of ribosomal transport actually increased.

While others have noted ribosomes in the myelinated fraction of Schwann cells, it has only been within the context of MBP production [48-52]. Additionally, their notable localization near Schmidt-Lanterman incisures [48] leaves open the possibility for their

transfer following axonal injury [27]. Prior to myelination ribosomes localized to Schwann cell projections may possess larger responsibilities including focal adhesion and cytoskeletal turnover, important processes in the development and migration of unmyelinated Schwann cells. Building off my work, an effort to enhance the ribosomal presence within the myelin compartment of Schwann cells may be used to provide an enhanced source of ribosomes for local protein synthesis following injury. While ribosomal densities are observed early and maintained throughout our experimental time frame, enhanced levels could perhaps be reached by manipulation of the transport pathways following myelination may allow scientists to

Subsection 3: Nerve strain correlates with structural changes quantified by Fourier analysis [3]

Bands of Fontana are an observable banding pattern on the surface of nerves [163] which is well conserved across species and nerves types [166]. Implementing pattern detection methods previously used in other tissues [170] I was able to identify correlations between applied strains and the banding frequency in Chapter 4. These findings complement the work in Chapter 5 that investigated the effect of strain on local protein synthesis and signaling. If future surgical interventions integrate strain into a regenerative strategy or monitor strain during other nerve manipulations, it will be important that they impart moderate levels of strain below the damage threshold. Development of a tool using the relationship noted here between strain and banding pattern can allow surgeons to make simple, accurate, real-time measurements of strain while performing peripheral nerve repairs.

Subsection 4: Differential regulation of cytoskeletal protein synthesis following nerve strain

In Chapter 5 I identified strain dependent changes in cytoskeletal levels and protein synthetic signaling pathways. I found increases in cytoskeletal proteins β-actin and phosphorylated neurofilament-H (SMI31). A strain dependent increase in the protein signaling pathway driven by mTOR activation via was observed through increases in mTOR signaling and downstream S6 phosphorylation. With the application of the mTOR inhibitor rapamycin I found differential regulation of the various cytoskeletal elements in response to strain. The increase in β-actin remained whereas the increase in SMI31 was eliminated. Additionally, I found a strain dependent decrease in both tubulin and total mTOR following inhibition of mTOR with rapamycin.

Strain as a positive regulator of axonal outgrowth has begun to be explored *in vitro* [75-77]. In culture, rates of axonal elongation far exceeding native rates have been witnessed [75]. The processes underlying the strain-dependent enhancement of outgrowth are not yet understood. Combining the current understanding of the fields of muscle mechanics [79,80] and axonal elongation [69,70,81,82] I hypothesized that the application of strain will enhance activation of mTOR signaling within the axon leading to the production of cytoskeletal proteins to aid the growing axon. The finding that nerves increase activation of mTOR and downstream signals within the protein synthesis pathway locally supports our hypothesis. The adaptation of the nerve to increase levels of cytoskeletal proteins in response to strain provides a potential material and framework for axonal elongation. Complete understanding of the strain response of nerves is necessary before translational applications of this strategy can be effectively integrated into the operating room. Additionally, investigation into the complementation of a strain-based

strategy with other regenerative strategies including growth factor incorporation [16] and Schwann cell supplementation [20] will help to define the upper limits of regeneration attainable by this method.

Section 3: Future experiments and translational impact

My work has set the stage for a number of future studies to fully elucidate the context of the work within the context of translational surgical applications. In the immediate future a complementary *in vitro* study to Chapter 5 must be completed to fully characterize the role of strain in activation of neuronal local protein synthesis.

Subsection 1: Future experiments

Prior to peer-reviewed publication of Chapter 5, a complementary study investigating the application of strain on neurons *in vitro* and their response must be completed. The results in whole nerve provide significant evidence that neurons are actively responding to the applied strain. Specifically the increase in SMI31, an axonally specific protein, supports the idea that the neurons themselves are responding to the application of strain. Nonetheless, an *in vitro* model will do well to support our results in the context of neuronally specific activation.

Two methods have been devised to complete this task. First, puromycin incorporation as a surrogate for protein synthesis [194] will be utilized to identify the levels of proteins synthesized in a one hour time window within the axonal compartment of dissociated DRGs grown on a flexible substrate. Immunoflourescence quantification of puromycin levels (Figure 6-1) similar to talin identification (Figure 2-5) in Chapter 2 will be used to quantify and compare synthesis rates in strained and unstrained neurons. As this method reveals non-specific protein synthesis, an alternative method may be utilized. Whole adult DRGs will be plated and grown for three days on flexible substrates with

experimental wells subjected to a period of six hours of strain on Day 3. Following strain administration axons in the direction of strain will be collected and processed for western blots as done in Chapter 5. Identification of axonally specific changes in signaling and protein levels will allow us to strengthen our *in vivo* results.

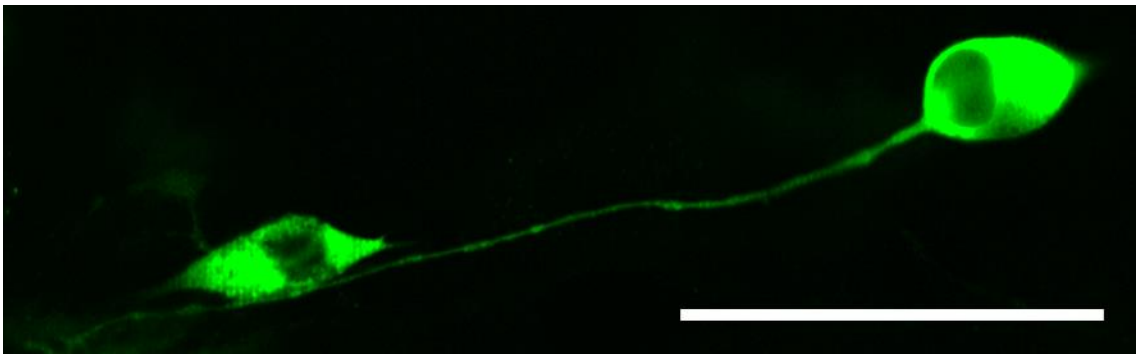

Figure 6-1: Immunolabeling of puromycin incorporation

Identification of puromycin incorporation within cultured DRGs can provide details about the amounts and localization of newly synthesized proteins

Subsection 2: Translational impact

While the work I have done presents little direct translational impact, it manages to open the door for a number of future studies to expand on, clarify, and incorporate my work into translational therapies. The work in Chapters 2 and 3 provides an important understanding of how Schwann cells and neurons interact with each other in the context of membrane stability and ribosomal incorporation in the myelin fraction. These two results point to the importance of interactions that should be considered prior to the incorporation of Schwann cells in a regenerative solution. Specific considerations include the manipulation of the Schwann cells prior to implantation and the method of introduction either through incorporation on a guidance conduit or direct injection.

Chapter 4 offers a unique technique that can be incorporated in surgical settings. Current surgical convention is to perform tension-free nerve repairs in light of growing. Even within current convention, being able to accurately identify the lower limits of strain application can limit the size of the surgical gap and potentially improve expected outcomes.

Chapter 5 focuses on the role strain application has on inducing local protein synthesis within the whole nerve. My study was performed outside of the context of injury but could potentially be applied to regenerative techniques. Validation of my results in the context of recovery following injury will go a long way towards garnering support for translational application of this technique in a regeneration strategy. With the well-documented importance of local protein synthesis in axonal regeneration and elongation [69,81] identification of a local protein synthesis response to strain further validates it as a promising repair component. Further understanding of the strain response might allow incorporation of the underlying signaling response without the physical limitations of strain application and consideration of the inevitable associated pain.

The work presented here provides context for a number of peripheral nervous system regeneration strategies, offers additional considerations for the future development of translational therapeutics, and proposes mechanisms by which the nervous system is able to adapt to its current environment.

Bibliography

1. Wisse B. Central nervous system and peripheral nervous system. NIH; 2013.
2. Love JM, Pathak GK, Chetta J, Shah SB. Variability in Membrane Continuity Between Schwann Cells and Neurons. Cellular and Molecular Bioengineering 2012;5(4):450-462.
3. Love JM, Chuang TH, Lieber RL, Shah SB. Nerve strain correlates with structural changes quantified by Fourier analysis. Muscle Nerve 2013;48(3):433-435.
4. Shah SB, Love JM, O'Neill A, Lovering RM, Bloch RJ. Influences of desmin and keratin 19 on passive biomechanical properties of mouse skeletal muscle. J Biomed Biotechnol 2012;2012:704061.
5. Ting-Hsien Chuang REW, James M. Love, John P. Fisher, Sameer B. Shah. A Novel Internal Fixator Device for Peripheral Nerve Regeneration. Tissue Engineering Part C 2013;19(6):427-437.
6. Pathak GK, Love JM, Chetta J, Shah SB. A comparative quantitative assessment of axonal and dendritic mRNA transport in maturing hippocampal neurons. PLoS One 2013;8(7):e65917.
7. Birch R, Misra P, Stewart MP, Eardley WG, Ramasamy A, Brown K, Shenoy R, Anand P, Clasper J, Dunn R, Etherington J. Nerve injuries sustained during warfare: part I--Epidemiology. J Bone Joint Surg Br 2012;94(4):523-528.
8. Ciaramitaro P, Mondelli M, Logullo F, Grimaldi S, Battiston B, Sard A, Scarinzi C, Migliaretti G, Faccani G, Cocito D. Traumatic peripheral nerve injuries: epidemiological findings, neuropathic pain and quality of life in 158 patients. J Peripher Nerv Syst 2010;15(2):120-127.
9. Asplund M, Nilsson M, Jacobsson A, von Holst H. Incidence of traumatic peripheral nerve injuries and amputations in Sweden between 1998 and 2006. Neuroepidemiology 2009;32(3):217-228.
10. Noble J, Munro CA, Prasad VS, Midha R. Analysis of upper and lower extremity peripheral nerve injuries in a population of patients with multiple injuries. J Trauma 1998;45(1):116-122.
11. Ruijs AC, Jaquet JB, Kalmijn S, Giele H, Hovius SE. Median and ulnar nerve injuries: a meta-analysis of predictors of motor and sensory recovery after modern microsurgical nerve repair. Plast Reconstr Surg 2005;116(2):484-494; discussion 495-486.
12. Frykman G, Gramyk K. Results of nerve grafting. Operative nerve repair and reconstruction Philadelphia: JB Lippincott 1991:553-567.
13. Brooks DN, Weber RV, Chao JD, Rinker BD, Zoldos J, Robichaux MR, Ruggeri SB, Anderson KA, Bonatz EE, Wisotsky SM, Cho MS, Wilson C, Cooper EO, Ingari JV, Safa B, Parrett BM, Buncke GM. Processed nerve allografts for peripheral nerve reconstruction: a multicenter study of utilization and outcomes in sensory, mixed, and motor nerve reconstructions. Microsurgery 2012;32(1):1-14.
14. Strauch RJ, Strauch B. Nerve conduits: an update on tubular nerve repair and reconstruction. J Hand Surg Am 2013;38(6):1252-1255; quiz 1255.

15. Kobayashi J, Mackinnon SE, Watanabe O, Ball DJ, Gu XM, Hunter DA, Kuzon WM, Jr. The effect of duration of muscle denervation on functional recovery in the rat model. Muscle Nerve 1997;20(7):858-866.
16. Yang Y, De Laporte L, Rives CB, Jang JH, Lin WC, Shull KR, Shea LD. Neurotrophin releasing single and multiple lumen nerve conduits. J Control Release 2005;104(3):433-446.
17. Zhang N, Zhang C, Wen X. Fabrication of semipermeable hollow fiber membranes with highly aligned texture for nerve guidance. J Biomed Mater Res A 2005;75(4):941-949.
18. Oh SH, Kim JH, Song KS, Jeon BH, Yoon JH, Seo TB, Namgung U, Lee IW, Lee JH. Peripheral nerve regeneration within an asymmetrically porous PLGA/Pluronic F127 nerve guide conduit. Biomaterials 2008;29(11):1601-1609.
19. Huang W, Begum R, Barber T, Ibba V, Tee NC, Hussain M, Arastoo M, Yang Q, Robson LG, Lesage S, Gheysens T, Skaer NJ, Knight DP, Priestley JV. Regenerative potential of silk conduits in repair of peripheral nerve injury in adult rats. Biomaterials 2012;33(1):59-71.
20. Hadlock T, Sundback C, Hunter D, Cheney M, Vacanti JP. A polymer foam conduit seeded with Schwann cells promotes guided peripheral nerve regeneration. Tissue Eng 2000;6(2):119-127.
21. Chuang TH, Wilson RE, Love JM, Fisher JP, Shah SB. A novel internal fixator device for peripheral nerve regeneration. Tissue Eng Part C Methods 2013;19(6):427-437.
22. Rushton WA. A theory of the effects of fibre size in medullated nerve. J Physiol 1951;115(1):101-122.
23. Son YJ, Thompson WJ. Schwann cell processes guide regeneration of peripheral axons. Neuron 1995;14(1):125-132.
24. Bandtlow CE, Heumann R, Schwab ME, Thoenen H. Cellular localization of nerve growth factor synthesis by in situ hybridization. EMBO J 1987;6(4):891-899.
25. Acheson A, Barker PA, Alderson RF, Miller FD, Murphy RA. Detection of brain-derived neurotrophic factor-like activity in fibroblasts and Schwann cells: inhibition by antibodies to NGF. Neuron 1991;7(2):265-275.
26. Bunge RP. The role of the Schwann cell in trophic support and regeneration. J Neurol 1994;242(1 Suppl 1):S19-21.
27. Court FA, Hendriks WT, MacGillavry HD, Alvarez J, van Minnen J. Schwann cell to axon transfer of ribosomes: toward a novel understanding of the role of glia in the nervous system. J Neurosci 2008;28(43):11024-11029.
28. Court FA, Midha R, Cisterna BA, Grochmal J, Shakhbazau A, Hendriks WT, Van Minnen J. Morphological evidence for a transport of ribosomes from Schwann cells to regenerating axons. Glia 2011;59(10):1529-1539.
29. Jessen KR, Mirsky R. The origin and development of glial cells in peripheral nerves. Nat Rev Neurosci 2005;6(9):671-682.
30. Cheng HL, Steinway M, Delaney CL, Franke TF, Feldman EL. IGF-I promotes Schwann cell motility and survival via activation of Akt. Mol Cell Endocrinol 2000;170(1-2):211-215.

31. Meintanis S, Thomaidou D, Jessen KR, Mirsky R, Matsas R. The neuron-glia signal beta-neuregulin promotes Schwann cell motility via the MAPK pathway. Glia 2001;34(1):39-51.
32. Yamauchi J, Chan JR, Shooter EM. Neurotrophins regulate Schwann cell migration by activating divergent signaling pathways dependent on Rho GTPases. Proc Natl Acad Sci U S A 2004;101(23):8774-8779.
33. Lemke G, Chao M. Axons Regulate Schwann-Cell Expression of the Major Myelin and Ngf Receptor Genes. Development 1988;102(3):499-504.
34. Weiner JA, Fukushima N, Contos JJ, Scherer SS, Chun J. Regulation of Schwann cell morphology and adhesion by receptor-mediated lysophosphatidic acid signaling. J Neurosci 2001;21(18):7069-7078.
35. de Waegh SM, Lee VM, Brady ST. Local modulation of neurofilament phosphorylation, axonal caliber, and slow axonal transport by myelinating Schwann cells. Cell 1992;68(3):451-463.
36. Popov S, Brown A, Poo MM. Forward plasma membrane flow in growing nerve processes. Science 1993;259(5092):244-246.
37. Bray D. Surface movements during the growth of single explanted neurons. Proc Natl Acad Sci U S A 1970;65(4):905-910.
38. Futerman AH, Banker GA. The economics of neurite outgrowth--the addition of new membrane to growing axons. Trends Neurosci 1996;19(4):144-149.
39. Zakharenko S, Popov S. Plasma membrane recycling and flow in growing neurites. Neuroscience 2000;97(1):185-194.
40. Pfenninger KH. Plasma membrane expansion: a neuron's Herculean task. Nat Rev Neurosci 2009;10(4):251-261.
41. Dai J, Sheetz MP. Axon membrane flows from the growth cone to the cell body. Cell 1995;83(5):693-701.
42. Pfenninger KH, Maylie-Pfenninger MF. Lectin labeling of sprouting neurons. II. Relative movement and appearance of glycoconjugates during plasmalemmal expansion. J Cell Biol 1981;89(3):547-559.
43. Kucik DF, Elson EL, Sheetz MP. Cell migration does not produce membrane flow. J Cell Biol 1990;111(4):1617-1622.
44. Zakharenko S, Popov S. Dynamics of axonal microtubules regulate the topology of new membrane insertion into the growing neurites. J Cell Biol 1998;143(4):1077-1086.
45. Prager-Khoutorsky M, Spira ME. Neurite retraction and regrowth regulated by membrane retrieval, membrane supply, and actin dynamics. Brain Res 2009;1251:65-79.
46. Dai J, Sheetz MP, Wan X, Morris CE. Membrane tension in swelling and shrinking molluscan neurons. J Neurosci 1998;18(17):6681-6692.
47. Morris CE, Wang JA, Markin VS. The invagination of excess surface area by shrinking neurons. Biophys J 2003;85(1):223-235.
48. Gould RM, Mattingly G. Regional localization of RNA and protein metabolism in Schwann cells in vivo. J Neurocytol 1990;19(3):285-301.
49. Griffiths IR, Mitchell LS, McPhilemy K, Morrison S, Kyriakides E, Barrie JA. Expression of myelin protein genes in Schwann cells. J Neurocytol 1989;18(3):345-352.

50. Trapp BD, Moench T, Pulley M, Barbosa E, Tennekoon G, Griffin J. Spatial segregation of mRNA encoding myelin-specific proteins. Proc Natl Acad Sci U S A 1987;84(21):7773-7777.
51. Trapp BD, Hauer P, Lemke G. Axonal regulation of myelin protein mRNA levels in actively myelinating Schwann cells. J Neurosci 1988;8(9):3515-3521.
52. Colman DR, Kreibich G, Frey AB, Sabatini DD. Synthesis and incorporation of myelin polypeptides into CNS myelin. J Cell Biol 1982;95(2 Pt 1):598-608.
53. Nave K-A. Myelination and the trophic support of long axons. Nature Reviews Neuroscience 2010;11(4):275-283.
54. Boyd BS, Puttlitz C, Gan J, Topp KS. Strain and excursion in the rat sciatic nerve during a modified straight leg raise are altered after traumatic nerve injury. J Orthop Res 2005;23(4):764-770.
55. Wall EJ, Massie JB, Kwan MK, Rydevik BL, Myers RR, Garfin SR. Experimental stretch neuropathy. Changes in nerve conduction under tension. J Bone Joint Surg Br 1992;74(1):126-129.
56. Kwan MK, Wall EJ, Massie J, Garfin SR. Strain, stress and stretch of peripheral nerve. Rabbit experiments in vitro and in vivo. Acta Orthop Scand 1992;63(3):267-272.
57. Phillips JB, Smit X, De Zoysa N, Afoke A, Brown RA. Peripheral nerves in the rat exhibit localized heterogeneity of tensile properties during limb movement. J Physiol 2004;557(Pt 3):879-887.
58. Haninec P. Undulating course of nerve fibres and bands of Fontana in peripheral nerves of the rat. Anat Embryol (Berl) 1986;174(3):407-411.
59. Hoffman PN, Lasek RJ. The slow component of axonal transport. Identification of major structural polypeptides of the axon and their generality among mammalian neurons. J Cell Biol 1975;66(2):351-366.
60. Black MM, Lasek RJ. Axonal transport of actin: slow component b is the principal source of actin for the axon. Brain Res 1979;171(3):401-413.
61. Koenig E, Adams P. Local protein synthesizing activity in axonal fields regenerating in vitro. J Neurochem 1982;39(2):386-400.
62. Koenig E, Martin R. Cortical plaque-like structures identify ribosome-containing domains in the Mauthner cell axon. J Neurosci 1996;16(4):1400-1411.
63. Bixby JL, Lilien J, Reichardt LF. Identification of the major proteins that promote neuronal process outgrowth on Schwann cells in vitro. J Cell Biol 1988;107(1):353-361.
64. Merianda TT, Lin AC, Lam JS, Vuppalanchi D, Willis DE, Karin N, Holt CE, Twiss JL. A functional equivalent of endoplasmic reticulum and Golgi in axons for secretion of locally synthesized proteins. Mol Cell Neurosci 2009;40(2):128-142.
65. Taylor AM, Berchtold NC, Perreau VM, Tu CH, Li Jeon N, Cotman CW. Axonal mRNA in uninjured and regenerating cortical mammalian axons. J Neurosci 2009;29(15):4697-4707.
66. Eng H, Lund K, Campenot RB. Synthesis of beta-tubulin, actin, and other proteins in axons of sympathetic neurons in compartmented cultures. J Neurosci 1999;19(1):1-9.
67. Sotelo-Silveira JR, Calliari A, Kun A, Benech JC, Sanguinetti C, Chalar C, Sotelo JR. Neurofilament mRNAs are present and translated in the normal and severed sciatic nerve. J Neurosci Res 2000;62(1):65-74.

68. Olink-Coux M, Hollenbeck PJ. Localization and active transport of mRNA in axons of sympathetic neurons in culture. J Neurosci 1996;16(4):1346-1358.
69. Zheng JQ, Kelly TK, Chang B, Ryazantsev S, Rajasekaran AK, Martin KC, Twiss JL. A functional role for intra-axonal protein synthesis during axonal regeneration from adult sensory neurons. J Neurosci 2001;21(23):9291-9303.
70. Ning K, Drepper C, Valori CF, Ahsan M, Wyles M, Higginbottom A, Herrmann T, Shaw P, Azzouz M, Sendtner M. PTEN depletion rescues axonal growth defect and improves survival in SMN-deficient motor neurons. Hum Mol Genet 2010;19(16):3159-3168.
71. Ikeda K, Tomita K, Tanaka S. Experimental study of peripheral nerve injury during gradual limb elongation. Hand Surg 2000;5(1):41-47.
72. Ozcivici E, Luu YK, Adler B, Qin YX, Rubin J, Judex S, Rubin CT. Mechanical signals as anabolic agents in bone. Nat Rev Rheumatol 2010;6(1):50-59.
73. McBride SH, Silva MJ. Adaptive and Injury Response of Bone to Mechanical Loading. Bonekey Osteovision 2012;1.
74. Hornberger TA. Mechanotransduction and the regulation of mTORC1 signaling in skeletal muscle. Int J Biochem Cell Biol 2011;43(9):1267-1276.
75. Pfister BJ, Iwata A, Meaney DF, Smith DH. Extreme stretch growth of integrated axons. J Neurosci 2004;24(36):7978-7983.
76. Bray D. Axonal growth in response to experimentally applied mechanical tension. Dev Biol 1984;102(2):379-389.
77. Lamoureux P, Buxbaum RE, Heidemann SR. Axonal outgrowth of cultured neurons is not limited by growth cone competition. J Cell Sci 1998;111 (Pt 21):3245-3252.
78. Hentz VR, Rosen JM, Xiao SJ, McGill KC, Abraham G. The nerve gap dilemma: a comparison of nerves repaired end to end under tension with nerve grafts in a primate model. J Hand Surg Am 1993;18(3):417-425.
79. Klossner S, Durieux AC, Freyssenet D, Flueck M. Mechano-transduction to muscle protein synthesis is modulated by FAK. Eur J Appl Physiol 2009;106(3):389-398.
80. Dalla Costa AP, Clemente CF, Carvalho HF, Carvalheira JB, Nadruz W, Jr., Franchini KG. FAK mediates the activation of cardiac fibroblasts induced by mechanical stress through regulation of the mTOR complex. Cardiovasc Res 2010;86(3):421-431.
81. Verma P, Chierzi S, Codd AM, Campbell DS, Meyer RL, Holt CE, Fawcett JW. Axonal protein synthesis and degradation are necessary for efficient growth cone regeneration. J Neurosci 2005;25(2):331-342.
82. Park KK, Liu K, Hu Y, Kanter JL, He Z. PTEN/mTOR and axon regeneration. Exp Neurol 2010;223(1):45-50.
83. Ruggero D, Pandolfi PP. Does the ribosome translate cancer? Nature Reviews Cancer 2003;3(3):179-192.
84. Vance JE, Campenot RB, Vance DE. The synthesis and transport of lipids for axonal growth and nerve regeneration. Biochim Biophys Acta 2000;1486(1):84-96.
85. Dent EW, Gertler FB. Cytoskeletal dynamics and transport in growth cone motility and axon guidance. Neuron 2003;40(2):209-227.
86. Miller KE, Sheetz MP. Direct evidence for coherent low velocity axonal transport of mitochondria. J Cell Biol 2006;173(3):373-381.

87. Heidemann SR, Buxbaum RE. Tension as a regulator and integrator of axonal growth. Cell Motil Cytoskeleton 1990;17(1):6-10.
88. Suter DM, Forscher P. Substrate-cytoskeletal coupling as a mechanism for the regulation of growth cone motility and guidance. J Neurobiol 2000;44(2):97-113.
89. Chan CE, Odde DJ. Traction dynamics of filopodia on compliant substrates. Science 2008;322(5908):1687-1691.
90. Grenningloh G, Soehrman S, Bondallaz P, Ruchti E, Cadas H. Role of the microtubule destabilizing proteins SCG10 and stathmin in neuronal growth. J Neurobiol 2004;58(1):60-69.
91. Suter DM, Miller KE. The emerging role of forces in axonal elongation. Prog Neurobiol 2011;94(2):91-101.
92. Martini R. Expression and functional roles of neural cell surface molecules and extracellular matrix components during development and regeneration of peripheral nerves. J Neurocytol 1994;23(1):1-28.
93. Kidd G, Andrews SB, Trapp BD. Axons regulate the distribution of Schwann cell microtubules. J Neurosci 1996;16(3):946-954.
94. Gupta D, Venugopal J, Prabhakaran MP, Dev VR, Low S, Choon AT, Ramakrishna S. Aligned and random nanofibrous substrate for the in vitro culture of Schwann cells for neural tissue engineering. Acta Biomater 2009;5(7):2560-2569.
95. Ahmed Z, Brown RA. Adhesion, alignment, and migration of cultured Schwann cells on ultrathin fibronectin fibres. Cell Motil Cytoskeleton 1999;42(4):331-343.
96. Ahmed Z, Underwood S, Brown RA. Low concentrations of fibrinogen increase cell migration speed on fibronectin/fibrinogen composite cables. Cell Motil Cytoskeleton 2000;46(1):6-16.
97. Wang Y, Zhao Z, Zhao B, Qi HX, Peng J, Zhang L, Xu WJ, Hu P, Lu SB. Biocompatibility evaluation of electrospun aligned poly (propylene carbonate) nanofibrous scaffolds with peripheral nerve tissues and cells in vitro. Chin Med J (Engl) 2011;124(15):2361-2366.
98. Munevar S, Wang YL, Dembo M. Distinct roles of frontal and rear cell-substrate adhesions in fibroblast migration. Mol Biol Cell 2001;12(12):3947-3954.
99. Song J, O'Connor L T, Yu W, Baas PW, Duncan ID. Microtubule alterations in cultured taiep rat oligodendrocytes lead to deficits in myelin membrane formation. J Neurocytol 1999;28(8):671-683.
100. Yan M, Cheng C, Jiang J, Liu Y, Gao Y, Guo Z, Liu H, Shen A. Essential role of SRC suppressed C kinase substrates in Schwann cells adhesion, spreading and migration. Neurochem Res 2009;34(5):1002-1010.
101. Chetta J, Kye C, Shah SB. Cytoskeletal dynamics in response to tensile loading of mammalian axons. Cytoskeleton (Hoboken) 2010;67(10):650-665.
102. Bacia K, Majoul IV, Schwille P. Probing the endocytic pathway in live cells using dual-color fluorescence cross-correlation analysis. Biophys J 2002;83(2):1184-1193.
103. Acheson A, Rutishauser U. Neural cell adhesion molecule regulates cell contact-mediated changes in choline acetyltransferase activity of embryonic chick sympathetic neurons. J Cell Biol 1988;106(2):479-486.
104. Fernandez-Valle C, Gorman D, Gomez AM, Bunge MB. Actin plays a role in both changes in cell shape and gene-expression associated with Schwann cell myelination. J Neurosci 1997;17(1):241-250.

105. Catsicas M, Allcorn S, Mobbs P. Early activation of Ca(2+)-permeable AMPA receptors reduces neurite outgrowth in embryonic chick retinal neurons. J Neurobiol 2001;49(3):200-211.
106. Webster HD. The geometry of peripheral myelin sheaths during their formation and growth in rat sciatic nerves. J Cell Biol 1971;48(2):348-367.
107. Van Vactor D. Adhesion and signaling in axonal fasciculation. Curr Opin Neurobiol 1998;8(1):80-86.
108. Oh U, Hwang SW, Kim D. Capsaicin activates a nonselective cation channel in cultured neonatal rat dorsal root ganglion neurons. J Neurosci 1996;16(5):1659-1667.
109. Porter S, Clark MB, Glaser L, Bunge RP. Schwann cells stimulated to proliferate in the absence of neurons retain full functional capability. J Neurosci 1986;6(10):3070-3078.
110. Nagata Y, Burger MM. Wheat germ agglutinin. Molecular characteristics and specificity for sugar binding. J Biol Chem 1974;249(10):3116-3122.
111. Honerkamp-Smith AR, Cicuta P, Collins MD, Veatch SL, den Nijs M, Schick M, Keller SL. Line tensions, correlation lengths, and critical exponents in lipid membranes near critical points. Biophys J 2008;95(1):236-246.
112. Seilheimer B, Schachner M. Regulation of neural cell adhesion molecule expression on cultured mouse Schwann cells by nerve growth factor. EMBO J 1987;6(6):1611-1616.
113. Korlach J, Schwille P, Webb WW, Feigenson GW. Characterization of lipid bilayer phases by confocal microscopy and fluorescence correlation spectroscopy. Proc Natl Acad Sci U S A 1999;96(15):8461-8466.
114. Wawrezinieck L, Rigneault H, Marguet D, Lenne PF. Fluorescence correlation spectroscopy diffusion laws to probe the submicron cell membrane organization. Biophys J 2005;89(6):4029-4042.
115. Hatten ME, Mason CA. Mechanisms of glial-guided neuronal migration in vitro and in vivo. Experientia 1990;46(9):907-916.
116. Hockfield S, McKay RD. Identification of major cell classes in the developing mammalian nervous system. J Neurosci 1985;5(12):3310-3328.
117. Anton ES, Weskamp G, Reichardt LF, Matthew WD. Nerve growth factor and its low-affinity receptor promote Schwann cell migration. Proc Natl Acad Sci U S A 1994;91(7):2795-2799.
118. Bray D, Bunge MB. Serial analysis of microtubules in cultured rat sensory axons. J Neurocytol 1981;10(4):589-605.
119. Godenschwege TA, Kristiansen LV, Uthaman SB, Hortsch M, Murphey RK. A conserved role for Drosophila Neuroglian and human L1-CAM in central-synapse formation. Curr Biol 2006;16(1):12-23.
120. Kelly BM, Gillespie CS, Sherman DL, Brophy PJ. Schwann cells of the myelin-forming phenotype express neurofilament protein NF-M. J Cell Biol 1992;118(2):397-410.
121. Waxman SG, Bennett MV. Relative conduction velocities of small myelinated and non-myelinated fibres in the central nervous system. Nat New Biol 1972;238(85):217-219.

122. Bryan DJ, Holway AH, Wang KK, Silva AE, Trantolo DJ, Wise D, Summerhayes IC. Influence of glial growth factor and Schwann cells in a bioresorbable guidance channel on peripheral nerve regeneration. Tissue Eng 2000;6(2):129-138.
123. Jacobs JM, Cavanagh JB. Species differences in internode formation following two types of peripheral nerve injury. J Anat 1969;105(Pt 2):295-306.
124. Twiss JL, van Minnen J. New insights into neuronal regeneration: the role of axonal protein synthesis in pathfinding and axonal extension. J Neurotrauma 2006;23(3-4):295-308.
125. Leader DP. Protein-Biosynthesis on Membrane-Bound Ribosomes. Trends in Biochemical Sciences 1979;4(9):205-208.
126. Caro LG, Palade GE. Protein Synthesis, Storage, and Discharge in the Pancreatic Exocrine Cell. An Autoradiographic Study. J Cell Biol 1964;20:473-495.
127. Jamieson JD, Palade GE. Intracellular transport of secretory proteins in the pancreatic exocrine cell. II. Transport to condensing vacuoles and zymogen granules. J Cell Biol 1967;34(2):597-615.
128. Ganoza MC, Williams CA. In vitro synthesis of different categories of specific protein by membrane-bound and free ribosomes. Proc Natl Acad Sci U S A 1969;63(4):1370-1376.
129. Brophy PJ, Boccaccio GL, Colman DR. The distribution of myelin basic protein mRNAs within myelinating oligodendrocytes. Trends Neurosci 1993;16(12):515-521.
130. Lee DA, Zurawel RH, Windebank AJ. Ciliary Neurotrophic Factor Expression in Schwann-Cells Is Induced by Axonal Contact. J Neurochem 1995;65(2):564-568.
131. Kruger T, Zentgraf H, Scheer U. Intranucleolar sites of ribosome biogenesis defined by the localization of early binding ribosomal proteins. J Cell Biol 2007;177(4):573-578.
132. Pedraza L, Colman DR. Fluorescent myelin proteins provide new tools to study the myelination process. J Neurosci Res 2000;60(6):697-703.
133. Eldridge CF, Bunge MB, Bunge RP, Wood PM. Differentiation of axon-related Schwann cells in vitro. I. Ascorbic acid regulates basal lamina assembly and myelin formation. J Cell Biol 1987;105(2):1023-1034.
134. Bolte S, Cordelieres FP. A guided tour into subcellular colocalization analysis in light microscopy. J Microsc 2006;224(Pt 3):213-232.
135. Manders EM, Stap J, Brakenhoff GJ, van Driel R, Aten JA. Dynamics of three-dimensional replication patterns during the S-phase, analysed by double labelling of DNA and confocal microscopy. J Cell Sci 1992;103 (Pt 3):857-862.
136. Chetta J, Shah SB. A novel algorithm to generate kymographs from dynamic axons for the quantitative analysis of axonal transport. J Neurosci Methods 2011;199(2):230-240.
137. Zadeh KS, Shah SB. Mathematical modeling and parameter estimation of axonal cargo transport. J Comput Neurosci 2010;28(3):495-507.
138. DiStefano PS, Friedman B, Radziejewski C, Alexander C, Boland P, Schick CM, Lindsay RM, Wiegand SJ. The neurotrophins BDNF, NT-3, and NGF display distinct patterns of retrograde axonal transport in peripheral and central neurons. Neuron 1992;8(5):983-993.
139. Morris RL, Hollenbeck PJ. Axonal transport of mitochondria along microtubules and F-actin in living vertebrate neurons. J Cell Biol 1995;131(5):1315-1326.

140. Weber MJ. Ribosomal RNA turnover in contact inhibited cells. Nat New Biol 1972;235(54):58-61.
141. Elson K, Ribeiro RM, Perelson AS, Simmons A, Speck P. The life span of ganglionic glia in murine sensory ganglia estimated by uptake of bromodeoxyuridine. Exp Neurol 2004;186(1):99-103.
142. Thomas MG, Tosar LJM, Loschi M, Pasquini JM, Correale J, Kindler S, Boccaccio GL. Staufen recruitment into stress granules does not affect early mRNA transport in oligodendrocytes. Mol Biol Cell 2005;16(1):405-420.
143. Buchthal F, Carlsen F, Behse F. Schmidt-Lanterman clefts: a morphometric study in human sural nerve. Am J Anat 1987;180(2):156-160.
144. Trapp BD, Andrews SB, Wong A, O'Connell M, Griffin JW. Co-localization of the myelin-associated glycoprotein and the microfilament components, F-actin and spectrin, in Schwann cells of myelinated nerve fibres. J Neurocytol 1989;18(1):47-60.
145. Wilhelm JE, Vale RD. RNA on the move: the mRNA localization pathway. J Cell Biol 1993;123(2):269-274.
146. Brown A. Slow axonal transport: stop and go traffic in the axon. Nat Rev Mol Cell Biol 2000;1(2):153-156.
147. Kidd GJ, Andrews SB, Trapp BD. Organization of microtubules in myelinating Schwann cells. J Neurocytol 1994;23(12):801-810.
148. Nobes CD, Hall A. Rho GTPases control polarity, protrusion, and adhesion during cell movement. J Cell Biol 1999;144(6):1235-1244.
149. Feltri ML, Scherer SS, Nemni R, Kamholz J, Vogelbacker H, Scott MO, Canal N, Quaranta V, Wrabetz L. Beta 4 integrin expression in myelinating Schwann cells is polarized, developmentally regulated and axonally dependent. Development 1994;120(5):1287-1301.
150. Fabrizi C, Kelly BM, Gillespie CS, Schlaepfer WW, Scherer SS, Brophy PJ. Transient expression of the neurofilament proteins NF-L and NF-M by Schwann cells is regulated by axonal contact. J Neurosci Res 1997;50(2):291-299.
151. Scherer SS, Kamholz J, Jakowlew SB. Axons modulate the expression of transforming growth factor-betas in Schwann cells. Glia 1993;8(4):265-276.
152. LeBlanc AC, Windebank AJ, Poduslo JF. P0 gene expression in Schwann cells is modulated by an increase of cAMP which is dependent on the presence of axons. Brain Res Mol Brain Res 1992;12(1-3):31-38.
153. Chiu SY, Scherer SS, Blonski M, Kang SS, Messing A. Axons regulate the expression of Shaker-like potassium channel genes in Schwann cells in peripheral nerve. Glia 1994;12(1):1-11.
154. Palacios IM. Hop-on hop-off: Polysomes take a tour of the cell on endosomes. J Cell Biol 2014;204(3):287-289.
155. Higuchi Y, Ashwin P, Roger Y, Steinberg G. Early endosome motility spatially organizes polysome distribution. J Cell Biol 2014;204(3):343-357.
156. Lipowsky R, Beeg J, Dimova R, Klumpp S, Muller MJI. Cooperative behavior of molecular motors: Cargo transport and traffic phenomena. Physica E-Low-Dimensional Systems & Nanostructures 2010;42(3):649-661.
157. Lafontaine DL. A 'garbage can' for ribosomes: how eukaryotes degrade their ribosomes. Trends in Biochemical Sciences 2010;35(5):267-277.

158. Shi R, Whitebone J. Conduction deficits and membrane disruption of spinal cord axons as a function of magnitude and rate of strain. J Neurophysiol 2006;95(6):3384-3390.
159. Li J, Shi R. Stretch-induced nerve conduction deficits in guinea pig ex vivo nerve. J Biomech 2007;40(3):569-578.
160. Mackinnon SE. New directions in peripheral nerve surgery. Ann Plast Surg 1989;22(3):257-273.
161. Terzis J, Faibisoff B, Williams B. The nerve gap: suture under tension vs. graft. Plast Reconstr Surg 1975;56(2):166-170.
162. Anava S, Greenbaum A, Ben Jacob E, Hanein Y, Ayali A. The regulative role of neurite mechanical tension in network development. Biophys J 2009;96(4):1661-1670.
163. Fontana F, Gibelin J. Traité sur le vénin de la vipere, sur les poisons americains, sur le laurier-cerise et sur quelques autres poisons vegetaux. On y a joint des observations sur la structure primitive du corps animal. Différentes expériences sur la reproduction des nerfs et la description d'un nouveau canal de l'oeil. Florence,1781.
164. Pourmand R, Ochs S, Jersild RA, Jr. The relation of the beading of myelinated nerve fibers to the bands of Fontana. Neuroscience 1994;61(2):373-380.
165. Merolli A, Mingarelli L, Rocchi L. A more detailed mechanism to explain the "bands of Fontana" in peripheral nerves. Muscle Nerve 2012;46(4):540-547.
166. Clarke E, Bearn JG. The spiral nerve bands of Fontana. Brain 1972;95(1):1-20.
167. Stolinski C. Structure and composition of the outer connective tissue sheaths of peripheral nerve. J Anat 1995;186 (Pt 1):123-130.
168. Hansen KA, Weiss JA, Barton JK. Recruitment of tendon crimp with applied tensile strain. J Biomech Eng 2002;124(1):72-77.
169. Sacks MS. Incorporation of experimentally-derived fiber orientation into a structural constitutive model for planar collagenous tissues. J Biomech Eng 2003;125(2):280-287.
170. Shah SB, Lieber RL. Simultaneous imaging and functional assessment of cytoskeletal protein connections in passively loaded single muscle cells. J Histochem Cytochem 2003;51(1):19-29.
171. Weiss P. Nerve patterns: the mechanics of nerve growth. Growth 1941;5:163-203.
172. Iwata A, Browne KD, Pfister BJ, Gruner JA, Smith DH. Long-term survival and outgrowth of mechanically engineered nervous tissue constructs implanted into spinal cord lesions. Tissue Eng 2006;12(1):101-110.
173. Loverde JR, Ozoka VC, Aquino R, Lin L, Pfister BJ. Live imaging of axon stretch growth in embryonic and adult neurons. J Neurotrauma 2011;28(11):2389-2403.
174. Tetzlaff W, Bisby MA, Kreutzberg GW. Changes in cytoskeletal proteins in the rat facial nucleus following axotomy. J Neurosci 1988;8(9):3181-3189.
175. Donnelly CJ, Park M, Spillane M, Yoo S, Pacheco A, Gomes C, Vuppalanchi D, McDonald M, Kim HH, Merianda TT, Gallo G, Twiss JL. Axonally synthesized beta-actin and GAP-43 proteins support distinct modes of axonal growth. J Neurosci 2013;33(8):3311-3322.
176. Dennerll TJ, Lamoureux P, Buxbaum RE, Heidemann SR. The cytomechanics of axonal elongation and retraction. J Cell Biol 1989;109(6 Pt 1):3073-3083.

177. Eshleman JS, Carlson BL, Mladek AC, Kastner BD, Shide KL, Sarkaria JN. Inhibition of the mammalian target of rapamycin sensitizes U87 xenografts to fractionated radiation therapy. Cancer Res 2002;62(24):7291-7297.
178. White AT, McCurdy CE, Philp A, Hamilton DL, Johnson CD, Schenk S. Skeletal muscle-specific overexpression of SIRT1 does not enhance whole-body energy expenditure or insulin sensitivity in young mice. Diabetologia 2013;56(7):1629-1637.
179. Schenk S, McCurdy CE, Philp A, Chen MZ, Holliday MJ, Bandyopadhyay GK, Osborn O, Baar K, Olefsky JM. Sirt1 enhances skeletal muscle insulin sensitivity in mice during caloric restriction. J Clin Invest 2011;121(11):4281-4288.
180. Restaino SM, Abliz E, Wachrathit K, Krauthamer V, Shah SB. Biomechanical and functional variation in rat sciatic nerve following cuff electrode implantation. J Neuroeng Rehabil 2014;11(1):73.
181. Westerga J, Gramsbergen A. Changes in the electromyogram of two major hindlimb muscles during locomotor development in the rat. Exp Brain Res 1993;92(3):479-488.
182. Abe I, Ochiai N, Ichimura H, Tsujino A, Sun J, Hara Y. Internodes can nearly double in length with gradual elongation of the adult rat sciatic nerve. J Orthop Res 2004;22(3):571-577.
183. Friede RL, Samorajski T. Axon caliber related to neurofilaments and microtubules in sciatic nerve fibers of rats and mice. Anat Rec 1970;167(4):379-387.
184. Fine RE, Bray D. Actin in growing nerve cells. Nat New Biol 1971;234(47):115-118.
185. Hoffman PN, Lasek RJ. Axonal transport of the cytoskeleton in regenerating motor neurons: constancy and change. Brain Res 1980;202(2):317-333.
186. Huttelmaier S, Zenklusen D, Lederer M, Dictenberg J, Lorenz M, Meng X, Bassell GJ, Condeelis J, Singer RH. Spatial regulation of beta-actin translation by Src-dependent phosphorylation of ZBP1. Nature 2005;438(7067):512-515.
187. Yao J, Sasaki Y, Wen Z, Bassell GJ, Zheng JQ. An essential role for beta-actin mRNA localization and translation in Ca2+-dependent growth cone guidance. Nat Neurosci 2006;9(10):1265-1273.
188. IJpma FF, Nicolai J-PA, Meek MF. Sural nerve donor-site morbidity: thirty-four years of follow-up. Ann Plast Surg 2006;57(4):391-395.
189. Mackinnon SE, Doolabh VB, Novak CB, Trulock EP. Clinical outcome following nerve allograft transplantation. Plast Reconstr Surg 2001;107(6):1419-1429.
190. Hood B, Levene HB, Levi AD. Transplantation of autologous Schwann cells for the repair of segmental peripheral nerve defects. Neurosurg Focus 2009;26(2):E4.
191. Carden MJ, Schlaepfer W, Lee V. The structure, biochemical properties, and immunogenicity of neurofilament peripheral regions are determined by phosphorylation state. Journal of Biological Chemistry 1985;260(17):9805-9817.
192. Komiya Y, Tashiro T, Kurokawa M. Phosphorylation of neurofilament proteins during their axonal transport. Biomedical research 1986;7(5):345-348.
193. Komiya Y, Tashiro T, Kurokawa M. Occurrence of faster migrating neurofilament proteins as revealed by their phosphorylation. Biomedical research 1986;7(5):359-363.
194. Schmidt EK, Clavarino G, Ceppi M, Pierre P. SUnSET, a nonradioactive method to monitor protein synthesis. Nat Methods 2009;6(4):275-277.